

BEHAVIOUR AND STRENGTH OF STEEL TWIN GIRDER SYSTEMS WITH
TORSIONAL BRACES

by

Christopher Mantha

Submitted in partial fulfilment of the requirements
for the degree of Master of Applied Science

at

Dalhousie University
Halifax, Nova Scotia
August 2014

© Copyright by Christopher Mantha, 2014

To my parents, Beryl and John, and my girlfriend, Brittany:

Mom and Dad – you have always taught me to work hard and follow my dreams; now I am one step closer to that accomplishment.

Brittany – I don't know what I would have done without you. You have kept me focused and motivated throughout this long enduring process with never ending support and guidance. I am truly grateful and I thank you from the bottom of my heart.

TABLE OF CONTENTS

LIST OF TABLES	vi
LIST OF FIGURES	ix
ABSTRACT	xiv
LIST OF ABBREVIATIONS AND SYMBOLS USED	xv
ACKNOWLEDGEMENTS	xix
CHAPTER 1 INTRODUCTION	1
1.1 BACKGROUND OF RESEARCH	1
1.2 OBJECTIVES AND SCOPE	4
1.3 OUTLINE OF RESEARCH	5
CHAPTER 2 LITERATURE SURVEY	6
2.1 BEAM BRACING	6
2.1.1 <i>Lateral Bracing</i>	6
2.1.2 <i>Torsional Bracing</i>	8
2.2 LATERAL TORSIONAL BUCKLING OF A BEAM	12
2.3 LATERAL TORSIONAL BUCKLING OF BEAMS WITH TORSIONAL BRACES	15
2.4 BEAMS WITH COMBINED LATERAL AND TORSIONAL BRACING	17
2.5 GLOBAL LATERAL BUCKLING OF A GIRDER SYSTEM	18
2.6 CODES AND STANDARDS	21
2.4.1 <i>CSA S16 (2010)</i>	21
2.4.2 <i>CSA S6 (2006)</i>	22
2.4.3 <i>AISC 360 (2010)</i>	22
CHAPTER 3 EXPERIMENTAL PROGRAM	25
3.1 GENERAL	25
3.2 TEST SPECIMEN	25
3.3 TEST SCHEME	28
3.4 TEST SETUP	29
3.5 INSTRUMENTATION AND DATA ACQUISITION	34

3.6 TEST PROCEDURE	37
3.7 TENSION TEST.....	39
CHAPTER 4 EXPERIMENTAL RESULTS	42
4.1 MATERIAL PROPERTIES.....	42
4.2 RESIDUAL STRESS.....	44
4.3 BUCKLING CAPACITY	44
4.4 FAILURE MODES	49
4.5 VERIFICATION OF TEST SETUPS AND INSTRUMENTATION	53
4.6 COMPARISON TO ANALYTICAL RESULTS	61
4.6.1 Specimen C1 Comparison.....	61
4.6.2 Specimen C2 Critical Moment Comparison	63
4.7 COMPARISON TO DESIGN STANDARDS.....	63
CHAPTER 5 FINITE ELEMENT ANALYSIS.....	66
5.1 GENERAL	66
5.2 FINITE ELEMENT ANALYSIS.....	66
5.2.1 Description of Elements.....	66
5.2.2 Material Non-Linearity and Stress-Strain Relationship.....	67
5.2.3 Finite Element Mesh	68
5.2.4 Initial Imperfections.....	70
5.2.5 Boundary Conditions	70
5.2.6 Residual Stresses.....	71
5.2.7 Load Application.....	72
5.2.8 Non-Linear Buckling Analysis	72
5.3 FINITE ELEMENT RESULTS.....	73
CHAPTER 6 PARAMETRIC STUDY.....	84
6.1 GENERAL	84
6.2 GIRDER SPACING	84
6.3 CROSS-FRAME STIFFNESS	88
6.4 NUMBER OF INTERIOR CROSS-FRAMES.....	91

6.5	CONTINUOUS TORSIONAL BRACING STIFFNESS	94
6.6	CSA S6 (2006) CRITICAL MOMENT.....	97
6.7	BRACE FORCE	100
6.8	FAILURE MODES	102
CHAPTER 7	CONCLUSIONS AND RECOMMENDATIONS	104
7.1	SUMMARY.....	104
7.2	CONCLUSIONS.....	104
7.3	RECOMMENDATIONS.....	106
REFERENCES.....		108
APPENDIX A		111
APPENDIX B		118
APPENDIX C		123
APPENDIX D		129
APPENDIX E		133

LIST OF TABLES

Table 2.1	AISC Bracing Requirements (2010).....	24
Table 3.1	Geometric configuration comparison.	27
Table 3.2	Specimen configurations.....	28
Table 4.1	Material properties.	43
Table 4.2	Specimen modulus of elasticity.	43
Table 4.3	Experimental results for test specimens.....	45
Table 4.4	Comparison of experimental and calculated flexural stress.	60
Table 4.5	Specimen C1 M_{cr} results comparison.	62
Table 4.6	Specimen C2 M_{cr} results comparison.	63
Table 4.7	Specimen C1-2 M_{cr} Comparison to CSA S6 (2006) (per beam).	64
Table 4.8	Specimen C2 M_{cr} comparison to CSA S6 (2006) (per beam).....	65
Table 5.1	Element summary.	66
Table 5.2	Mesh convergence study results.	69
Table 5.3	Summary of finite element and test results for three specimens.	73
Table 6.1	Critical moment comparison between finite element results and Equation [2.23] with varying girder spacing.....	85
Table 6.2	Calculated torsional stiffness for varying cross-frame member sizes.	89
Table 6.3	FE critical moment results of three cross frames with variation in brace stiffness.....	90
Table 6.4	Global elastic critical moment (kN·m) comparison with varying number of interior cross-frames.	92
Table 6.5	Continuous torsional brace stiffness.	95
Table 6.6	Comparison of FE critical moment and Equation [2.17] values (kN·m).....	96
Table 6.7	Critical moment comparison between FE and CSA S6 (2006) results.....	98
Table 6.8	Effective length factor to achieve FE results using CSA S6 (2006).....	99
Table 6.9	Comparison with CSA S6 (2006) without loading height effect.....	100
Table 6.10	Cross-frame bracing forces.	102
Table B.1	Critical moment calculation of specimen C1-2 calculated using continuous torsional brace stiffness (for Table 4.5; Taylor and Ojalvo, 1966).....	118
Table B.2	Simplified critical moment calculation of specimen C1-2 calculated using continuous torsional brace stiffness (for Table 4.5; Phillips, 1990).....	119

Table B.3	Simplified critical moment calculation of specimen C1-2 calculated using continuous torsional brace stiffness (for Table 4.5; Yura, 2001).....	120
Table B.4	Global elastic buckling moment of specimen C1-2 (for Table 4.5; Yura <i>et al.</i> , 2008).....	121
Table B.5	Critical moment calculation of specimen C2 (for Table 4.6; Phillips, 1990)	122
Table C.1	CSA S6 (2006) moment calculation for beam braced with torsional cross-frames (top flange loading not considered; for Table 4.7).....	123
Table C.2	CSA S6 (2006) moment calculation for beam braced with torsional cross-frames (top flange loading considered; for Table 4.7).....	124
Table C.3	CSA S6 (2006) moment calculation for beam braced with torsional cross-frames and lateral in plan bracing (top flange loading not considered; for Table 4.8).....	125
Table C.4	CSA S6 (2006) moment calculation for beam braced with torsional cross-frames and lateral in plan bracing (top flange loading considered; for Table 4.8).....	126
Table C.5	Calculated torsional brace stiffness (for Table 4.7).....	128
Table E.1	Sample calculation of Equation [2.23] critical moment calculation presented in Table 6.1.....	133
Table E.2	Cross-frame torsional stiffness calculation presented in Table 6.2.....	134
Table E.3	Equation [2.23] critical moment calculations presented in Table 6.4.....	135
Table E.4	Calculation of critical moment presented in Table 6.6 using Equation [2.17].....	136
Table E.5	Calculation of critical moment using CSA S6 (2006) for two intermediate cross-frames presented in Table 6.7.....	137
Table E.6	Calculation of critical moment using CSA S6 (2006) for three intermediate cross-frames presented in Table 6.7.....	138
Table E.7	Calculation of critical moment using CSA S6 (2006) for five intermediate cross-frames presented in Table 6.7.....	139
Table E.8	Calculation of torsional cross-frame stiffness using CSA S6 (2006) critical moment presented in Table 6.7.....	140
Table E.9	Calculation of effective length using CSA S6 (2006) critical moment calculation for two intermediate cross-frames presented in Table 6.7.....	141
Table E.10	Calculation of effective length using CSA S6 (2006) critical moment calculation for three intermediate cross-frames presented in Table 6.7.....	142
Table E.11	Calculation of effective length using CSA S6 (2006) critical moment calculation for five intermediate cross-frames presented in Table 6.7.....	143

Table E.12	CSA S6 (2006) critical moment calculation with two cross-frames loaded through shear center (for Table 6.9).....	144
Table E.13	CSA S6 (2006) critical moment calculation with three cross-frames loaded through shear center (for Table 6.9).....	145
Table E.14	CSA S6 (2006) critical moment calculation with five cross-frames loaded through shear center (for Table 6.9).....	146
Table E.15	AISC 360 (2010) critical moment calculation with two cross-frames loaded through shear center (for Table 6.9).....	147
Table E.16	AISC 360 (2010) critical moment calculation with three cross-frames loaded through shear center.	148
Table E.17	AISC 360 (2010) critical moment calculation with five cross-frames loaded through shear center (for Table 6.9).....	149
Table E.18	CSA S6 (2006) brace force calculation for two intermediate cross-frames (for Table 6.10).	150
Table E.19	CSA S6 (2006) brace force calculation for three intermediate cross-frames (for Table 6.10).	151
Table E.20	CSA S6 (2006) brace force calculation for five intermediate cross-frames (for Table 6.10).	152

LIST OF FIGURES

Figure 1.1	Beam failure modes (adapted from Galambos, 1998).	1
Figure 1.2	Plan view of twin girder system braced with combination of cross-frames and lateral bracing.	3
Figure 1.3	Typical cross-frame X-bracing arrangement.	3
Figure 1.4	Plan view of twin girder system braced with only cross-frames.	4
Figure 2.1	Plan view of relative brace system.	7
Figure 2.2	Tension cross-frame system (adapted from Yura, 2001).	9
Figure 2.3	Typical full depth web stiffener at torsional brace location (adapted from Yura, 2001).	10
Figure 2.4	Equivalent moment factor for concentrated and distributed loads (Galambos, 1998).	14
Figure 2.5	Buckling modes of twin girders with discrete torsional braces (Yura <i>et al.</i> , 2008).	20
Figure 3.1	Overall view of the test specimen.	26
Figure 3.2	Practical and scaled specimen beam.	26
Figure 3.3	Typical cross-frame system.	27
Figure 3.4	Typical compression flange bracing detail.	28
Figure 3.5	Plan view of specimen C1 with vertical cross-frames.	29
Figure 3.6	Plan view of specimen C2 with cross-frames and plan bracing.	29
Figure 3.7	Schematic test setup.	30
Figure 3.8	Specimen C1-1 (a) Pivot assembly; and (b) roller assembly.	31
Figure 3.9	Specimen C1-2, C2 roller and pivot assemblies.	32
Figure 3.10	Bearing assembly movements.	32
Figure 3.11	Uni-directional bearing assembly.	33
Figure 3.12	Multi-directional bearing assembly.	33
Figure 3.13	Pinned bearing assembly.	33
Figure 3.14	Strain gages instrumented at beam supports.	34
Figure 3.15	Typical midspan instrumentation schematic.	35
Figure 3.16	Plan view of experimental specimen showing LVDT locations on specimen.	36
Figure 3.17	(a) Vertical displacement; and (b) lateral displacement.	37
Figure 3.18	Midspan inclinometer.	37

Figure 3.19	Initial out-of-straightness of beam webs.....	38
Figure 3.20	Initial lateral sweep of beams.	39
Figure 3.21	Tension coupon cutting scheme.....	40
Figure 3.22	Tensile coupon dimensions.....	40
Figure 3.23	Tension coupon test setup.....	41
Figure 4.1	Coupon OF 2 stress-strain curve.....	42
Figure 4.2	Simplified Residual Stress Pattern (Trahair <i>et al.</i> , 1972).	44
Figure 4.3	Specimen C1-1 load vs. midspan lateral displacement response.....	46
Figure 4.4	Specimen C1-2 load vs. midspan lateral displacement response.....	46
Figure 4.5	Specimen C2 load vs. midspan lateral displacement response.	47
Figure 4.6	Specimen C1-1 load vs. midspan vertical displacement response.....	47
Figure 4.7	Specimen C1-2 load vs. midspan vertical displacement response.....	48
Figure 4.8	Specimen C2 load vs. midspan vertical displacement response.	48
Figure 4.9	Buckled shape of specimen: (a) C1-1, (b) C1-2 and (c) C2.....	50
Figure 4.10	Deformed shape with sinusoidal buckling of specimen C1-1 post failure.....	51
Figure 4.11	Yielding of specimen C1-1 beam 2 compression flange.	51
Figure 4.12	(a) Inelastic buckling of specimen C2; and (b) magnified view of inelastic buckling failure.....	52
Figure 4.13	Local buckling of specimen C2 compression flange and web.....	53
Figure 4.14	Specimen C1-1 comparison of calculated and experimental vertical displacements.....	54
Figure 4.15	Specimen C1-2 comparison of calculated and experimental vertical displacements.....	54
Figure 4.16	Specimen C2 comparison of calculated and experimental vertical displacements.....	55
Figure 4.17	Specimen C1-1 vertical strains in webs of beam ends.....	55
Figure 4.18	Location of longitudinal strain gages along specimen.....	56
Figure 4.19	Specimen C1-2 experimental neutral axis plot at location 1.	57
Figure 4.20	Specimen C1-1 midspan experimental neutral axis plot.....	58
Figure 4.21	Specimen C1-2 midspan experimental neutral axis plot.....	58
Figure 4.22	Specimen C2 midspan neutral axis plot.....	59
Figure 4.23	Engaged portion of pivot assembly base.	59

Figure 5.1	Elasto-plastic material model.....	67
Figure 5.2	Test specimen material model applied to finite element.	68
Figure 5.3	Cross-section of finite element mesh.....	69
Figure 5.4	Typical cross-frame mesh.	70
Figure 5.5	Finite element model end support conditions.	71
Figure 5.6	Residual stress pattern applied to finite element model.....	71
Figure 5.7	Typical midspan load application at top flange to web junction.	72
Figure 5.8	Specimen C1-1 roller friction experiment.	75
Figure 5.9	Lateral load vs. lateral displacement of specimen C1-1 roller assembly.....	75
Figure 5.10	Finite element load vs. midspan lateral deflection response for specimen C1-1.	76
Figure 5.11	Specimen C1-1 sinusoidal buckling mode shape between cross-braces. .	76
Figure 5.12	Lateral load vs. lateral displacement of specimen C1-2 roller assembly.....	77
Figure 5.13	Finite element load vs. midspan lateral deflection response for specimen C1-2.	78
Figure 5.14	Specimen C1-2 global buckling mode shape.....	78
Figure 5.15	Lateral load vs. lateral displacement of specimen C2 roller assembly.	79
Figure 5.16	Finite element load vs. midspan lateral deflection response for specimen C2 roller assembly.	80
Figure 5.17	Connection of roller assembly to load distribution beam.	80
Figure 5.18	Specimen C2 buckled shape between lateral brace points.....	81
Figure 5.19	Midspan vertical displacement comparison of specimen C1-1.	82
Figure 5.20	Midspan vertical displacement comparison of specimen C1-2.	82
Figure 5.21	Midspan vertical displacement comparison of specimen C2.....	83
Figure 6.1	Load versus top flange lateral displacement response of a girder.	86
Figure 6.2	Load versus lateral displacement response of 3 interior cross-frame specimen with varying girder spacing.	87
Figure 6.3	Critical moment vs girder spacing for FE and Eqn. [2.23].	88
Figure 6.4	Effect of varying cross-frame stiffness on the load vs. top flange lateral displacement curves of girders.....	90
Figure 6.5	Effect of torsional cross-frame system stiffness on critical moment for varying cross-frame brace members.	91

Figure 6.6	Load versus lateral displacement response of 2 interior cross-frame specimen with variable girder spacing.....	92
Figure 6.7	Load versus lateral displacement response of 5 interior cross-frame specimen with variable girder spacing.....	93
Figure 6.8	Comparison of FE and Equation [2.23] results for the number of cross-frames.	94
Figure 6.9	Determination of critical load from load versus top flange lateral displacement response of a girder.....	96
Figure 6.10	Von Mises stress at buckling for five cross-frame arrangement.....	96
Figure 6.11	Relationship between unbraced length modifier k and ratio of provided torsional stiffness to ideal torsional stiffness.....	99
Figure 6.12	Schematic for: (a) cross-frame geometry; and (b) brace force diagram.....	101
Figure 6.13	Applied load vs. brace force response of cross-frame member.....	102
Figure 6.14	FE buckled shape.....	103
Figure A.1	Coupon OF 1 stress-strain curve.....	111
Figure A.2	Coupon OF 2 stress-strain curve.....	111
Figure A.3	Coupon OF 3 stress-strain curve.....	112
Figure A.4	Coupon OF 4 stress-strain curve.....	112
Figure A.5	Coupon OW 1 stress-strain curve.....	113
Figure A.6	Coupon OW 2 stress-strain curve.....	113
Figure A.7	Coupon OW 3 stress-strain curve.....	114
Figure A.8	Coupon NF 1 stress-strain curve.....	114
Figure A.9	Coupon NF 2 stress-strain curve.....	115
Figure A.10	Coupon NF 3 stress-strain curve.....	115
Figure A.11	Coupon NW 1 stress-strain curve.....	116
Figure A.12	Coupon NW 2 stress-strain curve.....	116
Figure A.13	Coupon NW 3 stress-strain curve.....	117
Figure A.14	Coupon NW 4 stress-strain curve.....	117
Figure C.1	Diagram for calculation of moment gradient (ω_2) for cross-frame only condition (for Table 4.7).....	127
Figure C.2	Diagram for calculation of moment gradient (ω_2) for combination cross-frame and in plan bracing condition (for Table 4.8).	127
Figure D.1	Stress vs strain diagram for beam 1 web.....	129

Figure D.2	Stress vs strain diagram for beam 1 flange.	130
Figure D.3	Stress vs strain diagram for beam 2 web.	131
Figure D.4	Stress vs strain diagram for beam 2 flange.	132

ABSTRACT

For both buildings and bridges where slab-on-girder construction is used, maintaining the lateral torsional stability of girders during the construction stage is a critical issue. The current industry practice is to use both lateral and torsional bracing to ensure girder stability. However, lateral bracing becomes redundant and ineffective once the concrete deck has hardened and acts as lateral bracing instead. In addition, commonly placed on the underside of the slab, the installed lateral bracing may present a long-term maintenance liability. The current Design of Steel Structures Code CSA S16 (2010) and Canadian Highway Bridge Design Code CSA S6 (2006) do not provide adequate guidelines addressing the design of lateral stability of a girder system where the girders are braced solely with torsional bracing. Although a simplified method is recommended for strength design in the standards, it does not provide an explicit stiffness requirement for the torsional bracing system.

This study is motivated to investigate the behaviour and strength of beams with only discrete torsional bracing. The experimental program of a scaled twin-girder system with different arrangements of lateral and torsional bracing was conducted. Concurrently, a finite element model was developed and verified with the test results. A parametric study using the finite element model was conducted to study further the effect of girder spacing, cross-frame stiffness, and number of cross-frames on the lateral torsional stability of the twin-girder system. Results showed that the girder spacing and number of cross-frames had the most significant effects on the critical moment of girders braced with only torsional braces. Changing the cross-frame member stiffness did not result in any marked change in the critical moment. The comparison of numerical results with design equations contained in the current CSA S16 (2010) and S6 (2006) standards showed that a stiffness requirement for the torsional brace should be implemented. A relationship between the design critical moment and the ratio of provided-to-required torsional stiffness was discussed.

LIST OF ABBREVIATIONS AND SYMBOLS USED

A_{br}	cross-sectional area of the lateral brace
A_c	area of diagonal cross-frame members
A_h	area of horizontal cross-frame members
B1	beam 1
B2	beam 2
BRG	bearing
b_s	stiffener width
c	1.0 for doubly symmetric I-shapes
C_b	factor accounting for moment gradient
C_{bb}	moment gradient factor for a braced beam with unbraced length, L_b
C_{bu}	moment gradient factor for a beam with unbraced length, L
c_L	reduction factor for imperfections in lateral brace stiffness
c_t	reduction factor for imperfections in torsional brace stiffness
C_T	variable to account for loading height; $C_T = 1.2$
C_w	warping torsion constant
CHBDC	Canadian Highway Bridge Design Code
d	beam depth
E	modulus of elasticity
F	1% of the flange compressive force at the buckling load
F_{br}	brace force
F_{cr}	critical plate buckling stress
FE	finite element
f_y	yield stress
f_u	ultimate stress

G	shear modulus of elasticity
h_b	height of cross-frame
h_o	distance between flange centroids
I_{eff}	effective moment of inertia about beam's y-axis
I_x	strong axis moment of inertia
I_y	moment of inertia about beam's y-axis
J	St.-Venant torsion constant
k	effective length multiplier
L	beam length; span
L_b	unbraced length of beam between brace points
L_c	length of diagonal cross-frame member
L_{br}	length of brace
L_g	girder length
L_u	unbraced length of beam between torsional braces
LVDT	linear variable differential transducer
L/d	span to depth ratio
M_a	bending moment at one-quarter point of unbraced segment
M_b	bending moment at midpoint of unbraced segment
M_{br}	brace moment
M_c	bending moment at three-quarter point of unbraced segment
M_{cr}	beam buckling moment
$M_{CRe\text{xp}}$	experimental critical moment
M_{max}	maximum bending moment of unbraced segment
M_o	elastic critical buckling moment derived in Equation [2.9]
M_p	plastic moment

M_r	required flexural strength of beam
M_{rb}	flexural strength of torsional brace
M_u	CSA S6 (2006) critical elastic moment
M_y	yielding moment of section
n	number of intermediate torsional braces along the beam length
P	load applied to the beams
P_{cr}	critical buckling load
$P_{C_{Rexp}}$	experimental critical buckling load
P_y	axial force in beam due to flexure
r_{ts}	effective radius of gyration
r_y	weak axis radius of gyration
S	spacing between adjacent girders
S/d	spacing to depth ratio
THK	thickness
t_s	stiffener thickness
t_w	beam web thickness
TYP	typical
u_x	translation in the x direction
u_y	translation in the y direction
u_z	translation in the z direction
W	warping constant
w_{exp}	uniformly distributed self-weight of specimen
β_b	stiffness of a brace member
β_g	girder web stiffness
β_L	continuous lateral brace stiffness

β_{sec}	stiffness due to cross-sectional distortion
β_t	resultant torsional stiffness of intermediate cross-frame
β_T	continuous torsional cross-frame stiffness
β_{ti}	ideal stiffness of torsional cross-frame
Δ_o	initial out of straightness of the girder
Δ_L	mid span top flange lateral displacement at P_{cr}
$\Delta_{L,B1}$	B1 midspan lateral displacement
$\Delta_{L,B2}$	B2 midspan lateral displacement
Δ_V	maximum midspan vertical displacement at P_{cr}
$\Delta_{V,B1}$	B1 midspan vertical displacement
$\Delta_{V,B2}$	B2 midspan vertical displacement
Θ_x	rotation about the x axis
Θ_y	rotation about the y axis
Θ_z	rotation about the z axis
κ	ratio of smaller to larger end moments, M_1/M_2
λ_y	slenderness ratio about beam's weak axis
σ_{top}	normal stress in top flange
σ_{bottom}	normal stress in bottom flange
ω_2	moment gradient for CSA S6 (2006)

ACKNOWLEDGEMENTS

First, I want to express my gratitude towards my supervisor, Dr. Yi Liu, for providing me with the opportunity to work on this project and gain knowledge in academic research.

Thank you to my committee members, Dr. Jane Thorburn and Dr. Dmitry Garagash, for taking the time to review this research project.

I would also like to thank Brian Liekens, Blair Nickerson, Brian Kennedy and Phil Vickers for their assistance during the laboratory testing program and Xi Chen for his assistance with the finite element study.

Finally, I would like to thank my parents, John and Beryl, my sister, Chantal, my brother, Adam, and my beautiful girlfriend, Brittany, for supporting me throughout my academic career and keeping me motivated to complete this degree.

CHAPTER 1 INTRODUCTION

1.1 BACKGROUND OF RESEARCH

Slab-on-girder bridges are commonly used in bridge construction. A typical slab-on-girder bridge is composed of two or more evenly spaced steel plate girders that are interconnected by a concrete deck slab. For the design check of the girders at the ultimate limit state, the girder is reasonably considered to be fully supported by the deck slab for its lateral torsional buckling capacity. However, during construction of the concrete deck and prior to its hardening, the girders are most susceptible to lateral torsional buckling failure since the deck slab is not composite with the steel plate girders.

Figure 1.1 plots the critical moment (M_{cr}) versus beam length. As shown in the figure, lateral torsional buckling governs the flexural capacity of slender and intermediate beams and is a phenomenon that occurs when beams in flexure undergo out-of-plane buckling and twisting when a critical load is reached.

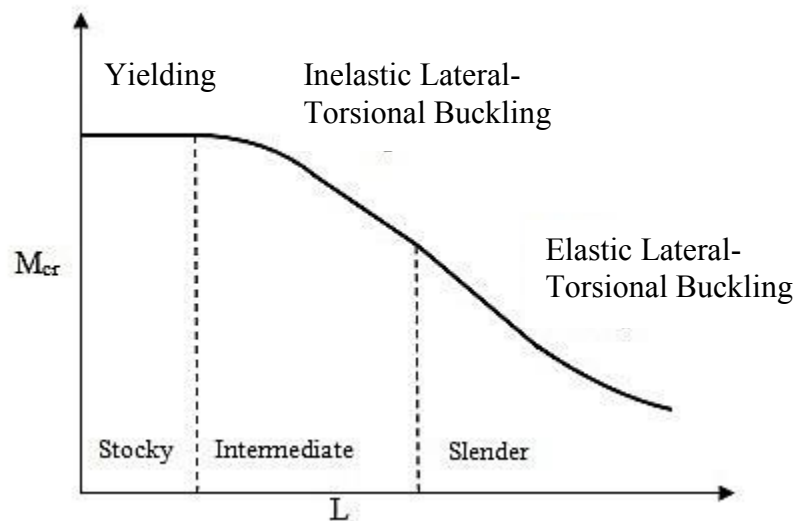


Figure 1.1 Beam failure modes (adapted from Galambos, 1998).

For plate girders fully braced by a concrete slab, the moment resistance is dependent on cross-sectional strength. In comparison, plate girders braced at discrete locations along the compression flange, have a moment resistance dependent on an unbraced length of

girder (Timoshenko & Gere 1961). To prevent lateral torsional buckling failure, beams must be properly braced against lateral deflection and twisting.

Since the girder is most susceptible to buckling during the construction stage, the Canadian Highway and Bridge Design Code (CHBDC) CSA S6 (2006) suggests that bracing be provided. In current practice, two types of bracings are often used in combination to satisfy this requirement, namely lateral and torsional bracing. The lateral bracing is implemented in the plane of the compression flange between two girders, usually one exterior and the adjacent girder as shown in Figure 1.2. This type of bracing, also referred to as plan bracing, is used to provide the lateral restraint for compressive flanges of the girder systems. In a multi-girder system, no additional lateral bracing is provided since the remaining girders are considered to “lean-on” the two braced girders. In addition to plan bracing between a pair of girders, the discrete torsional restraints, often referred as cross-frames, are also required at certain brace points over the girder span connecting all girders. The torsional braces are often in the form of X bracing or K bracing, but for shallower girders single horizontal channels connecting the girder at mid-height is an economic, but less rigid alternative. A typical cross-frame X bracing is shown in Figure 1.3. When lateral and torsional bracing types are present, the unbraced length of the girder is normally taken as the cross-frame spacing, L_b , shown in Figure 1.2. For plate girders, the combined lateral and torsional bracing has shown to produce satisfactory results in terms of buckling capacity.

However, plan bracing is not always a popular choice with contractors. If the bracing is placed above the top flange for incorporation within the slab, it interferes with the installment of reinforcement and formwork. If it is placed below the underside of the top flange, it presents a long-term maintenance liability. The plan bracing becomes redundant when the concrete deck attains 75% of its compressive strength allowing the deck to behave as a lateral diaphragm due to the composite action developed between the girder and deck.

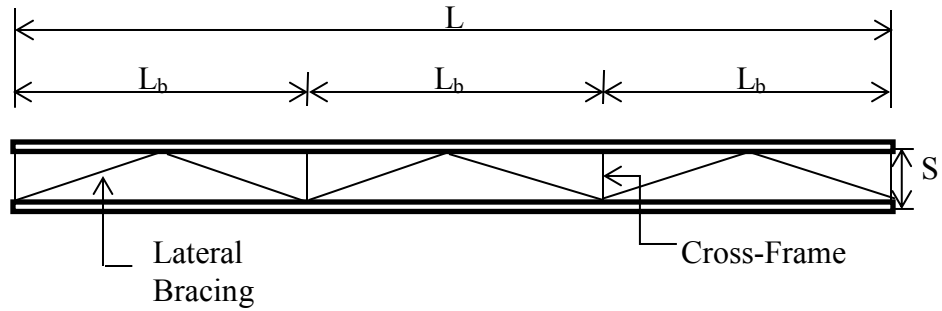


Figure 1.2 Plan view of twin girder system braced with combination of cross-frames and lateral bracing.

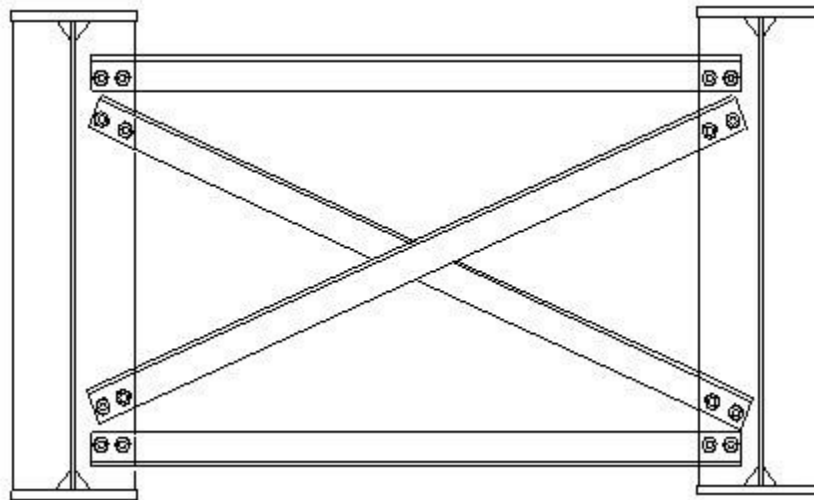


Figure 1.3 Typical cross-frame X-bracing arrangement.

Lateral torsional buckling of a single girder is a well understood phenomenon and its design is well anchored in both the Design of Steel Structures Code CSA S16 (2010) and CHBDC CSA S6 (2006). However, there is little technical information in either standard addressing the lateral stability of a girder system with only cross-frame bracing without the added lateral plan bracing. The question of interest is whether or not the unbraced length, can still be considered as L_b as shown in Figure 1.4, if only cross-frames are provided as bracing.

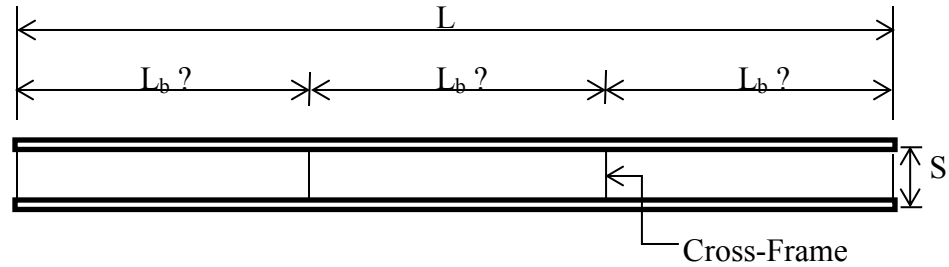


Figure 1.4 Plan view of twin girder system braced with only cross-frames.

1.2 OBJECTIVES AND SCOPE

This study is therefore motivated to investigate the efficiency of torsional braces provided by cross-frames for lateral torsional stability of plate girders. Both experimental and numerical analyses are included in the study. A parametric study using the verified numerical model is also conducted to investigate the additional parameters beyond the scope of the experimental program on the lateral torsional buckling capacity. The ultimate goal of this study is to provide some scientific information on the effective unbraced length of girder that can be used with the current design procedure CSA S6 (2006) for the lateral torsional buckling stability check when only cross-frames are used as bracing.

The detailed objectives of this research are:

1. To conduct a comprehensive literature review on research relevant to the lateral buckling of plate girders braced using cross-frames and a combination of cross-frames with lateral bracing.
2. To develop an experimental testing program to study the behaviour of twin beams braced using cross-frames and a combination of cross-frames and lateral bracing.
3. To develop a finite element model for the analysis of lateral torsional buckling of twin beams.
4. To validate the finite element results using experimental results and other results from available literature.

5. To conduct a parametric study to investigate the effect of parameters that include girder spacing, brace stiffness, and number of braces on the lateral torsional buckling capacity of twin girders.
6. To examine the current design standards, both CSA S16 (2010) and CSA S6 (2006), on the applicability of using the effective unbraced length in the girder stability consideration for girders with torsional braces only.

1.3 OUTLINE OF RESEARCH

This research commenced with a comprehensive literature review provided in Chapter Two. The experimental work conducted on twin beam systems is described in Chapter Three and the experimental results are presented in Chapter Four along with analytical results reported by others in literature. Chapter Five presents the development of the finite element model and its verification using the experimental results. The parametric study using the finite element model is presented in Chapter Six. Chapter Seven provides the summary, conclusions and recommendations from this research.

CHAPTER 2 LITERATURE SURVEY

2.1 BEAM BRACING

Beam bracing requirements were adapted and modified from research conducted on lateral bracing requirements for column buckling. The early research on lateral bracing requirements to prevent column buckling was conducted by Winter (1960). Winter showed that to effectively resist buckling a brace requires adequate strength and sufficient stiffness. In column buckling, the brace stiffness required to allow the column to achieve a load corresponding to Euler buckling between brace points is referred to as the ideal brace stiffness. A brace system that only provides a minimum stiffness equivalent to the ideal stiffness is not practical since the brace forces that are developed during buckling become infinitely large. To maintain the brace force in the range of 1% of the column axial force, the brace stiffness provided commonly exceeds the ideal brace stiffness by a factor of two. This theory has been verified for column buckling by Roddis *et al.* (2008) using finite element analysis. The bracing requirements developed by Winter (1960) also apply for both elastic and inelastic braced members. Gil and Yura (1999) verified the bracing method developed by Winter (1960) was applicable to inelastic members because the bracing requirements were independent of the material state.

Beam bracing, however, is a much more complex topic than column bracing due to the fact that beam buckling involves both flexure and torsion. In general, beam bracing is classified into two categories known as lateral and torsional bracing. Lateral bracing minimizes the amount of twist of the cross-section by restraining the beam's ability to displace laterally, while torsional bracing resists twisting of the cross-section directly by the use of a cross frame or diaphragm between adjacent beams (Yura, 2001).

2.1.1 Lateral Bracing

There are four categories of lateral bracing known as relative, discrete, continuous, and lean-on braces. Relative bracing systems are normally in the form of a truss situated on the compression flange of a beam as shown in Figure 2.1. This system is also referred to

as plan bracing which is studied in this research. The purpose of a relative brace system is to control relative lateral displacements between brace points. When a beam buckles, lateral displacements are prevented at the brace points resulting in sinusoidal buckling of the girder between the laterally braced locations. Discrete bracing systems provide lateral spring support at individual positions along the span of a beam. Lean-on brace systems rely on adjacent beams for lateral support during lateral buckling resulting in all beams buckling simultaneously. Continuous bracing systems have no unbraced length and provide full lateral support to the compression flange (Yura, 2001). The description of other bracing configurations can be found in Galambos (1998).

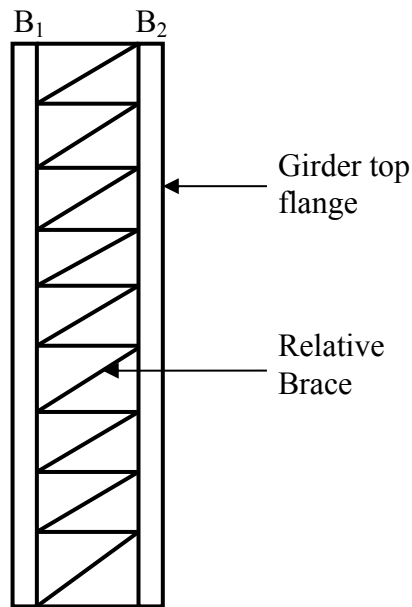


Figure 2.1 Plan view of relative brace system.

Yura (2001) showed that lateral bracing systems were most efficient to resist top flange loading effects when the bracing system was situated on the top (compression) flange. It was observed that the beam capacity increased linearly with a corresponding increase in bracing stiffness. He modified the Winter (1960) model to propose an equation for the calculation of the ideal lateral bracing stiffness. It was concluded that a beam will buckle in a global mode shape if the ideal brace stiffness was not provided.

2.1.2 Torsional Bracing

Torsional bracing systems can be described as either discrete or continuous systems. Diaphragms and cross frames are the two main types of discrete torsional bracing used in bridge construction, while a solidified concrete deck after construction is considered a continuous torsional brace. The effectiveness of using a torsional bracing system as a method of lateral support has been questioned by some engineers since both girders can still displace laterally under load. Yura *et al.* (1992) have proven theoretically and experimentally that girders may be treated as braced if twisting of the section is prevented (Galambos, 1998). Similar to lateral bracing, effective torsional bracing must have sufficient strength and stiffness (Helwig *et al.*, 1993). Yura *et al.* (1992) showed that unlike the case for lateral braces, top flange loading, the position of the brace on the cross section and the number of braces does not significantly affect the effectiveness of a torsional brace. A torsional brace has the same effectiveness whether it was situated on the tension flange or the compression flange of a beam.

Milner (1977) determined that the stiffness of a torsional brace is a function of the brace member stiffness, the beam web stiffness, and the beam to brace connection stiffness. Yura *et al.* (1992) modified the Milner (1977) expression to consider the effects of the girder cross-sectional distortion, as expressed in Equation [2.1]. It was found that the distortion could be minimized by installing web stiffeners at the brace locations or by installing torsional braces on both girder flanges (Yura, 2001). Helwig *et al.* (1993) indicated the magnitude of the torsional brace system stiffness was governed by the component with the smallest stiffness.

$$\frac{1}{\beta_t} = \frac{1}{\beta_b} + \frac{1}{\beta_{sec}} + \frac{1}{\beta_g} \quad [2.1]$$

where,

β_t is the resultant torsional stiffness of a single cross-frame,

β_b is the stiffness of the brace member expressed in Eq. [2.2],

β_{sec} is the stiffness due to cross-sectional distortion expressed in Eq. [2.3],

β_g is the girder web stiffness expressed in Eq. [2.4].

Yura *et al.* (1992) derived brace member stiffness expressions, β_b , for various cross-frame systems using elastic truss analyses. The tension cross frame system shown in Figure 2.2 requires both top and bottom chords along with a diagonal strut to link adjacent girders. This cross-frame stiffness calculation was adopted for the experimental program described in Chapter Three and the parametric study in Chapter Five. The brace stiffness for the tension cross-frame system is expressed in Equation [2.2].

$$\beta_b = \frac{ES^2h_b^2}{\frac{2L_c^3}{A_c} + \frac{S^3}{A_h}} \quad [2.2]$$

where,

- A_h is the area of horizontal cross-frame members,
- A_c is the area of diagonal cross-frame members,
- E is the modulus of elasticity,
- L_c is the length of diagonal cross-frame member,
- S is the spacing between adjacent girders,
- h_b is the height of cross frame.

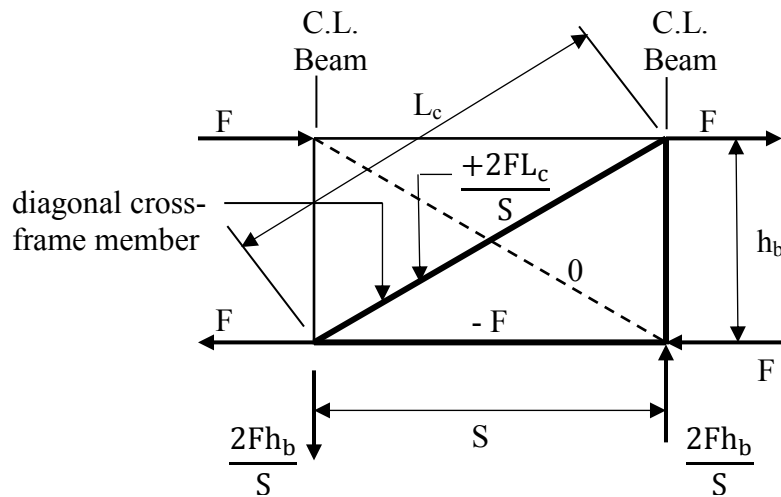


Figure 2.2 Tension cross-frame system (adapted from Yura, 2001).

The web stiffener arrangement displayed in Figure 2.3 can result in a torsional stiffness component due to cross-sectional distortion of the girder web which can be approximated using Equation [2.3]. This equation considers the potential reduction or increase in the cross-frame system stiffness due to web flexibility by means of a web stiffener. If full depth stiffeners were welded to the beam flanges in the cross-frame system, then the cross-sectional distortion component of the resultant torsional stiffness can be taken to be infinitely stiff (Yura, 2001).

$$\beta_{\text{sec}} = 3.3 \frac{E}{h_o} \left(\frac{(N + 1.5h_o)t_w^3}{12} + \frac{t_s b_s^3}{12} \right) \quad [2.3]$$

where,

- t_w is the beam web thickness,
- h_o is the distance between beam flange centroids,
- t_s is the stiffener thickness,
- b_s is the stiffener width.

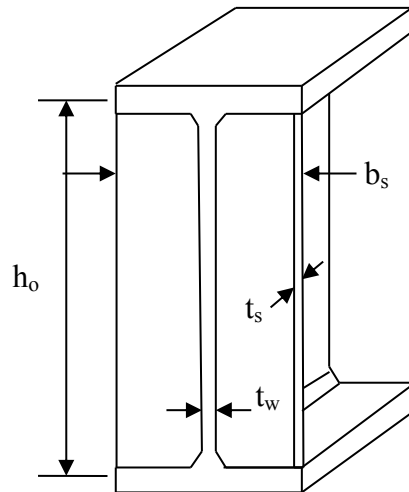


Figure 2.3 Typical full depth web stiffener at torsional brace location (adapted from Yura, 2001).

Helwig *et al.* (1993) developed a girder web stiffness approximation shown in Equation [2.4] for twin girders with one or multiple torsional braces along the span. The equation was verified using FEM for a twin girder system that was simply supported and free to warp with an applied uniform moment. The results of the study indicated that it was unconservative to neglect the girder web stiffness when evaluating the torsional brace system stiffness.

$$\beta_g = \frac{12S^2EI_x}{L^3} \quad [2.4]$$

where,

L is the beam length,

I_x is the beam strong axis moment of inertia.

Phillips (1990) found that initial imperfections such as out of straightness had a significant effect on the torsional brace stiffness and that increasing the initial imperfections resulted in a decrease in the critical buckling load. It was proposed that the stiffness of the brace member component in Equation [2.2] be modified to account for initial imperfections to the form shown in Equation [2.5].

$$\frac{1}{\beta_b} = \frac{1}{c_t\beta_b} \quad [2.5]$$

$$c_t = \frac{1}{1 + 3000 \frac{\Delta_o}{L}} \quad [2.6]$$

where,

c_t is the reduction factor for imperfections in torsional brace stiffness,

Δ_o is the initial out of straightness of the girder.

Yura (2001) provided the ideal torsional stiffness expressed in Equation [2.7] and stated that at least twice the ideal stiffness is required in practice to account for initial imperfections and to control anticipated torsional displacements and bracing forces.

$$\beta_{ti} = \frac{1.2LM_{cr}^2}{nEI_y C_b^2} \quad [2.7]$$

where,

- β_{ti} is the ideal stiffness of the torsional brace system,
- M_{cr} is beam buckling moment,
- n is number of intermediate torsional braces along the beam length,
- I_y is moment of inertia about y-axis for doubly symmetric section,
- C_b is the factor accounting for moment gradient.

The brace force expressed in Equation [2.8] is represented by a moment developed in the brace based on the assumption of a one degree initial imperfection in the girder and a brace stiffness that is at least twice the ideal brace stiffness (Helwig *et al.*, 1993). Finite element studies conducted by Wang and Helwig (2005) showed that the main factors which affect the magnitude of the brace force are the size and distribution of the initial imperfections.

$$M_{br} = F_{br}h_b = \frac{0.04LM_{cr}^2}{nEI_y C_b^2} \quad [2.8]$$

where,

- M_{br} is the brace moment,
- F_{br} is the brace force.

2.2 LATERAL TORSIONAL BUCKLING OF A BEAM

Timoshenko and Gere (1961) developed a general equation presented in Equation [2.9] to calculate the elastic critical buckling moment for a simply supported doubly symmetric beam with an applied uniform moment.

$$M_o = \frac{\pi}{L_b} \sqrt{EI_y GJ + \left(\frac{\pi E}{L_b}\right)^2 I_y C_w} \quad [2.9]$$

where,

M_o is the elastic critical buckling moment,

L_b is the unbraced girder length,

G is the shear modulus of elasticity,

J is the St.-Venant torsion constant,

C_w is the warping torsion constant.

Salvadori (1955) further proposed the use of a factor to account for the effects of moment gradient along the length of the beam using various loading conditions as shown in Equation [2.10].

$$M_{cr} = C_b M_{ocr} \quad [2.10]$$

For the case of a simply supported beam subjected to uneven end moments, the most commonly accepted formula by various design standards for C_b is:

$$C_b = 1.75 + 1.05\kappa + 0.3\kappa^2 \leq 2.5 \quad [2.11]$$

where,

κ is the ratio of the smaller to larger end moment, M_1/M_2 ; \pm depending on single or double curvature.

The C_b expression was further modified to account for location of the applied load with respect to the centroid of the beam. Galambos (1998) provided approximate solutions shown in Figure 2.4 based on conclusions from Nethercot and Rockey (1972). For top flange loading, $C_b = A/B$; $C_b = A$ for centroidal loading and $C_b = AB$ for bottom flange loading. In 2010, Ziemian published an updated version of the Guide to Stability

previously written by Galambos (1998) in which the same references are utilized for determining the C_b factor for a simply supported beam subject to varying load heights.

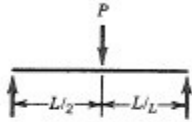
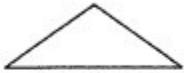
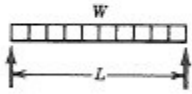
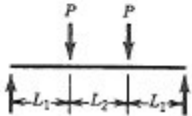
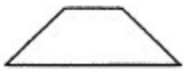
Loading	BMD	M	A	B
		$\frac{PL}{4}$	1.35	$1 - 0.180W^2 + 0.649W$
		$\frac{wL^2}{8}$	1.12	$1 - 0.154W^2 + 0.535W$
		PL_1	$1 + \left(\frac{L_1}{2L_1 + L_2}\right)^2$	$1 - 0.465W^2 + 1.636W$

Figure 2.4 Equivalent moment factor for concentrated and distributed loads (Galambos, 1998).

where,

W is the warping constant calculated in Equation [2.12].

$$W = \frac{\pi}{L} \sqrt{\frac{EC_w}{G}} \quad [2.12]$$

Wong and Driver (2010) observed that Equation [2.12] produced very conservative results in the calculation of the moment gradient factor for unbraced simply supported beams subjected to a point loading. However, the quarter point moment method proposed by Kirby and Nethercot (1979) had shown better results. Therefore, Wong and Driver (2010) adopted and modified the quarter point method expressed in Equation [2.13] to provide more accurate moment gradient values which represented the trends of various experimental data.

$$C_b = \frac{4M_{\max}}{\sqrt{M_{\max}^2 + 4M_a^2 + 7M_b^2 + 4M_c^2}} \leq 2.5 \quad [2.13]$$

where,

M_{\max} is the maximum bending moment of unbraced segment,

M_a is bending moment at one-quarter point of unbraced segment,

M_b is bending moment at midpoint of unbraced segment,

M_c is bending moment at three-quarter point of unbraced segment.

2.3 LATERAL TORSIONAL BUCKLING OF BEAMS WITH TORSIONAL BRACES

Taylor and Ojalvo (1966) developed a closed form solution to calculate the critical moment of a doubly symmetric beam subjected to a uniform moment with continuous torsional bracing. Equation [2.14] shows an expanded version of the equation with the known substitutions provided in detail in the paper. This expression expanded on a graphical solution previously developed that was limited to only a few bracing scenarios. In the case of discrete braces, an equivalent continuous torsional brace stiffness is required.

$$M_{cr} = \frac{\pi}{L} \sqrt{EI_y GJ + \frac{\pi^2 E^2 I_y^2 h_o^2}{4L^2} + \frac{\beta_T L^2 EI_y}{\pi^2}} \quad [2.14]$$

where,

$$\beta_T = \frac{\beta_t n}{L} \quad [2.15]$$

β_T is the continuous torsional brace stiffness described in Equation [2.15].

β_t is the stiffness of a single torsional cross-frame calculated using Equation [2.1].

Phillips (1990) simplified Equation [2.14] to the form shown in Equation [2.16].

$$M_{cr} = \sqrt{M_o^2 + EI_y \beta_T} \quad [2.16]$$

where,

- M_o is the critical elastic buckling moment calculated using Equation [2.9] with the warping component (C_w) ignored in the calculation,
- β_T is the continuous torsional cross-frame stiffness expressed in Equation [2.14] which accounts for initial out of straightness as expressed in Equation [2.5].

Yura (2001) modified Equation [2.16] to consider the effects of cross-section distortion, moment gradient, and loading height on the critical buckling strength shown in Equation [2.17]. To accommodate the effects of imperfections, the factor to account for loading height was doubled. The effects of cross-sectional distortion were accounted for by using the continuous torsional cross-frame stiffness expressed in Equation [2.15].

$$M_{cr} = \sqrt{C_{bu}^2 M_o^2 + \frac{C_{bb}^2 \beta_T EI_{eff}}{C_T}} \leq M_y \text{ or } M_p \quad [2.17]$$

where,

- C_{bu} is the moment gradient factor for a beam with an unbraced length of L ,
- C_{bb} is the moment gradient factor for a braced beam with an unbraced length of L_b ,
- C_T is a variable to account for loading height; $C_T = 1.2$,
- I_{eff} is the effective moment of inertia about the beam's y-axis which is equal to I_y for a doubly symmetric beam,
- M_y is the yield moment,
- M_p is the plastic moment.

Roddis *et al.* (2008) conducted a case study on the South Snyder River Bridge in Nebraska where excessive deflections were observed in twin plate girders during placement of the concrete bridge deck. The girders had a span of 45.7 m and were

interconnected using cross-frames at a spacing of 7.7 m. It was concluded the cross-frame stiffness was insufficient and that a cross-frame stiffness of three times the provided brace stiffness was required to achieve buckling between torsional braces. Therefore, the excessive deflections were a result of girder instability due to inadequate bracing stiffness. Finite element analysis of a single girder from the Snyder River Bridge indicated that using the unbraced length of beam as the distance between the torsional braces can only be achieved when the cross-frames act as stiff braces (Roddis *et al.*, 2008).

Nguyen *et al.* (2010) developed an analytical method using the energy method for strength and stiffness requirements of I-girders with discrete torsional braces. It was reported that the method compared well with finite element results presented by Yura (2001) and Trahair (1993). However, the method involved solving a series of differential equations and was considered cumbersome to use for design.

2.4 BEAMS WITH COMBINED LATERAL AND TORSIONAL BRACING

Phillips (1990) proposed an approximation (Equation [2.18]) to calculate the critical buckling moment of a beam braced with both lateral and torsional bracing. This combined the contributions of both the continuous lateral and torsional brace stiffness with the elastic critical buckling moment presented in Equation [2.9]. Phillips (1990) verified this equation using finite element analysis.

$$M_{cr} = \sqrt{\left(M_o^2 + \frac{P_y^2 h_o^2 A}{4}\right) (1 + A) + \beta_T EI_y} \leq M_y \quad [2.18]$$

where,

- M_o is the critical elastic buckling moment calculated using Equation [2.9] with the warping component (C_w) ignored in the calculation,
- P_y is the axial force in the beam due to flexure,
- A is a value calculated in Equation [2.19],

- c_L is a reduction factor for imperfections in lateral brace stiffness (Equation [2.20]),
- β_L is the continuous lateral brace stiffness (Equation [2.21]),
- A_{br} is the cross-sectional area of the lateral brace,
- L_{br} is the length of the lateral brace.

$$A = \frac{L^2}{\pi} \sqrt{\frac{.67c_L\beta_L}{EI_y}} \quad [2.19]$$

$$c_L = \frac{1}{1 + 1500 \frac{\Delta_o}{L}} \quad [2.20]$$

$$\beta_L = \frac{A_{br}E}{L_{br}} \times \frac{n}{L} \quad [2.21]$$

2.5 GLOBAL LATERAL BUCKLING OF A GIRDER SYSTEM

Kozy and Tunstall (2007) conducted an investigation regarding a twin girder bridge that showed large amounts of lateral displacement during the installation of the deck formwork. It was indicated the girders were susceptible to lateral torsional buckling failure with a global or system buckling mode. Finite element method was used to analyze various bracing methods and it was observed that the brace forces were in excess of the suggested 1% or 2% of the beam compressive flange force by AISC for the design of bracing members.

Yura *et al.* (2008) also acknowledged that the global buckling mode may occur when torsional bracing systems are solely used to restrain twist and lateral movement of the compression flanges of twin beams. The global buckling of the system was found to be entirely dependent on the geometry of the twin beams. Yura *et al.* (2008) conducted a finite element study of a doubly symmetric twin girder system that was subjected to uniform moment with the girders braced using cross-frames. The lateral bending rigidity of the twin girder system was expressed as $2EI_yGJ$. The torsional rigidity of the system

contained three components referred to as the St. Venant shear stresses of the individual flanges, warping stresses that are a result of lateral bending of the flanges and warping stresses developed from the vertical bending about the strong axis of the twin girder system which is also known as system warping. The torsional rigidity is expressed in Equation [2.22].

$$\frac{2EI_y h_o^2}{4} + \frac{2EI_x S^2}{4} \quad [2.22]$$

Yura *et al.* (2008) presented a closed form solution to calculate the elastic global lateral buckling moment of a twin girder system shown in Equation [2.23]. This closed form solution represents a maximum global buckling moment of a twin-girder system. To ensure adequate cross-frame stiffness, it was recommended that twice the ideal torsional brace stiffness be provided.

$$M_g = 2 \frac{\pi}{L_g} \sqrt{EI_y GJ + \frac{\pi^2 E^2 I_y}{4L_g^2} (I_y h_o^2 + I_x S^2)} \quad [2.23]$$

where,

L_g is girder length,

M_g is the global buckling moment of twin girder system.

All section properties from Equation [2.23] are based on a single girder. The global critical buckling moment per girder would be one half of the value calculated for M_g . Additional investigations concluded the moment gradient factor for a single girder was applicable to the twin girder setup while the top flange loading effects were negligible. It was also identified that cross-frame stiffness can influence the buckled shape of the girders by allowing the girders to buckle globally or by forcing the girders to buckle between the torsional brace locations as shown in Figure 2.5. When twin girder specimens fail in global buckling, the cross frame size and spacing provide minimal effect. The theories presented by Yura *et al.* (2008) were developed without the use of an

experimental testing program to verify the closed form solution and the finite element results.

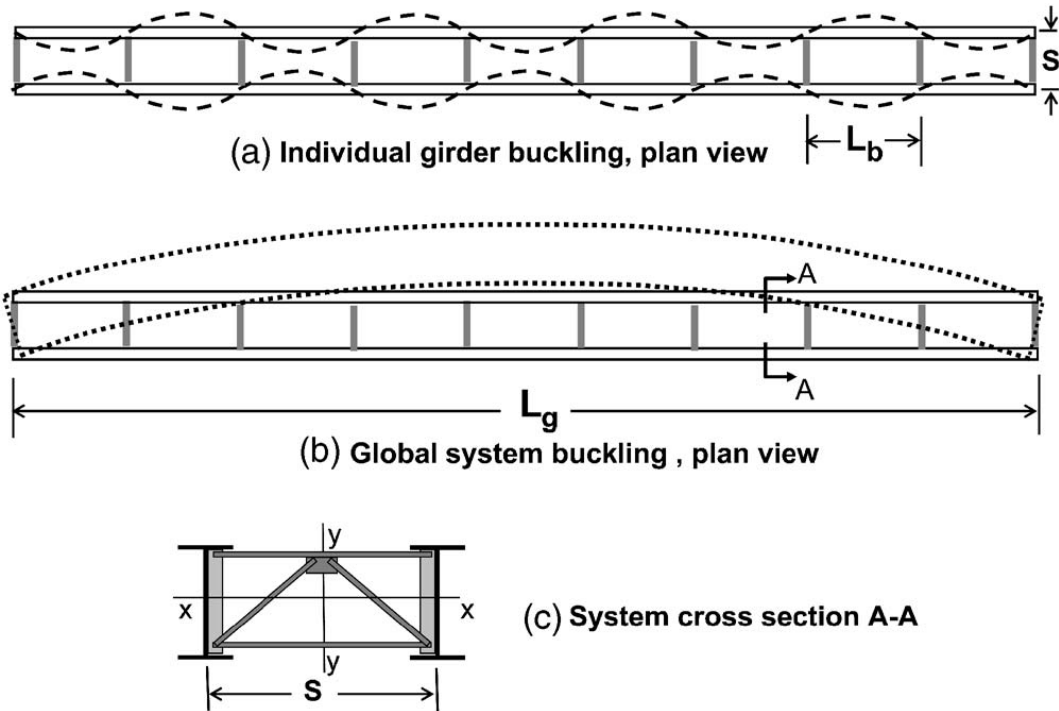


Figure 2.5 Buckling modes of twin girders with discrete torsional braces (Yura *et al.*, 2008).

Zhao *et al.* (2010) verified work presented by Yura *et al.* (2008) using a finite element method with a variety of girder arrangements. The investigation focused on deep plate girders which included parameters such as span length, girder spacing, girder section properties, cross-frame size, and cross-frame spacing. The finite element results were in good correlation with the previous results presented using Equation [2.23]. Zhao *et al.* (2010) suggested that the capacity of a twin girder system is governed by the maximum allowable girder span, minimum number of cross-frames along the span, and the minimum cross-frame stiffness.

Coffelt (2010) investigated the behavior of twin girder systems that were subjected to both dead and winds loads. Buckling analyses were conducted using finite element method to determine if buckling of cross-frames could occur prior to buckling of the girder system if lateral loads were applied to the girder. It was found that the primary

buckling mode for simply supported beams with a depth-to-girder spacing ratio less than 0.5 was global buckling of the girder system. When applying a lateral load to the windward girder of a twin girder system, the lateral stiffness of a twin girder system was determined approximately to be $2EI_y$ as suggested by Yura *et al.* (2008). Coffelt (2010) also acknowledged that buckling of the braces was highly unlikely prior to girder buckling, but twin girders with large spacing between girders have the highest risk of buckling the brace members.

2.6 CODES AND STANDARDS

2.4.1 CSA S16 (2010)

The Design of Steel Structures Code, CSA S16 (2010), adopts Equation [2.9] to determine the elastic critical moment of a simply supported beam subjected to strong axis bending without continuous lateral support to the compression flange. A moment gradient factor, ω_2 , expressed in Equation [2.24] was applied to the critical elastic moment. Wong and Driver (2010) suggested that the moment gradient factor can be calculated using the quarter point method in Equation [2.13].

$$M_u = \frac{\omega_2 \pi}{L_u} \sqrt{EI_y GJ + \left(\frac{\pi E}{L_u}\right)^2 I_y C_w} \quad [2.24]$$

To achieve stability in the plane of buckling for a member, CSA S16 (2010) suggests that braces supporting members against buckling be designed to resist 2% of the compressive force at each brace point. An additional stipulation indicates this method is only effective when the displacement of the brace does not exceed the initial misalignment of the beam. No explicit provisions are provided for the stiffness requirement of a lateral brace unless a detailed analysis of a beam system is conducted to compare the lateral displacement of the brace with respect to the initial imperfection of the beam.

CSA S16 (2010) also suggests that torsional brace systems should be proportioned for beams that are required to resist torsional forces. However, it is not directly indicated

whether the 2% rule is applicable for the design of the members which compose the torsional bracing system, such as a cross-frame, although it does indicate the brace member must be sufficient to transfer the forces that are developed in the braces. It has become a custom in standard practice to provide web stiffeners at the locations of torsional and lateral bracing as a means to limit web distortion. Clause 14.5 details the design considerations of web stiffeners, namely sufficient width-to-thickness ratios, moment of inertia, gross area, and the connection to the web and compression flange to transfer forces to the braces.

2.4.2 CSA S6 (2006)

CHBDC CSA S6 (2006) provides the same design guidelines for simply supported doubly symmetric beams subjected to flexure as the Design of Steel Structures Code CSA S16 (2010).

For the design of intermediate cross-frames and lateral bracing, CHBDC CSA S6 (2006) adopts the Winter (1960) model where both the cross-frames and lateral bracing must be designed to resist only 1% of the compression flange force of the beam at the braced location in addition to lateral loads they attract. Again, no stiffness requirement is clearly provided.

2.4.3 AISC 360 (2010)

AISC 360 Specification for Structural Steel Buildings (2010) provides an equation for the calculation of the elastic critical buckling stress as shown in Equation [2.25]. AISC presents the critical buckling resistance in the form of a critical stress instead of the critical moment as previously described for CSA S16 (2010). Although expressed in terms of stress, AISC Equation [2.25] in essence produces nearly identical critical moment values as CSA S16 (2010) and S6 (2006) Equation [2.24] with moment gradient considered.

$$F_{cr} = \frac{C_b \pi^2 E}{\left(\frac{L_b}{r_{ts}}\right)^2} \sqrt{1 + 0.078 \frac{Jc}{S_x h_o} \left(\frac{L_b}{r_{ts}}\right)^2} \quad [2.25]$$

where,

- F_{cr} is the critical plate buckling stress,
- L_b is the distance between lateral braces,
- h_o is the distance between flange centroids,
- J is the St. Venant torsion constant,
- r_{ts} is the effective radius of gyration calculated in Equation [2.26],
- c is a coefficient equal to 1.0 for doubly symmetric I-shapes,
- C_b is a lateral torsional buckling modification factor for non-uniform moments diagrams expressed in Equation [2.27],

$$r_{ts}^2 = \frac{\sqrt{I_y C_w}}{S_x} \quad [2.26]$$

$$C_b = \frac{12.5M_{max}}{2.5M_{max} + 3M_a + 4M_b + 3M_c} \quad [2.27]$$

AISC indicates that beam bracing requires sufficient strength and stiffness if it is to be used to define the unbraced length of a member. Table 2.1 presents the beam brace requirements for lateral and torsional braces from Appendix 6 of AISC 360 (2010).

Table 2.1 AISC Bracing Requirements (2010).

Brace Type	Strength Requirement	Stiffness Requirement	Equation
Lateral Brace	$P_{rb} = \frac{0.008M_r}{h_o}$	$\beta = \frac{1}{\phi} \left(\frac{4M_r}{L_b h_o} \right)$	[2.28]
Torsional Brace	$M_{rb} = \frac{0.024M_r L}{nC_b L_b}$	$\beta_T = \frac{1}{\phi} \left(\frac{2.4LM_r^2}{nEI_y C_b^2} \right)$	[2.29]

where,

- M_r is the flexural strength of the beam,
- C_b is the equivalent moment factor expressed in Equation [2.27],
- P_{rb} is the axial strength of brace,
- M_{rb} is the flexural strength of the torsional brace,
- h_o is the distance between flange centroids,
- ϕ is the material resistance factor (1.0 for this research).

CHAPTER 3 EXPERIMENTAL PROGRAM

3.1 GENERAL

The experimental program was designed to study the lateral torsional stability of twin beams with different arrangements of lateral and torsional bracing systems. Due to time constraints, only two specimen configurations were considered: 1) two beams tied with only cross-frames; and 2) two beams tied with both cross-frames and plan bracing. The test results are analyzed and discussed in the context of the bracing effect on the critical buckling moment and are also used to validate the numerical model that was developed concurrently with the experimental program.

3.2 TEST SPECIMEN

The test specimen used in the experimental program was scaled down by a factor of four to have similar geometric characteristics to a twin-girder bridge that would be encountered in practice. The practical plate girders considered in this study were simply supported with a span of 40 meters. The overall depth of the girder was 1500 mm with 450 mm wide flanges that had a thickness of 40 mm. The girders were spaced at 3.4 meters with cross frames spaced every 8 meters. The cross-frames were composed of L102×102×13 bracing that were bolted to web stiffeners. The web stiffeners were 200 mm wide plates that extended full depth of the girder with a thickness of 16 mm. The stiffeners were welded to the girder flanges and web. The plan bracing was WT155×26 members that were bolted to gusset plates located 100 mm below the beam top flange.

The test specimen consisted of two beams simply supported with a span of 11 meters. An overall view of the specimen is shown in Figure 3.1. A W360×33 section (Figure 3.2) was selected rather than a fabricated I-beam to reduce the associated fabrication costs. Table 3.1 compares the geometric properties of the real girder and the scaled beam which shows that the slenderness ratio and the span-to-depth ratio of both beams were comparable. The W360×33 section was also a Class 1 section that would prevent the test specimen from failing prematurely by local buckling of the flanges or web. The spacing

of the two beams was determined to be 800 mm to maintain the girder spacing to girder depth ratio provided in Table 3.1.

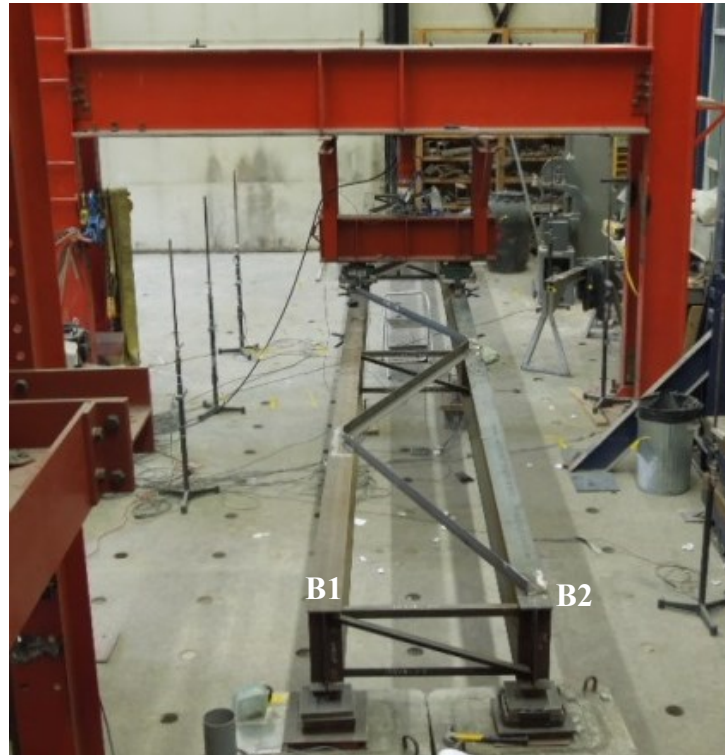


Figure 3.1 Overall view of the test specimen.

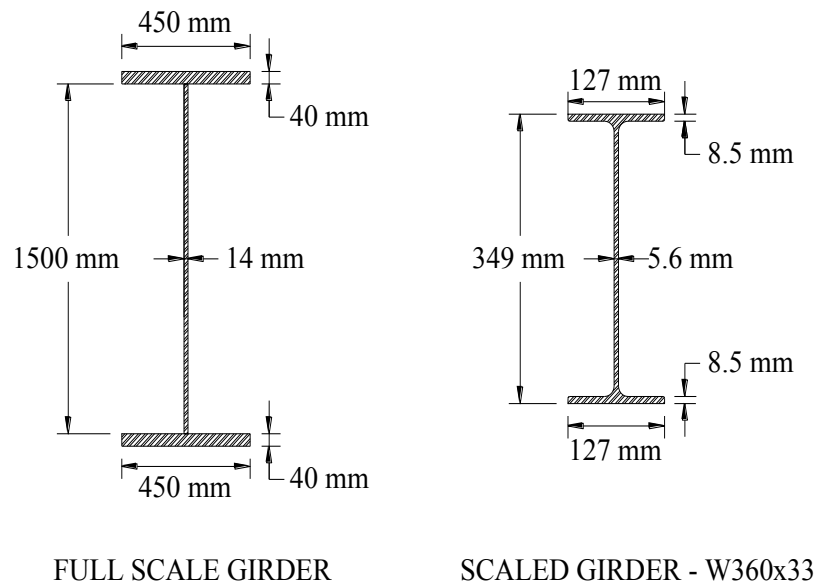


Figure 3.2 Practical and scaled specimen beam.

Table 3.1 Geometric configuration comparison.

	Full Scale Design	Scaled Test Specimen
Slenderness of beam's weak axis, λ_y	410	416
Span-to-depth, L/d	26.7	31.5
Spacing-to-depth, S/d	2.27	2.29

The cross-frame members were scaled to be proportionate with the W360×33 beams while maintaining adequate strength to resist buckling forces as per CSA S6 (2006). The spacing of the cross-frame systems were selected to achieve buckling of the specimen beams within the desired elastic stress range. As shown in Figure 3.3, the cross-frame system was composed of 60 mm wide full depth stiffeners that were 8 mm thick and welded to the beam flanges and webs. By providing full depth stiffeners that were welded to the beams, it was believed that cross-section distortion is prevented at the cross-frame locations. The cross-frame members were designed to resist both tension and compression during beam buckling. With the scale of the cross-frames in the specimen, it was not practical to achieve bolted connections. Therefore, 5mm fillet welds were used to attach the bracing members to the stiffeners.

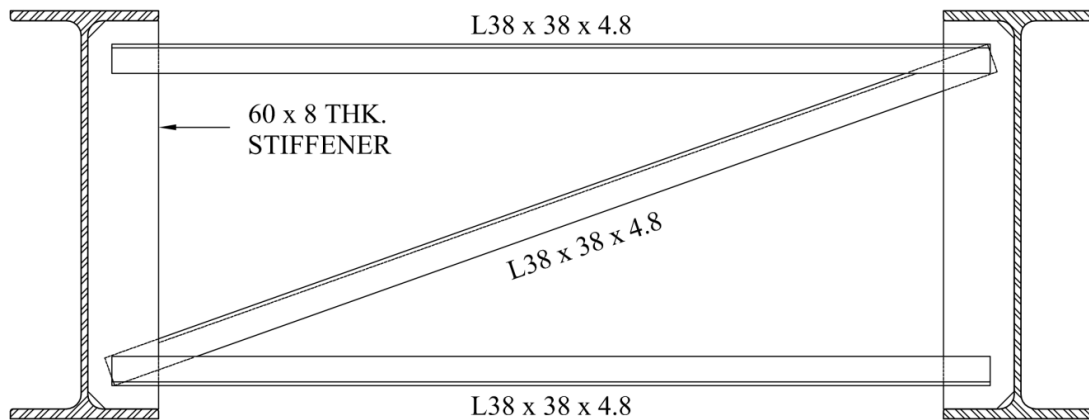


Figure 3.3 Typical cross-frame system.

The plan bracing system consisted of L64×64×4.8 angles which were installed in a Chevron (V-shape) arrangement between the cross-frame braces as displayed in Figure 3.4. Due to the scale of the specimen, the angles were welded to the top surface of the compression flanges.

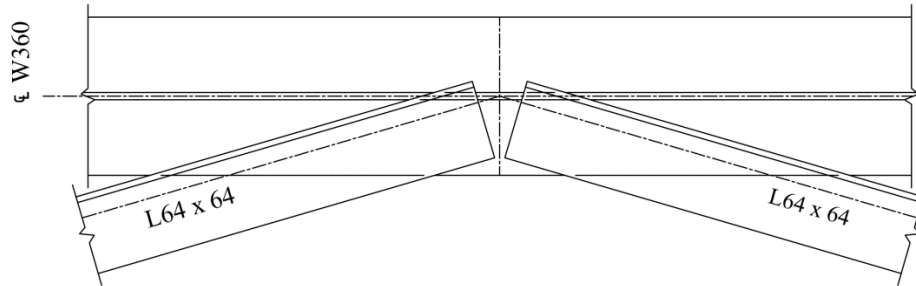


Figure 3.4 Typical compression flange bracing detail.

3.3 TEST SCHEME

Two specimen configurations were considered in the experimental testing program as described in Table 3.2.

Table 3.2 Specimen configurations.

Specimen	Configuration
C1-1	Twin beams with only cross-frame bracing
C1-2	Twin beams with only cross-frame bracing
C2	Twin beams with cross-frame bracing and plan bracing

Specimen C1 refers to the configuration where two beams are connected using only cross-frames as shown in Figure 3.5, whereas specimen C2 refers to the case where two beams are connected with both cross-frames and plan bracing as shown in Figure 3.6. For test C1, the specimen was expected to reach its buckling load while remaining in the elastic stress range which would allow the specimen to be reused for test C2 where yielding of the material is expected. However, during the test of specimen C1, the specimen buckled in the inelastic range and significant plastic deformation was observed. The higher than anticipated buckling load value was attributed to frictional forces that developed in the midspan loading system. The frictional force behaved as a lateral

restraint at the beam midspan which caused beam 2 (Figure 3.5) to buckle inelastically. A close physical inspection and strain readings indicated that beam 1 was still in the elastic range after the removal of the applied load. It was decided that beam 2 be replaced with a new beam and that test C1 be repeated again with specimen C1-2. In the test of C1-2, the loading setup at the interface of the load distribution beam and the top flange of the test beam was modified to reduce the friction. The detailed discussion of this modification is provided in Section 3.4.

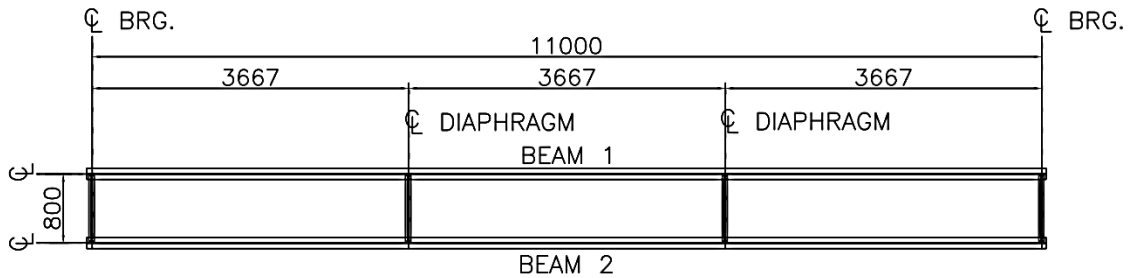


Figure 3.5 Plan view of specimen C1 with vertical cross-frames.

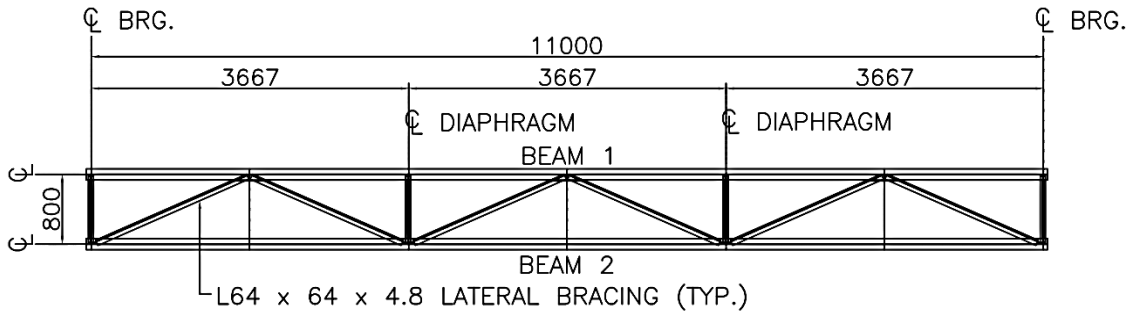


Figure 3.6 Plan view of specimen C2 with cross-frames and plan bracing.

3.4 TEST SETUP

The schematic test setup for the loading of the twin beam system is shown in Figure 3.7. The downward vertical load was applied through a load distribution beam to the specimen at its midspan. A 500 kN hydraulic ram acting against an existing loading frame was used to apply the load. The load distribution beam was a stiffened W360×79 that was braced against potential lateral movement during testing using steel knife edges. The knife edges were welded to the existing loading frame. The crosshead beam (W621x241) of the existing frame was simply connected to the columns (W360x51) with

two sets of three 40 mm A325 bolts at each end. The columns of the frame were welded to 35 mm thick baseplates that were in turn anchored to the concrete floor with four 50 mm diameter bolts. The ram was mounted to the underside of the crosshead beam through a 25 mm thick plate. The applied load from the hydraulic ram was distributed through the load distribution beam and transferred to the top flange of each test specimen beam through a roller and pivot assembly as shown in Figure 3.7.

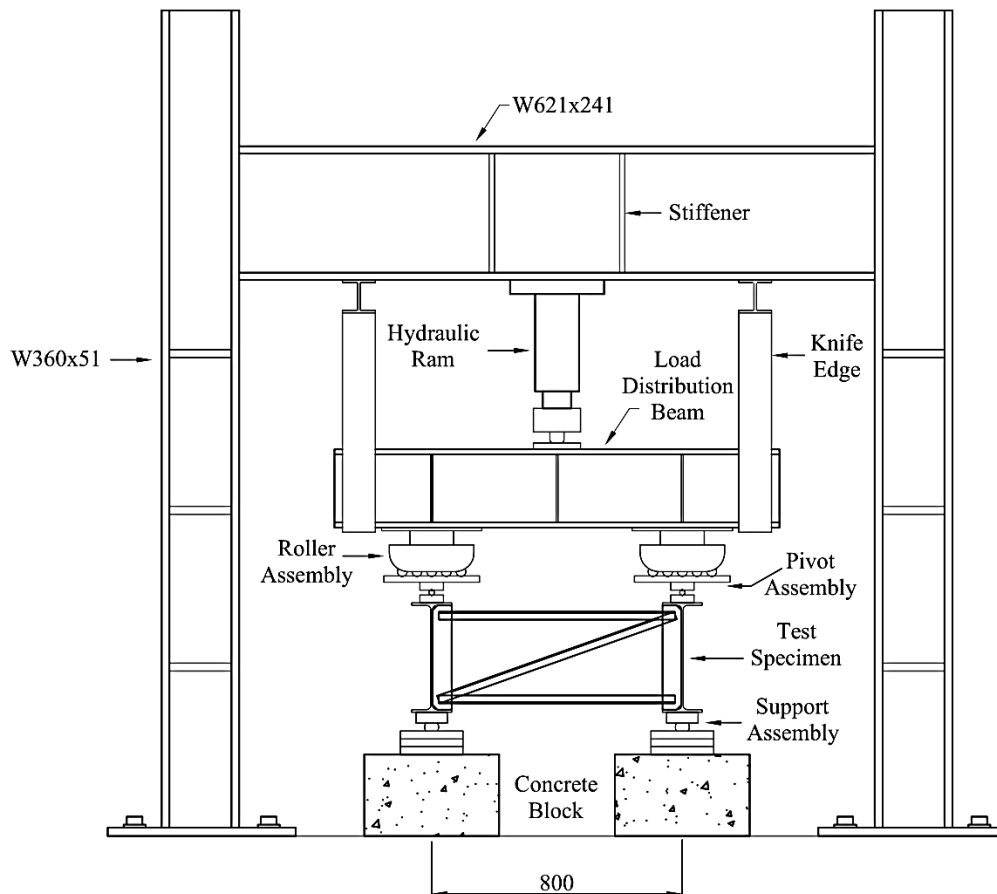


Figure 3.7 Schematic test setup.

The roller and pivot assemblies were designed to allow the beam top flange to translate and rotate freely during testing. To achieve the desired movements, the roller and pivot assemblies were required to have minimal friction between the rollers and the plate of the pivot assembly. Any appreciable friction between these surfaces would result in lateral restraint for the beams.

The initial roller assembly used in the testing program is shown in Figure 3.8. The roller assembly consisted of five 25 mm diameter rollers connected together through a rectangular cage made of steel flat bars. The rollers were high strength steel with a polished surface. However, this assembly still showed appreciable friction when subjected to compression which resulted in a critical buckling load of the specimen that was higher than the analytical value. After several modifications, it was determined that commercial Hilman rollers were best suited for the roller assembly. The modified system is shown in Figure 3.9. The Hilman roller assembly was suspended in a track that could rotate around bearings to minimize frictional forces while maintaining the compression forces exerted on the rollers. The bearing plate in the pivot assembly was surface grinded to provide a smooth flat finish. A lubricant was applied between the surface of the Hilman rollers and the pivot plate and on the surface of pivot roller to further reduce friction during testing.

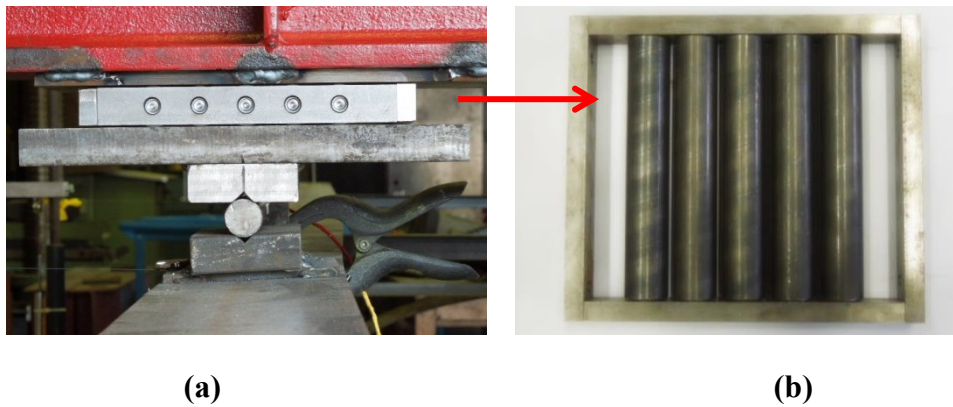


Figure 3.8 Specimen C1-1 (a) Pivot assembly; and (b) roller assembly.

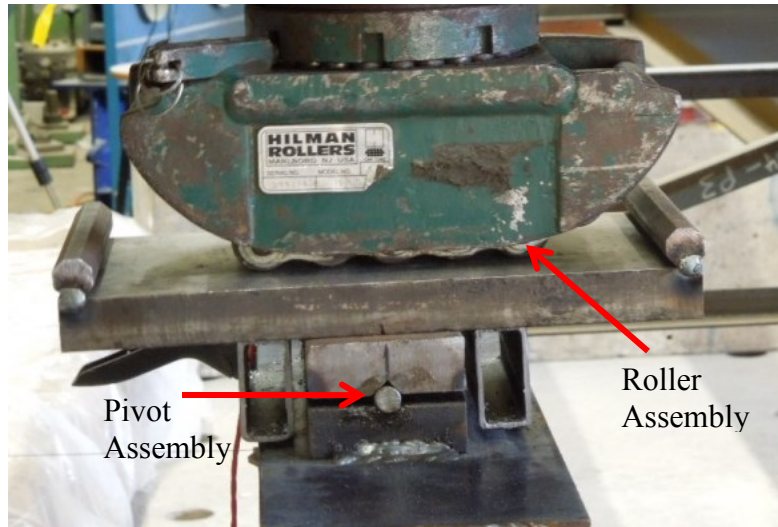


Figure 3.9 Specimen C1-2, C2 roller and pivot assemblies.

The beam ends were supported on bearing assemblies situated on concrete blocks. The bearing assembly simulated the simple support conditions. The requirement for translation in the longitudinal and transverse directions for each support is illustrated in Figure 3.10. The translational requirements were achieved by constructing roller assemblies similar to the one in Figure 3.8(b). To achieve translation in the longitudinal direction, transverse direction or both directions simultaneously, uni-directional and multi-directional bearing assemblies were fabricated. The uni-directional bearings shown in Figure 3.11 had a single roller assembly while the multi-directional bearings shown in Figure 3.12 had a roller assembly for each direction of translation. The test specimen was kept at the same elevation at all four bearing supports by maintaining the total height of the bearing assemblies.

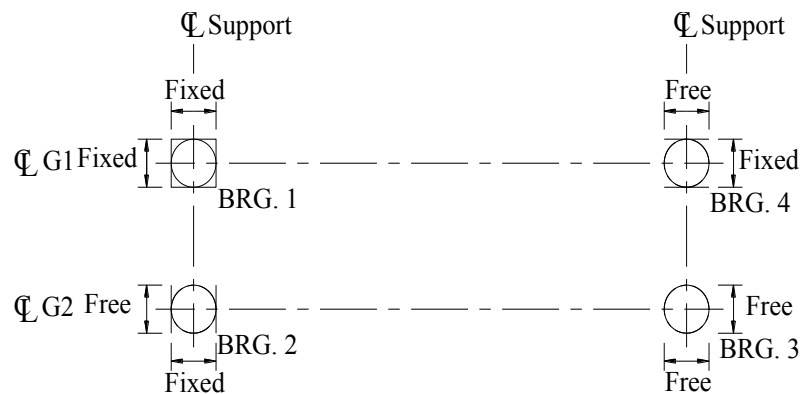


Figure 3.10 Bearing assembly movements.

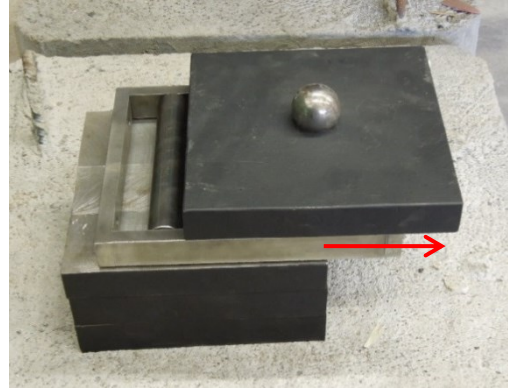


Figure 3.11 Uni-directional bearing assembly.

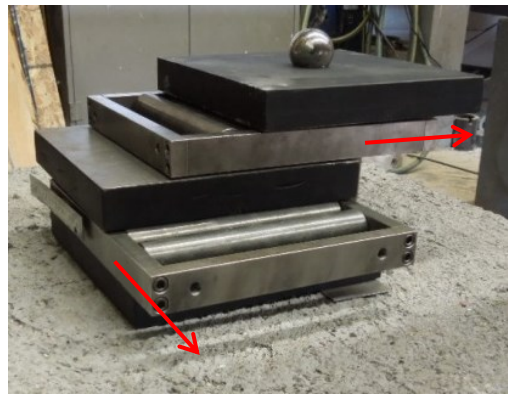
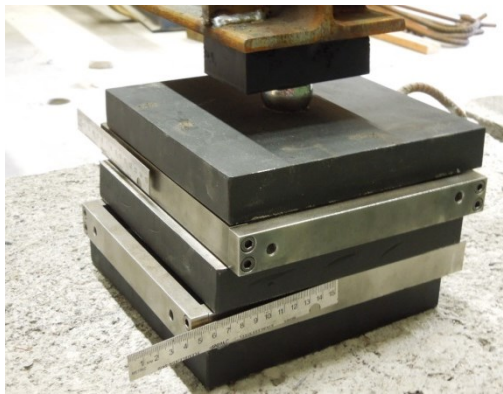


Figure 3.12 Multi-directional bearing assembly.

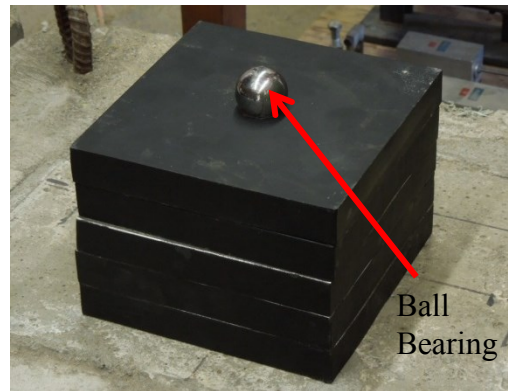
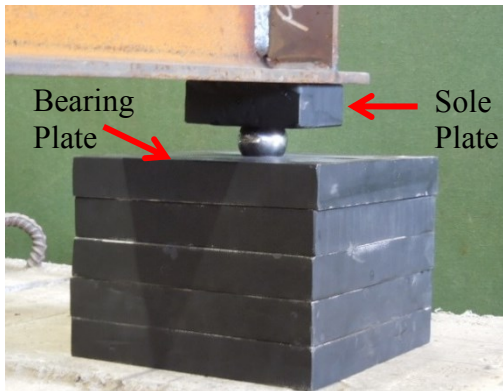


Figure 3.13 Pinned bearing assembly.

The beam rotation at bearing locations was achieved using ball bearings as shown in Figure 3.13. The ball rested in spherical grooves that were machined into both the beam sole plate and the bearing plate.

3.5 INSTRUMENTATION AND DATA ACQUISITION

The load applied to the specimen was recorded using a 200 kN load cell that was attached to the hydraulic ram. The distribution of the applied load from the distribution beam to the specimen was monitored using electrical strain gages. The webs of both beams were instrumented with the electrical strain gages at the supports shown in Figure 3.14. The readings from these strain gages were used to verify equal load distribution between the beams and all four supports. The strain gages had micro-measurement precision.

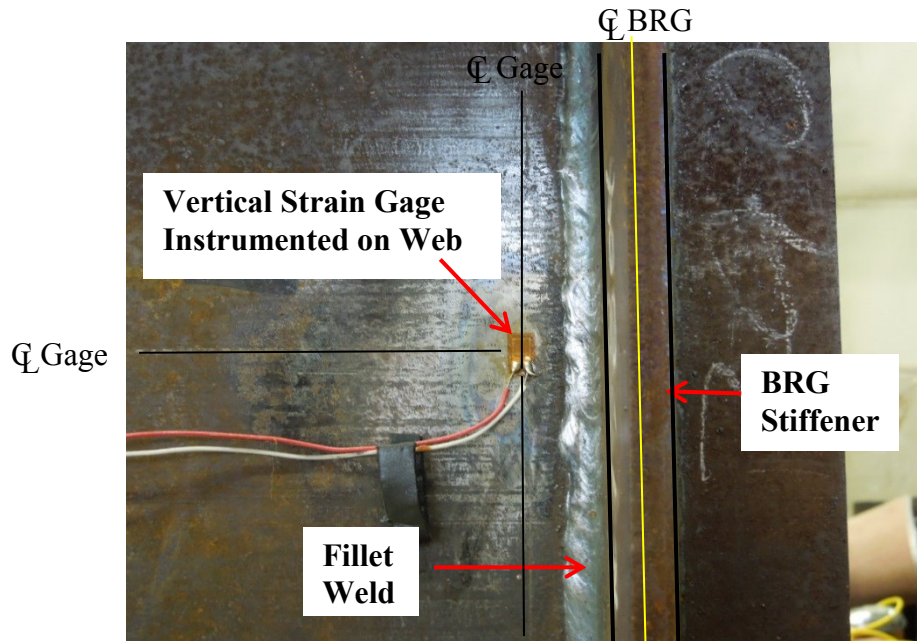


Figure 3.14 Strain gages instrumented at beam supports.

At midspan, six strain gages were installed on the top and bottom flanges of both beams to record the normal strains in the flanges. A single strain gage was installed at the center of the bottom flange while two strain gages were installed on the top flange at either side of the beam web. A typical midspan instrumentation for strain gages labelled as “S” is provided Figure 3.15. Strain gages were installed on the underside of the top flange to accommodate installation of the pivot assembly from the loading setup. The strain readings will indicate whether the beams have buckled elastically or inelastically. Since the top flange strain gages were installed on the underside of flange, the recorded top flange strain values would then be interpolated to the section’s extreme compression

fibre. Two additional strain gages were also installed on the top and bottom flanges at the quarter point of a single beam to supplement the midspan strain readings.

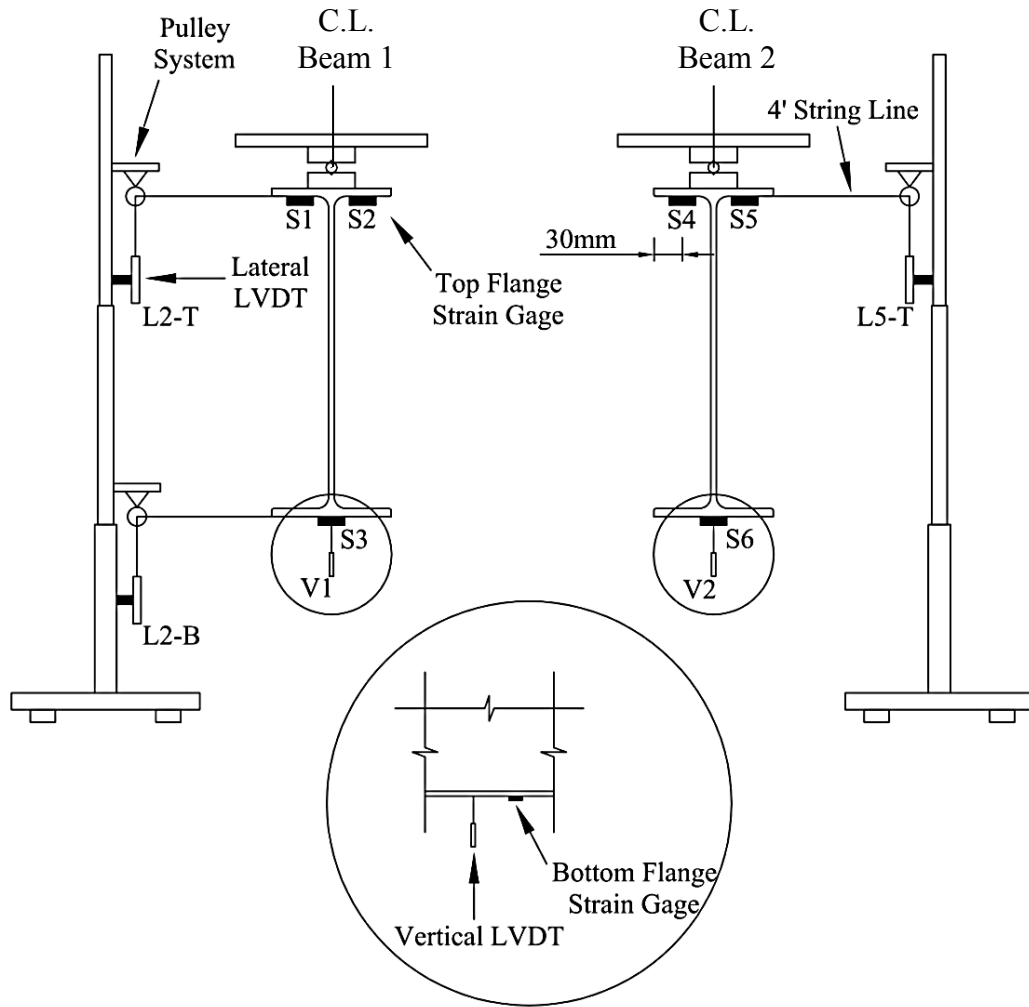


Figure 3.15 Typical midspan instrumentation schematic.

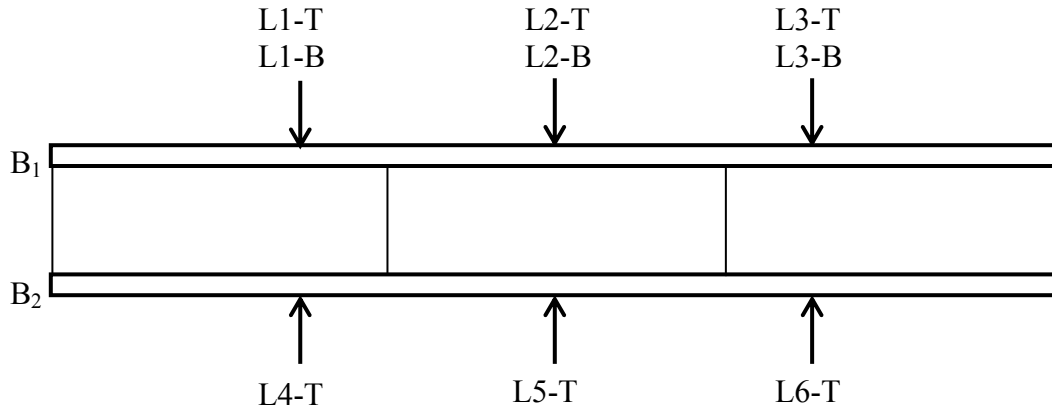
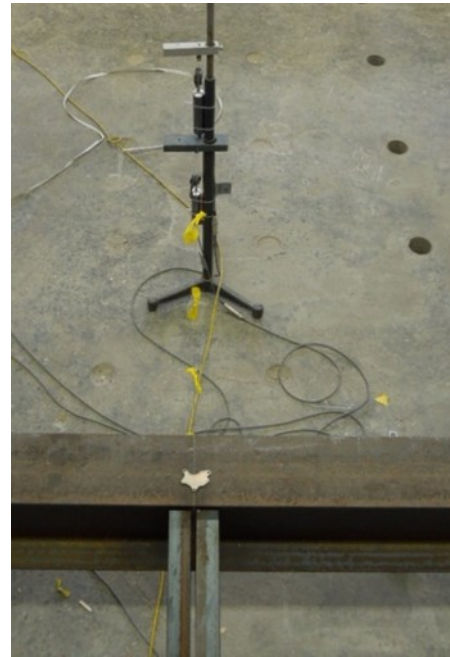


Figure 3.16 Plan view of experimental specimen showing LVDT locations on specimen.

Lateral and vertical displacements were recorded for both beams using Linear Variable Differential Transducers (LVDTs) as shown in Figure 3.15 labelled as “L” and “V” respectively. The midspan vertical displacements were measured on the underside of each beam (Figure 3.17a). The lateral displacements were recorded at the midspan and quarter point locations (Figure 3.17b). The LVDTs were instrumented on the top and bottom flanges of beam 1 and only on the top flange of beam 2 as displayed in Figure 3.16. The top and bottom flange displacement readings provided a method to monitor the twist of the section at various locations. Inclometers were also installed on the top and bottom flanges of both beams at midspan. The inclinometers were used to verify the amount of beam twist which was calculated using the LVDTs. A typical inclinometer can be observed in Figure 3.18. The load, deflections and strain readings were recorded using an electronic data acquisition system throughout the loading history of each test.



(a)



(b)

Figure 3.17 (a) Vertical displacement; and (b) lateral displacement.



Figure 3.18 Midspan inclinometer.

3.6 TEST PROCEDURE

The specimen was aligned over the end supports and under the loading beam such that the load would be applied at midspan of both beams. The support bearing assemblies at

the beam ends were shimmed to ensure the specimen had the same top flange elevation at each beam end. The load distribution beam was aligned and the roller assemblies were aligned above the center of the beam webs. Any initial eccentricities between the center of the roller assemblies and the centers of the beam webs were corrected.

After the alignment of the load distribution beam, the initial imperfections such as out-of-straightness of the beam web and lateral sweep of the beams were measured and recorded. The initial out-of-straightness of the beam web was measured by dropping a plumb-bob from the edge of the beam top flange to bottom flange. A 3 mm differential in flange location was recorded for both beams as shown in Figure 3.19.

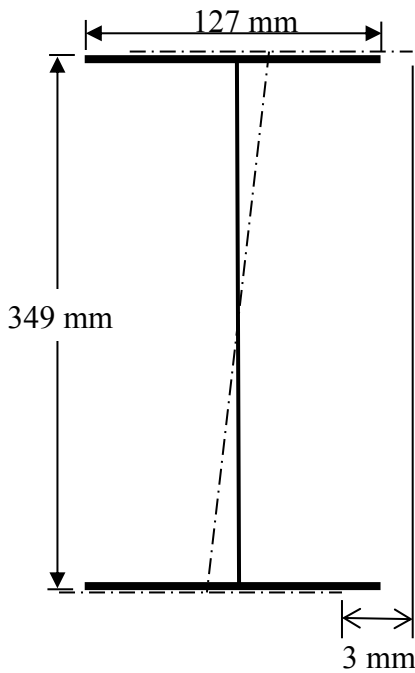


Figure 3.19 Initial out-of-straightness of beam webs.

The lateral sweep of the beams was measured by running a string along the edge of the beam flange from one end to the other. The distance between the string line and beam flange at one meter station intervals was measured using a set of Vernier calipers. This process was repeated for both the flanges and web of each beam. A maximum lateral sweep of 9 mm was recorded at the midspan of each beam as shown in Figure 3.20. The measured initial imperfections fall within the allowable limits provided by CSA S16

(2010), where the maximum allowable sweep was calculated to be 22 mm for the beam span and a web out-of-straightness of 5 mm.

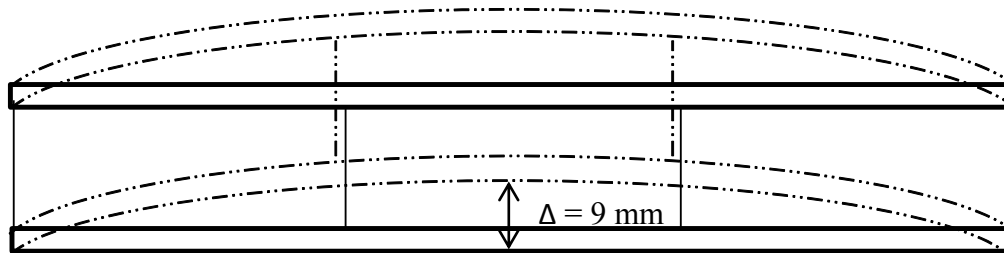


Figure 3.20 Initial lateral sweep of beams.

The initial location of the support bearing assembly rollers were recorded with respect to the top and bottom bearing plates to determine the global translation of the test specimen at the buckling load. Prior to actual testing, a preloading procedure was conducted where 20% of the predicted elastic critical buckling load was applied to the test specimen and then removed. This process was repeated twice to ensure that the specimen was “settled in” and all instrumentation devices functioned properly before testing. During testing, the specimen was loaded at a rate of 2.4 kN/min and the data was recorded at a scan rate of 1 hertz. The applied load was removed from the specimen when visible signs of buckling or yielding were observed.

3.7 TENSION TEST

Eight steel coupons were cut from a single beam of Specimen C1-1 since both beams were fabricated from the same mill stock. Additional eight coupons were cut from the replacement beam used in Specimen C1-2 and C2. For each beam, coupons consisted of 2 from each flange and 4 coupons from the web as shown in Figure 3.21.

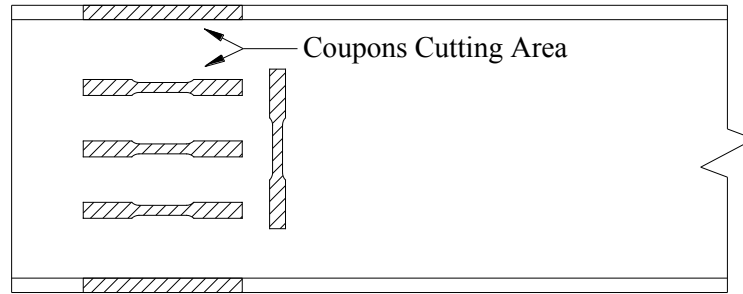
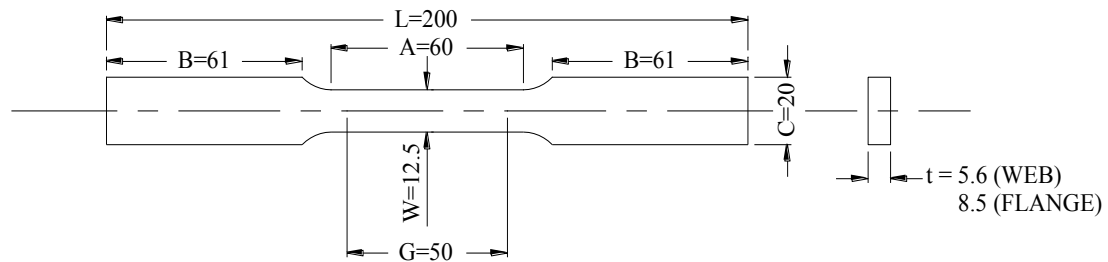


Figure 3.21 Tension coupon cutting scheme.

The coupons were milled in accordance with the ASTM Standard A370 (2012) for specimens with a gauge length of 50 mm as shown in Figure 3.22. The coupons were tested using an Instron universal testing machine with a capacity of 2000 kN as shown in Figure 3.23. The coupons were loaded at a constant rate of 3 mm/min and the elongation of each coupon was measured using a digital extensometer with a 50 mm nominal gauge length.



- G – Gauge Length, mm
- W – Width, mm
- T – Thickness, mm
- R – Radius of fillet, mm
- L – Overall length, mm
- A – Length of reduced section, mm
- B – Length of grip section, mm
- C – Width of grip section, mm

Figure 3.22 Tensile coupon dimensions.



Figure 3.23 Tension coupon test setup.

CHAPTER 4 EXPERIMENTAL RESULTS

4.1 MATERIAL PROPERTIES

The first beam stock consisted of beams from specimen C1-1 whereas the second beam stock consisted of the replacement beam for specimens C1-2 and C2. A summary of the material properties, including the modulus of elasticity E , yield stress f_y , and ultimate stress f_u , is provided for each coupon in Table 4.1. A typical stress-strain curve for a coupon that was removed from the flange of beam stock one is shown in Figure 4.1. The stress-strain curve did not show a pronounced yielding plateau; therefore, the yield strength was determined using the 0.2% offset method specified by the ASTM A370 Specifications (2012). Additional coupon stress-strain plots can be observed in Appendix A.

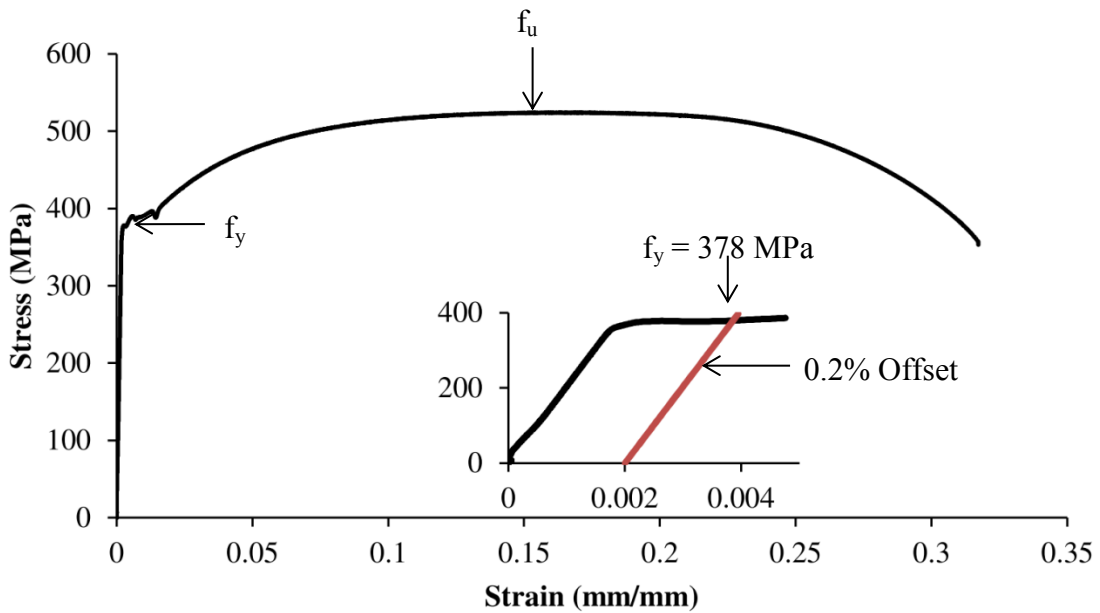


Figure 4.1 Coupon OF 2 stress-strain curve.

Table 4.1 Material properties.

Coupon No.	Beam Stock	Location	E (MPa)	f_y (MPa)	f_u (MPa)
OF 1	1	Flange	198684	378	503
OF 2	1	Flange	204293	378	524
OF 3	1	Flange	279434	396	525
OF 4	1	Flange	120631	386	528
mean			200761	385	520
OW 1	1	Web	197475	417	530
OW 2	1	Web	213306	421	530
OW 3	1	Web	192101	415	539
OW 4	1	Web	-	-	-
mean			200961	418	533
NF 1	2	Flange	240629	383	536
NF 2	2	Flange	234982	382	533
NF 3	2	Flange	202123	387	540
NF 4	2	Flange	-	-	-
mean			225911	384	536
NW 1	2	Web	207303	445	-
NW 2	2	Web	218417	454	550
NW 3	2	Web	202280	432	531
NW 4	2	Web	218564	444	544
mean			211641	444	542

The modulus of elasticity used in the later calculation for each specimen is listed in Table 4.2. The listed value for each beam is the average value of both the beam flange and web modulus results presented in Table 4.1.

Table 4.2 Specimen modulus of elasticity.

Specimen	Modulus of Elasticity (MPa)	
	Beam 1	Beam 2
C1-1	200861	200861
C1-2	200861	218776
C2	200861	218776

4.2 RESIDUAL STRESS

The residual stress distribution for the specimen beams was not experimentally obtained in this study. A commonly accepted residual stress distribution presented by Galambos and described in Figure 4.2 was assumed instead.

The peak residual stresses were calculated to be 115 MPa in compression at the flange tips and 43 MPa in tension at the flange to web junction. A yield stress of 385 MPa determined from the tension coupon tests for flanges was used to calculate these peak residual stress values. These values were used to monitor whether the specimen had reached the inelastic stress range.

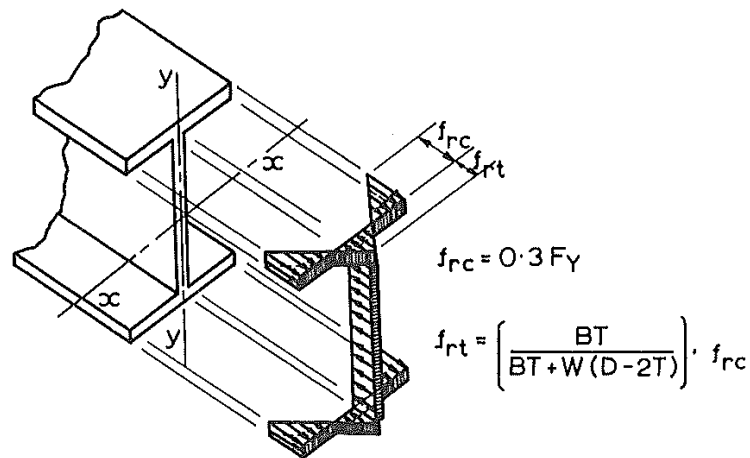


Figure 4.2 Simplified Residual Stress Pattern (Trahair *et al.*, 1972).

4.3 BUCKLING CAPACITY

Table 4.3 summarizes the results of specimens including the critical buckling load, mid-span top flange lateral displacement, Δ_L , mid-span vertical displacement, Δ_V , all taken at the buckling load, and the failure mode for each specimen. The critical buckling load, P_{cr} was defined as the load at which point the lateral displacement of compression flanges at midspan showed a rapid increase while the applied load remained roughly unchanged.

Table 4.3 Experimental results for test specimens.

Test Specimen	P_{cr} (kN)	$\Delta_{L,B1}$ (mm)	$\Delta_{L,B2}$ (mm)	$\Delta_{V,B1}$ (mm)	$\Delta_{V,B2}$ (mm)	Failure Type
C1-1	99.5	3.0	2.0	79.1	78.2	Inelastic Buckling
C1-2	72.2	8.6	2.0	62.2	56.8	Elastic Buckling
C2	145.3	1.6	1.8	133.0	127.9	Yielding/Web Buckling

The load versus midspan lateral displacement response for each specimen is presented in Figure 4.3 to 4.5 whereas the load vs. midspan vertical displacement response is presented in Figure 4.6 to 4.8. The respective buckling load of each specimen is also identified in the lateral displacement plots. The load vs. lateral displacement response of specimens C1-1 and C1-2 showed a rapid increase in displacement at the buckling load. At this point it is considered the beam has lost stability. However, the corresponding load versus vertical displacement responses remained almost linear up to the buckling load. This indicates that the failure of these two specimens was by buckling. On the other hand, the load versus vertical displacement response of specimen C-2 exhibited signs of non-linearity at the buckling load, indicating that yielding has occurred before the web buckled. A yielding load of 119 kN was defined using experimental strain data and vertical displacement readings. It is noted that specimens C1-2 and C2 exhibited slightly different load vs. vertical displacement responses. The vertical displacements recorded for each beam of specimen C1-2 deviated as loading increased whereas the beams of specimen C2 experienced nearly identical vertical displacements. It is believed that the presence of plan bracing resulted in a beam system that behaved as a unit vertically.

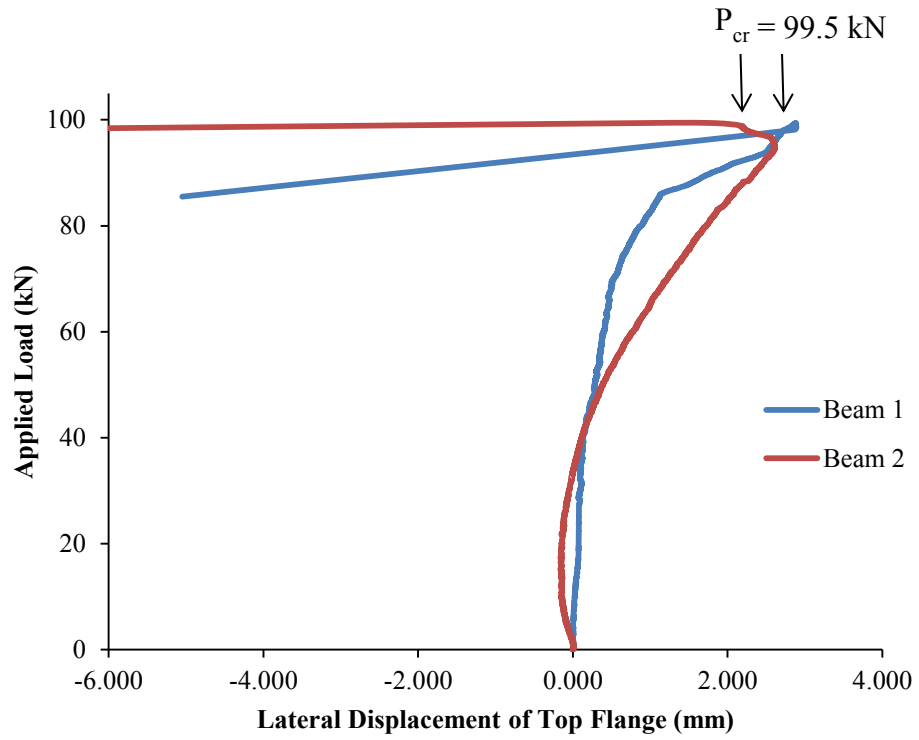


Figure 4.3 Specimen C1-1 load vs. midspan lateral displacement response.

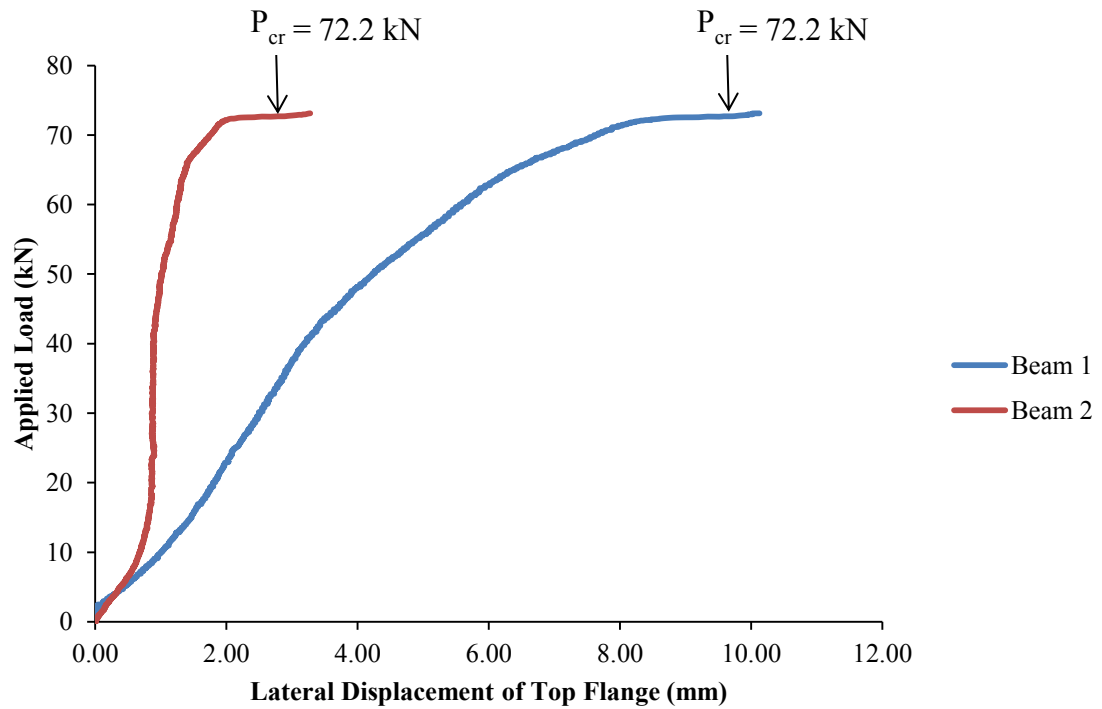


Figure 4.4 Specimen C1-2 load vs. midspan lateral displacement response.

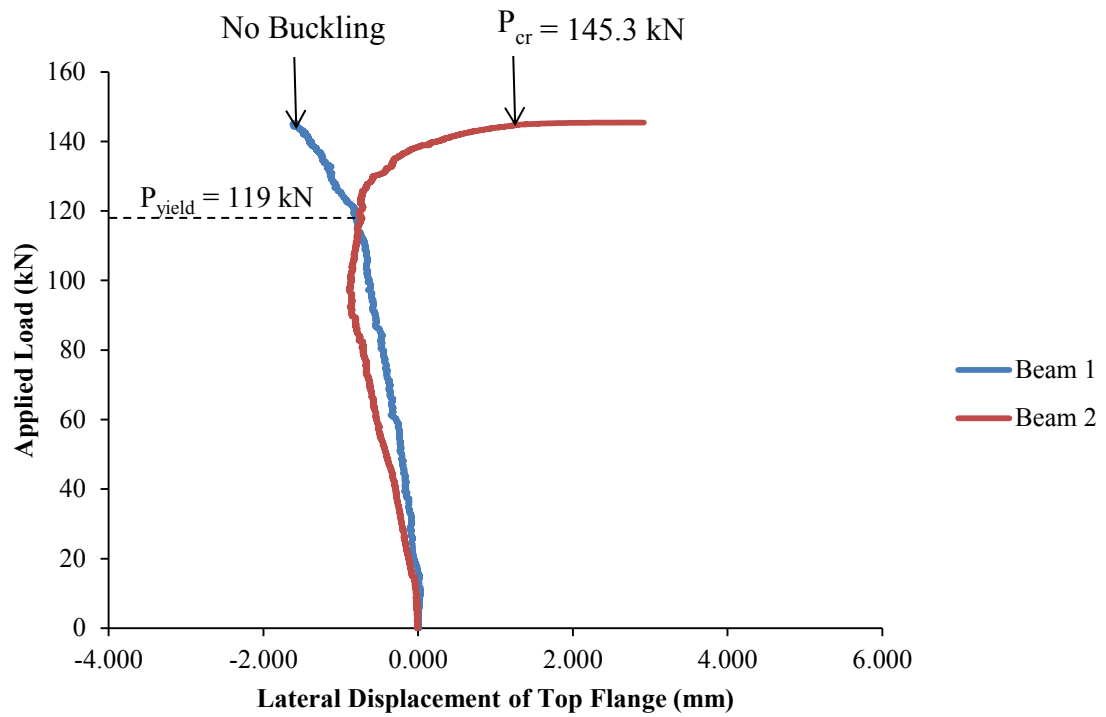


Figure 4.5 Specimen C2 load vs. midspan lateral displacement response.

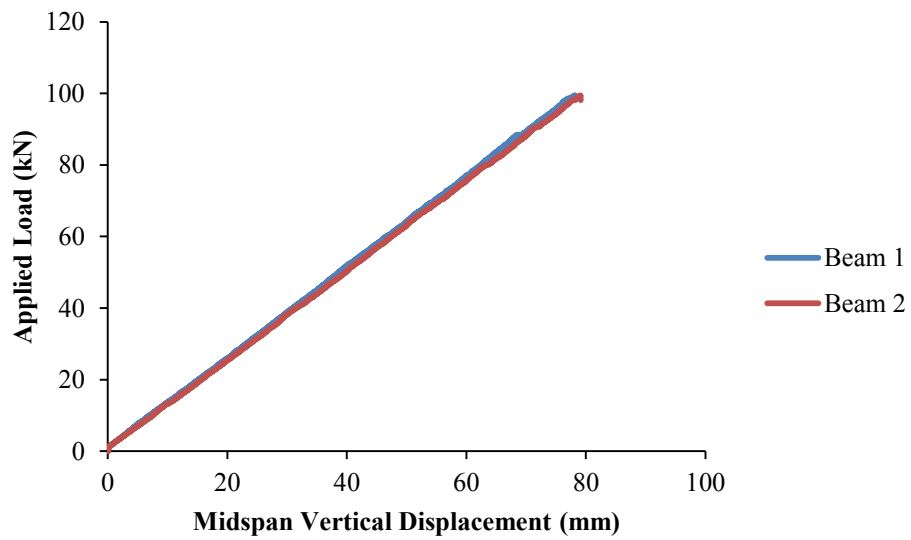


Figure 4.6 Specimen C1-1 load vs. midspan vertical displacement response.

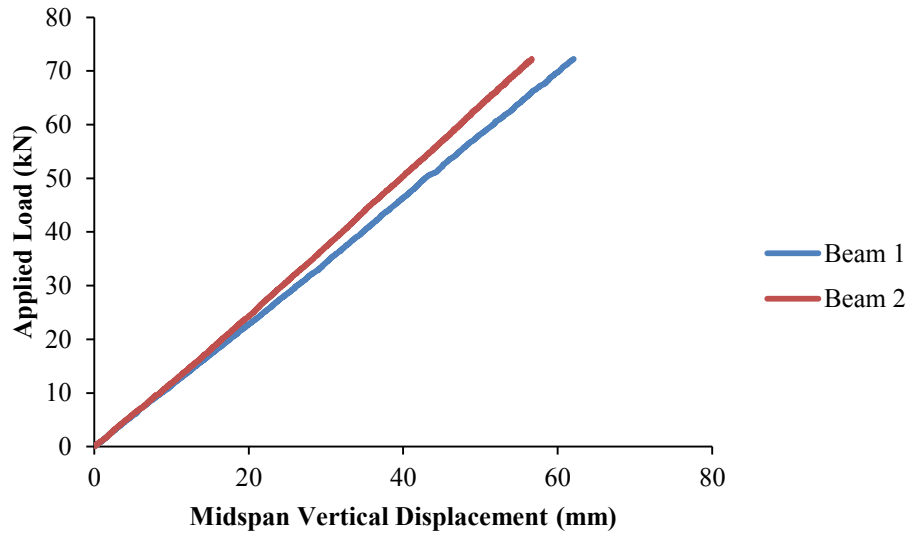


Figure 4.7 Specimen C1-2 load vs. midspan vertical displacement response.

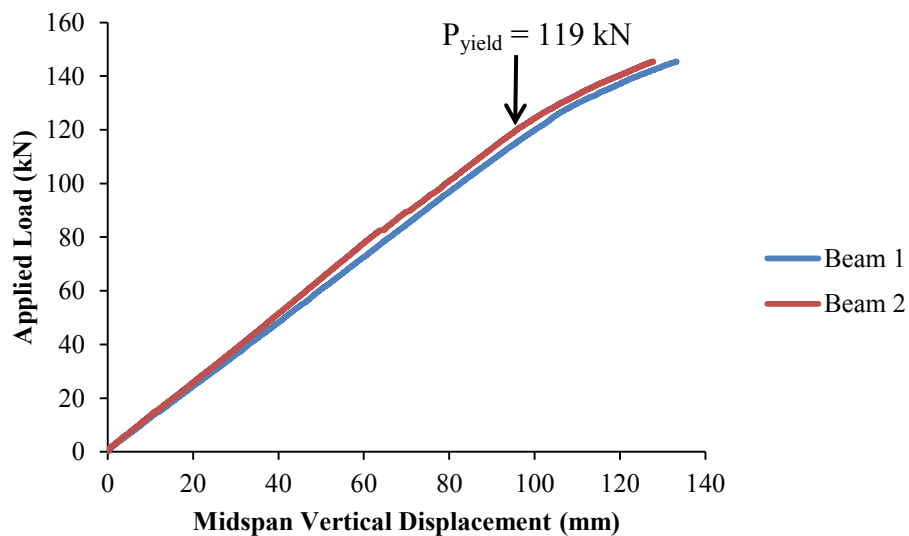


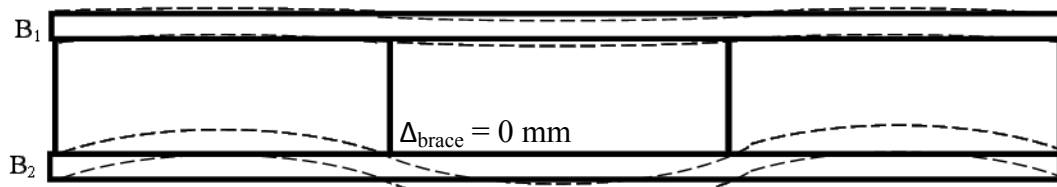
Figure 4.8 Specimen C2 load vs. midspan vertical displacement response.

Specimens C1-1 and C1-2 attained different buckling loads even though both specimens were tested with identical cross-frame bracing configuration. Specimen C1-1 attained 37.8% higher buckling load than specimen C1-2. As discussed in Chapter 3, the difference between these two specimens was the roller assembly that supports the load distribution beam. Also shown in Figure 4.3, little lateral displacement was recorded prior to buckling for both beams for specimen C1-1. It was believed the roller assembly used during testing of specimen C1-1 had exerted frictional forces that attributed to little

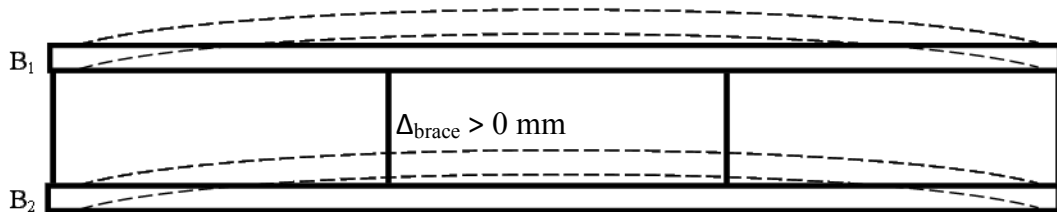
lateral movement of both beams prior to buckling. These frictional forces also contributed to a higher buckling load than specimen C1-2. The Hilman roller system used in specimen C1-2 is designed to generate minimal friction during movements of heavy loads. As shown in Figure 4.4, beam 1 showed a pronounced lateral displacement at buckling which indicates that a reduction in friction from the Hilman roller system was present. As a result of the reduced friction, the buckling load was within the anticipated range obtained from a finite element analysis. Specimen C2 shown in Figure 4.5 had little lateral displacement for both beams. This behaviour was anticipated since the plan bracing stabilizes the compression flanges. The addition of plan bracing to the cross-frame bracing (Specimen C2) provided a significant increase in the buckling capacity of the specimen. This increase in capacity is 101% when compared to specimen C1-2 which has only cross-frame bracing.

4.4 FAILURE MODES

The schematic views of the buckled shapes are shown in Figure 4.9 for all three specimens.



(a)



(b)

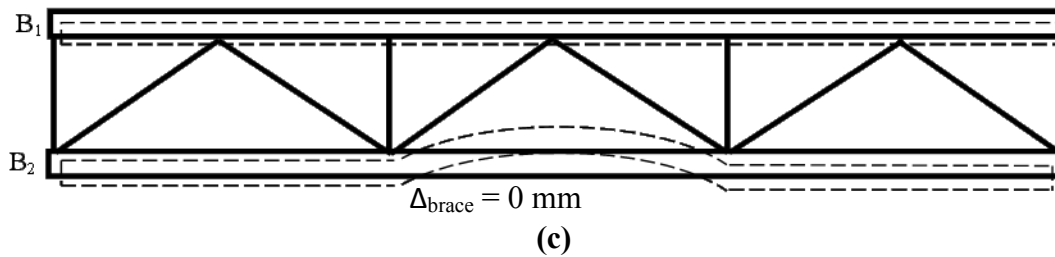


Figure 4.9 Buckled shape of specimen: (a) C1-1, (b) C1-2 and (c) C2.

For specimen C1-1 (Figure 4.9a), beam 2 (B_2) showed an evident sinusoidal buckled shape during experimental testing while beam 1 did not exhibit any evident signs of buckling. Therefore, load vs. lateral displacement responses were relied upon to verify the buckled shape of beam 1. A photograph of the failure mode is shown in Figure 4.10. The frictional forces exerted by the roller assembly at the loading point on the flanges are believed to attribute to this failure mode. The frictional force behaved as a lateral restraint at midspan of each compression flange causing the specimen to buckle at a higher mode resulting in a higher buckling capacity. The buckling of the beam 2 was in the inelastic range where yield lines were visible on the inside portion of the compression flange of the midspan segment situated between cross-frames as shown in Figure 4.11. The inclinometer readings indicate there was 0.5 degrees of rotation recorded about the longitudinal axis of the specimen at the top flange when buckling occurred. It was also noted that a 10 mm longitudinal translation was measured in the free end support bearing assemblies.



Figure 4.10 Deformed shape with sinusoidal buckling of specimen C1-1 post failure.



Figure 4.11 Yielding of specimen C1-1 beam 2 compression flange.

An expected global elastic lateral torsional buckling failure was achieved for specimen C1-2 after modifications were incorporated to reduce the frictional restraint in the roller assembly. The buckled shape of the test specimen was not visible due to the small lateral displacements of the compression flanges. The load vs. displacement responses were

relied upon to signify when the specimen had a sudden change in lateral stiffness as a result of lateral torsional buckling. Once buckling was thought to have occurred, the applied load was removed from the specimen to prevent the material from undergoing strain-hardening and failing from inelastic buckling. An inclinometer reading of 0.3 degrees was recorded for the top flange rotation when buckling occurred and an 8 mm longitudinal movement was measured in the free end support bearing assemblies.

Specimen C2 showed no apparent yield lines on the compression flange prior to failing by web buckling of the midspan region at the ultimate load. The specimen buckled between torsional cross frames in the segment of beam that was unbraced at midspan shown in Figure 4.12. This failure was catastrophic resulting in lateral buckling of both the girder flange and the web shown in Figure 4.13 with visible yield marks in the web and permanent deformations to both the compression flange and web. An inclinometer reading of 1.0 degrees was recorded for the top flange rotation when buckling occurred. No longitudinal movements were recorded for specimen C2 as a result of the specimen leaving the end support bearing assemblies when buckling occurred.

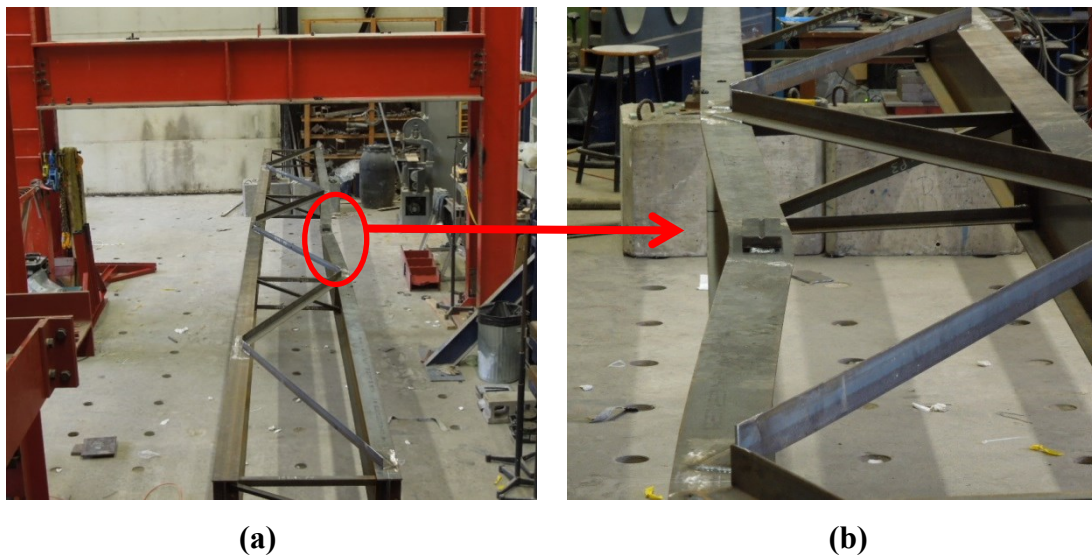


Figure 4.12 (a) Inelastic buckling of specimen C2; and (b) magnified view of inelastic buckling failure.



Figure 4.13 Local buckling of specimen C2 compression flange and web.

4.5 VERIFICATION OF TEST SETUPS AND INSTRUMENTATION

In this section, vertical displacement readings are verified with the calculated values, and strain gauge readings are used to verify the stresses developed in the specimen. The midspan vertical displacement results were verified by calculating the midspan displacement for a simply supported beam with a concentrated load at the beam midspan using Equation [4.1].

$$\Delta_v = \frac{PL^3}{48EI_x} \quad [4.1]$$

where,

- Δ_v is maximum midspan vertical displacement (mm),
- P is the load applied to the beam (N),
- L is the beam length (mm),
- E is the modulus of elasticity tabulated from Table 4.2 (MPa),
- I_x is the beam's strong axis moment of inertia (mm⁴).

The calculated vertical displacements are shown with the experimental results in Figures 4.14 to 4.16. It shows that the calculated vertical displacements are in good agreement with experimentally measured values when using the experimentally obtained modulus. Even for specimen C2, although the curve began to show nonlinearity due to yielding, the

calculated vertical displacement compared well with experimental values for a major portion of the curve.

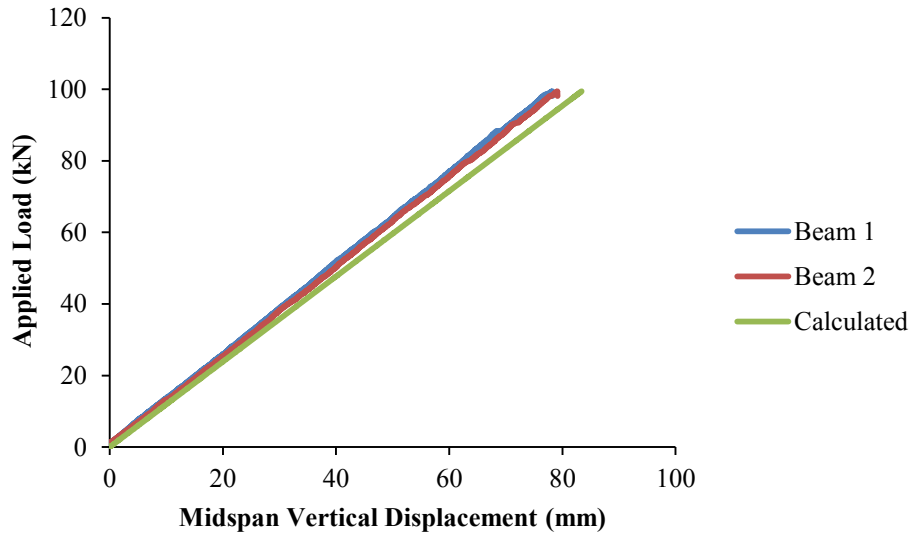


Figure 4.14 Specimen C1-1 comparison of calculated and experimental vertical displacements.

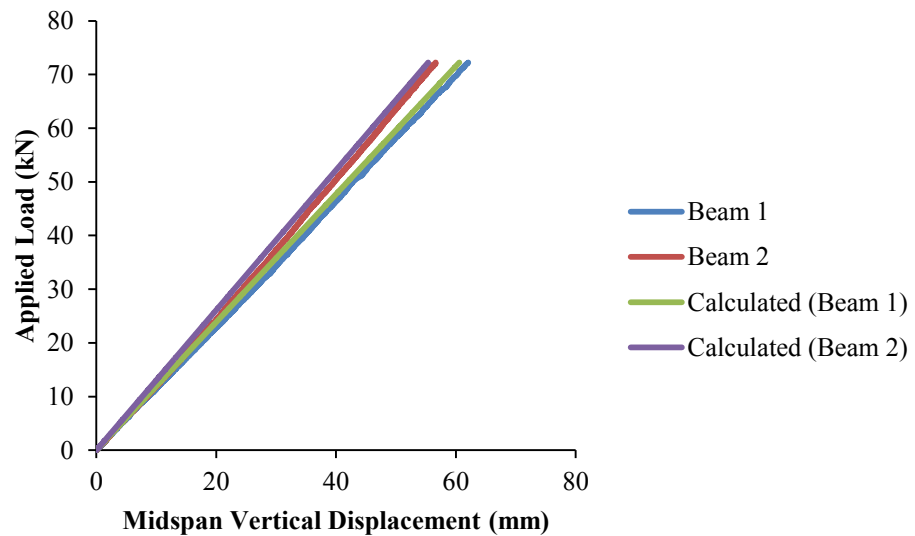


Figure 4.15 Specimen C1-2 comparison of calculated and experimental vertical displacements.

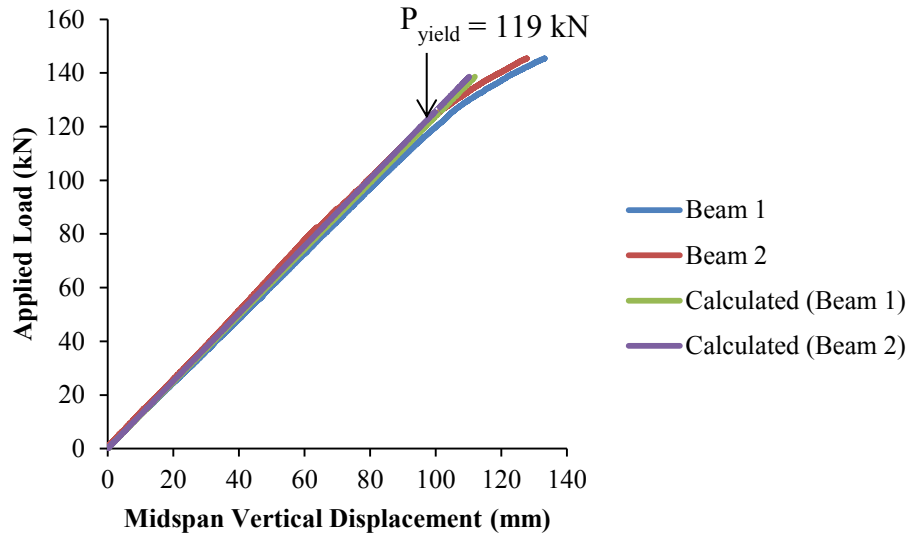


Figure 4.16 Specimen C2 comparison of calculated and experimental vertical displacements.

The distribution of the applied load to the two beams was also verified using vertical strains mounted in the beam webs at the end supports. As shown in Figure 4.17, the recorded vertical strains for Specimen C1-1 were within 5 microstrains at the beam ends under an applied load of 99.5 kN which is acceptable from a practical viewpoint. Similar strain readings were obtained for specimens C1-2 and C2.

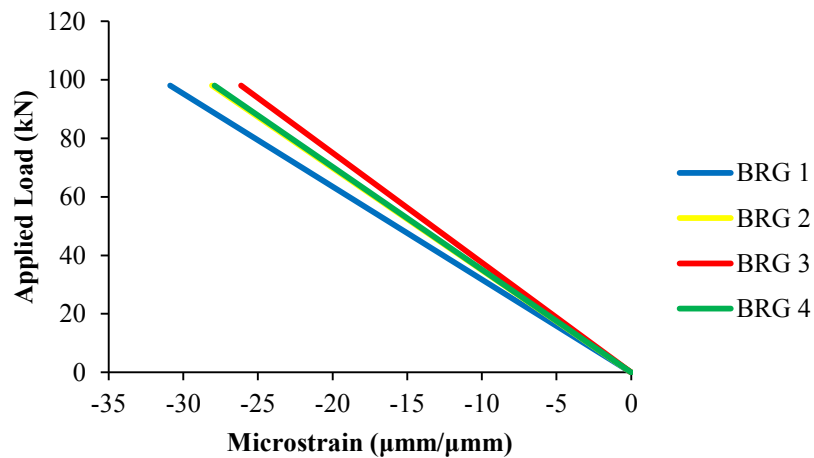


Figure 4.17 Specimen C1-1 vertical strains in webs of beam ends.

Strain readings were also obtained to monitor flexural stress at various locations along the length of the specimen as shown in Figure 4.18. The location 1 was situated 3 meters from the end of beam 2.

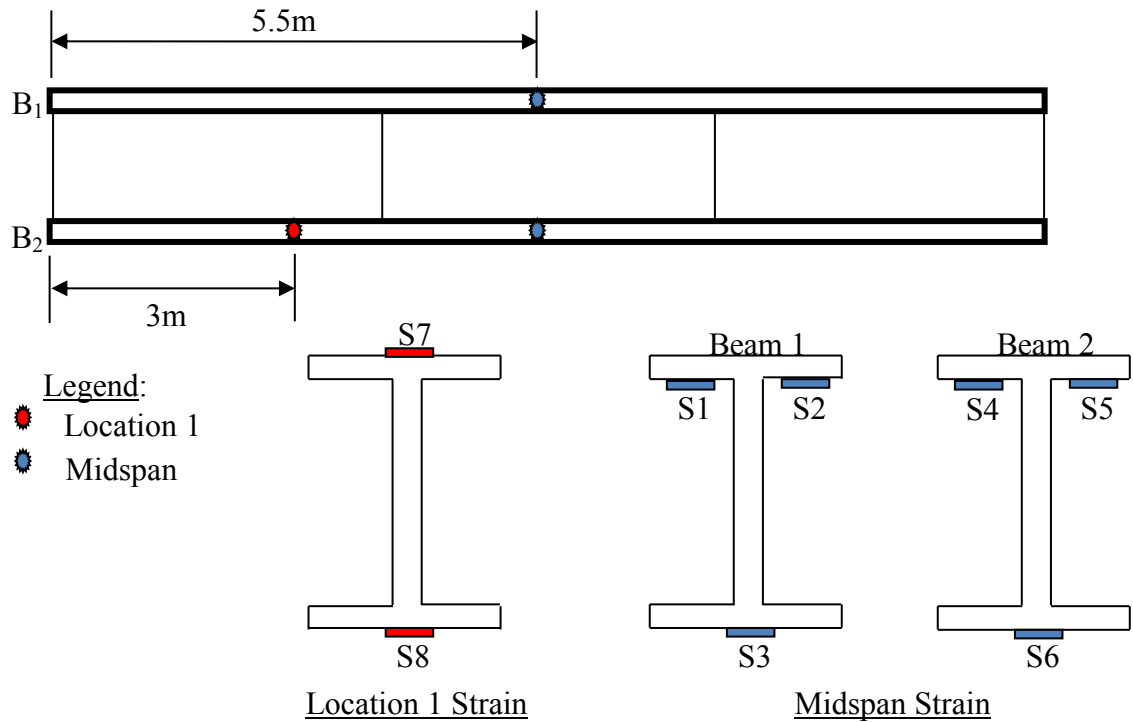


Figure 4.18 Location of longitudinal strain gages along specimen.

Figure 4.19 shows the neutral axis plot for specimen C1-2 obtained at location 1 using strain readings S7 and S8. The experimental neutral axis was measured at 175.2 mm from the bottom flange. This was in compliance with the theoretical neutral axis elevation of 174.5 mm calculated using the section properties of the beam.

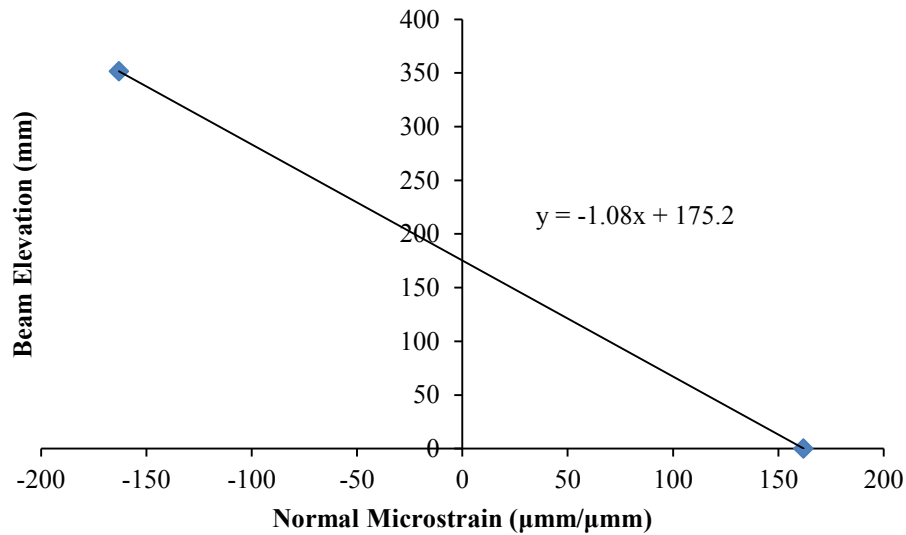


Figure 4.19 Specimen C1-2 experimental neutral axis plot at location 1.

For midspan location, the normal strains from the flanges of both beams were plotted for all three specimens in Figure 4.20 to 4.22. Since gages were mounted on either side of the beam web, the average of these strain readings was used in plotting the midspan neutral axis. The figures show that the neutral axis locations for specimens C1-2 and C-2 are similar. However, the neutral axis for the two specimens was determined to be approximately 22 mm ($196-174 = 22$ mm) higher than that determined for location 1. This discrepancy is believed to be attributed to the plate (part of the pivot assembly) welded on the top flange of the two beams at midspan as shown in Figure 4.23. The weld may have engaged a portion of the plate resulting in an increase in the elevation of the experimental neutral axis. The engaged portion of the pivot assembly base was roughly 13 mm high by 50 mm wide. The average neutral axis location for two beams in specimen C1-1 (Figure 4.20) was about 192 mm which was similar to the other two specimens but the strain readings for two beams had more pronounced variation. This variation was believed to attribute to the failure mode of specimen C1-1 where one beam (beam 2) buckled inelastically and the other beam (beam 1) buckled elastically. The normal strain distribution of beam 2 was affected by warping of the flange causing the strains to be magnified at the S4 gage location when buckling had occurred.

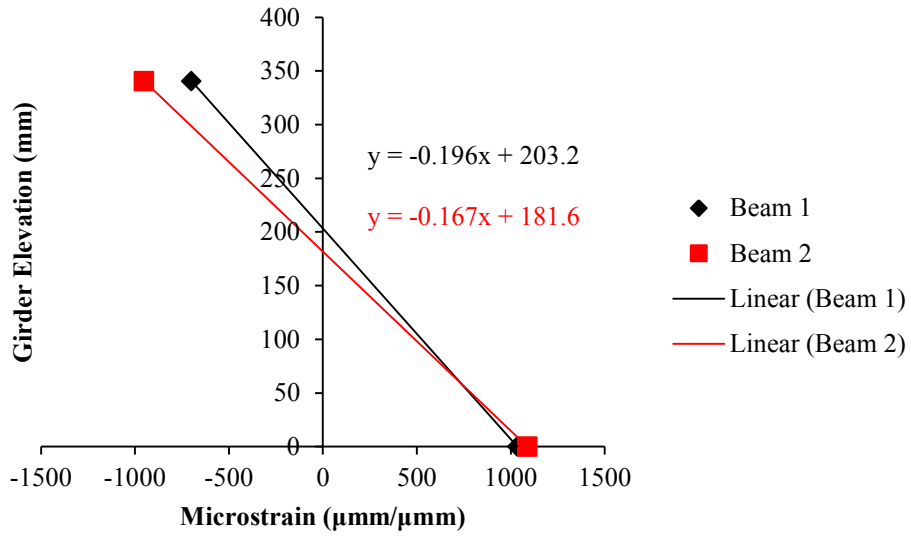


Figure 4.20 Specimen C1-1 midspan experimental neutral axis plot.

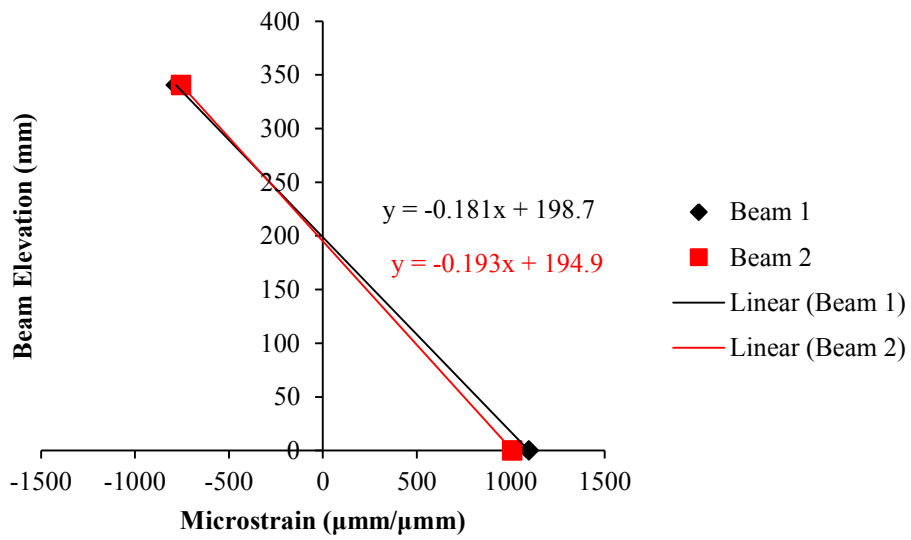


Figure 4.21 Specimen C1-2 midspan experimental neutral axis plot.

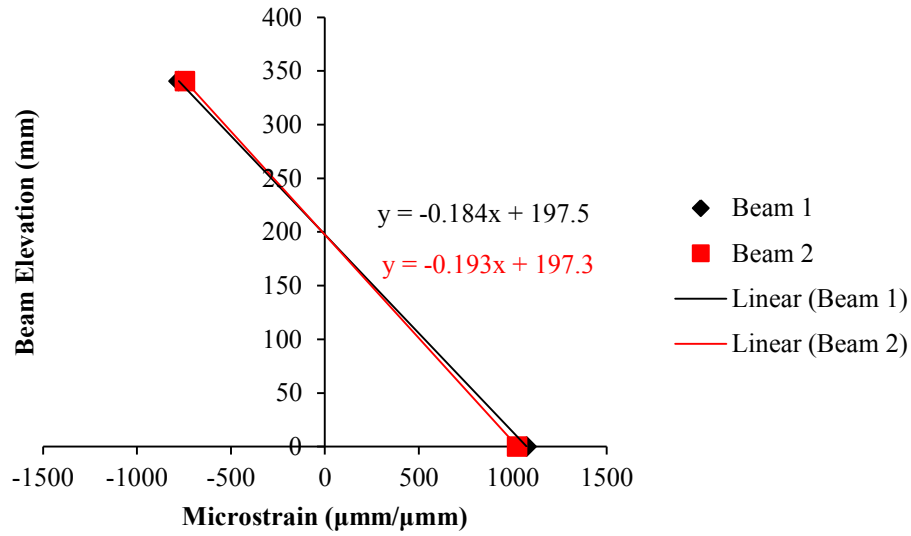


Figure 4.22 Specimen C2 midspan neutral axis plot.

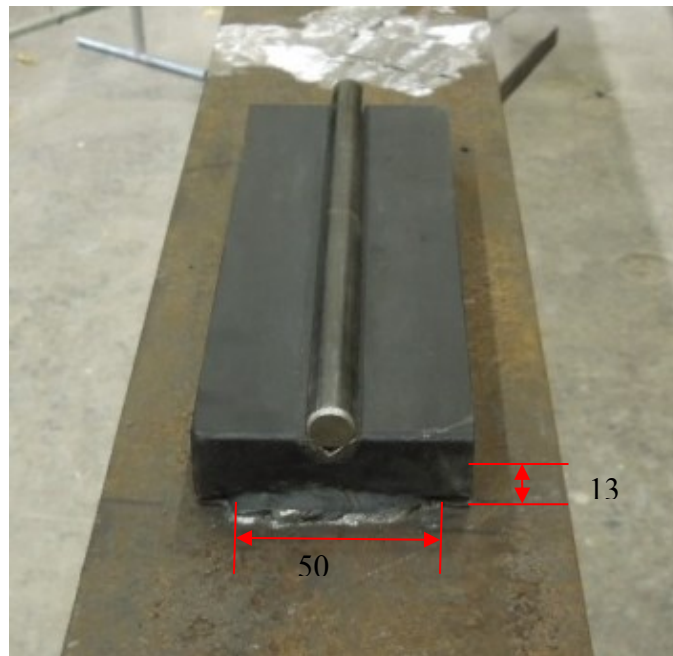


Figure 4.23 Engaged portion of pivot assembly base.

The stresses calculated using experimental load and section modulus are compared with experimental normal stresses obtained from strain readings and the comparison is presented in Table 4.4. Each beam had to be analyzed individually due to varying elevations of the beams' neutral axis resulting in each beam having slight variance in their section properties. The theoretical yield stress was also presented in the table. These

stresses were determined incorporating the residual stress from Section 4.2. It is noted that the stresses for specimen C2 were calculated at load of 119 kN when yielding had occurred whereas the stresses for specimens C1-1 and C1-2 were calculated at the buckling load. A comparison between the experimental stresses and theoretical yield stress shows that specimen C1-2 remained elastic while specimens C1-1 and C2 developed yielding in beam 2. This is consistent with the experimental observation.

Table 4.4 Comparison of experimental and calculated flexural stress.

Test Specimen	Experimental Normal Stress (MPa)		Calculated Normal Stress (MPa)		Theoretical Yield Stress (MPa)
	Beam 1	Beam 2	Beam 1	Beam 2	Beam 1 and 2
	$\sigma_{\text{top}} / \sigma_{\text{bottom}}$				
C1-1	-208 / 294	-283 / 308	-188 / 267	-259 / 281	-270 / 342
C1-2	-171 / 226	-181 / 227	-147 / 195	-151 / 195	
C2	-289 / 328	-310 / 385	-211 / 281	-228 / 302	

The results of Table 4.4 indicate the stresses calculated using the experimental strain values were 10 – 20% greater than the stresses calculated using the applied load for all specimens. This error was suspected to be from two sources: one of which was from strain gauge transverse sensitivity and the other was a result of cross-section warping and twisting at lateral buckling. A publication by the strain gage manufacturer, Vishay Precision Group, states that the error due to transverse sensitivity ranges between 0.9 - 2.0% of the axial strain reading (Vishay Precision Group, 2011). The warping of the cross-section will result in additional axial strains either added or subtracted from the flange strain of the test specimen and these strains were not included in the calculated stresses. Elsayed (2000) observed that I-girders without web stiffeners displayed web distortion which resulted in an increase of the compression flange stresses. These observations indicate that cross-section warping may have resulted in the experimental flange stresses to be magnified in Table 4.4 since no web stiffeners were provided beneath the midspan loading arrangement.

4.6 COMPARISON TO ANALYTICAL RESULTS

In this section, the experimental results are compared to the analytical values obtained using methods presented in Chapter 2. The experimental results of Specimen C1-1 were not included in the comparison since the analytical methods do not account for the lateral restraint developed at the midspan loading points.

The experimental critical moment was calculated using Equation [4.2] which takes into account the moment developed from specimen self-weight that had been previously neglected in the load vs. displacement responses.

$$M_{CRexp} = \frac{P_{CRexp}L}{4} + \frac{w_{exp}L^2}{8} \quad [4.2]$$

where,

P_{CRexp} is the experimental critical buckling load of the specimen (kN),

w_{exp} is the uniformly distributed selfweight of the specimen (kN/m).

4.6.1 Specimen C1 Comparison

The results comparison of Specimen C1-2 where beams are braced using only torsional bracing is presented in Table 4.5. The analytical solutions for the buckling moment were calculated from research by Taylor and Ojalvo (1966), Phillips (1990), Yura (2001), and Yura *et al.* (2008). The provided torsional cross-frame system stiffness of a single cross-frame and the continuous torsional cross-frame stiffness were calculated in accordance with Equation [2.1] and Equation [2.15] respectively. Since the intermediate web stiffeners at the torsional brace locations were welded to the beam flanges, the stiffness reduction due to cross-sectional distortion was neglected in Equation [2.1]. All critical moment calculations are presented in Appendix B.

Table 4.5 Specimen C1 M_{cr} results comparison.

Specimen	Experimental	Taylor and Ojalvo (1966), Eqn. [2.14]	Phillips (1990), Eqn. [2.16]	Yura (2001), Eqn. [2.17]	Yura <i>et al.</i> (2008), Eqn. [2.23]
C1-2	209 kN·m	212 kN·m	200 kN·m	229 kN·m	292 kN·m

The calculated critical moment using a continuous torsional brace stiffness presented by Taylor and Ojalvo (1966) overestimated the experimental moment by 1.4%. This solution appeared to be quite accurate but the analytical value does not account for the effects of moment gradient. If a moment gradient factor calculated using Equation [2.16] was applied to this solution based on the length of the unbraced segment, the critical moment would be overestimated by 10%.

The numerical solution presented in Equation [2.16] by Phillips (1990) underestimates the experimental moment by 4.5%. This solution does not account for the effects of moment gradient or loading height, but considers the reduction in torsional brace stiffness caused by initial imperfections shown in Equation [2.5].

Yura (2001) modified the solution for the critical moment from previous work by Phillips (1990) to account for load height and moment gradient. The analytical value approximated the experimental critical moment to within 10%. This method is simple to use yet provides an approximate solution that is quite accurate and accounts for various loading scenarios. A loading height factor $C_t = 1.0$ was used in the analysis since Yura suggested that loading height effect was negligible for twin girder systems with only torsional braces. A moment gradient factor was calculated using Equation [2.13].

The calculated critical moment using the closed form solution presented by Yura *et al.* (2008) overestimated the experimental moment by 40%. Yura *et al.* (2008) applied a moment gradient factor of 1.35 for a beam subjected to a midspan point load based on recommendations provided in Galambos (1998). Yura *et al.* also indicates the top flange loading effects are negligible for twin girder systems and that a 30% reduction in critical

moment should be applied for twin girders braced with only two intermediate torsional cross-frames (2008).

4.6.2 Specimen C2 Critical Moment Comparison

The comparison of results of Specimen C2 where beams are braced using a combination of lateral and torsional bracing is presented in Table 4.6. The analytical value was calculated using Equation [2.18] (Phillips, 1990). The torsional brace stiffness was calculated using the same methodology as for Specimen C1. The stiffness of the top flange bracing was calculated using Equation [2.21]. The angular component of the calculated member stiffness was required to determine the lateral stiffness provided to the top flange at the brace point. An initial imperfection of 9 mm was used to calculate the reduction factor for imperfections c_L . Equation [2.18] does not consider the effects of moment gradient.

Table 4.6 Specimen C2 M_{cr} results comparison.

Specimen	Experimental	Phillips (1990) Eqn. [2.18]
C2	364 kN·m	364 kN·m

The critical moment value of Equation [2.18] was governed by yielding of the section, M_y . Utilizing the yield stress presented in Table 4.1 a yield moment was calculate to be within 1% of the experimental moment. The critical moment resistance with combination of lateral and torsional bracing significantly increases the critical moment. In comparison to Specimen C1-2, the addition of lateral bracing to force yielding of the test specimen (Specimen C2) results in an increase of critical moment by a factor of 1.73.

4.7 COMPARISON TO DESIGN STANDARDS

Table 4.7 compares the experimental critical moment for a single beam of specimen C1-2 with the analytical critical moment using CSA S6 (2006). The moment magnifier developed by Wong and Driver (2010) was adopted to account for effects of moment gradient and the loading height effect was considered by implementing an ω_2 value of 1.0

with an effective length of $1.2L_u$, where L_u is the distance between intermediate cross-frames. Sample critical moment calculations based on CSA S6 (2006) are included in Appendix C.

A 33% reduction in the experimental critical moment was observed when top flange loading effect was considered. As discussed in Chapter 2, Yura *et al.* (2008) indicated that top flange loading was negligible for twin girder specimens. When top flange loading was neglected in the CSA S6 (2006) calculation, the calculated critical moment was within 3% of the experimental critical moment. If top flange loading is considered in design as per CSA S6 (2006) then an effective unbraced length of beam (distance between intermediate cross-frames) of 2864 mm is required to achieve a moment equivalent to the critical moment of specimen C1-2 provided in Table 4.7.

Table 4.7 Specimen C1-2 M_{cr} Comparison to CSA S6 (2006) (per beam).

	Experimental	Top Flange Loading	No Top Flange Loading
M_{cr} (kN·m)	104.5 kN·m	69.8 kN·m	101.8 kN·m

This suggests that top flange loading does not have a significant effect on the critical moment of twin girder specimens. This observation has also been suggested by Helwig *et al.* (1993), Yura (2001), Yura *et al.* (2008) as described in Chapter 2.

Specimen C2 critical moment is compared to the critical moment calculated in accordance with CSA S6 (2006) in Table 4.8. Values in the second and third columns of the table are the calculated critical moments using Equation [2.24] for the unsupported length of beam between cross-frames (3.667 m) and the unbraced length of beam measured between in plan brace points (1.838 m) respectively. In the former case, the CSA S6 (2006) equation markedly underestimated the experimental critical moment regardless whether the top flange loading effect was considered. In the latter case, the CSA S6 (2006) critical moment with top flange loading only underestimated the experimental results by a factor of 1.02 resulting in a calculated critical moment of 178.8

kN·m per beam. When top flange loading was neglected, CSA S6 (2006) overestimated the experimental results by a factor of 1.10.

Table 4.8 Specimen C2 M_{cr} comparison to CSA S6 (2006) (per beam).

Specimen C2	M_{cr} (kN·m) – L_u between cross-frames	M_{cr} (kN·m) – L_u between lateral braces
Experimental	182.0	
Top Flange Loading	69.8	178.8
No Top Flange Loading	101.8	200.0

For beams braced using a combination of lateral and torsional bracing, the CSA S6 (2006) equation is accurate when the distance between lateral brace points is considered as the unbraced length and top flange loading effect is considered. It suggests that the loading position effect should be included in the critical moment calculation when the lateral braces are present. Research conducted by Yura (2001) also indicated that unlike the torsionally braced beams, loading height has a significant effect on the critical moment of laterally braced beams.

CHAPTER 5 FINITE ELEMENT ANALYSIS

5.1 GENERAL

A finite element study was conducted to supplement the experimental results while providing an alternate method to investigate additional parameters that may influence the lateral stability of the twin girder specimen.

The modeling was conducted using Lusas Bridge Plus 14.7 finite element software[®], which is developed for the analysis, design, and assessment of all types of bridge structures (Lusas, 2013). This software provided the capability of incorporating geometric and material nonlinearity in the buckling analysis.

5.2 FINITE ELEMENT ANALYSIS

5.2.1 Description of Elements

The finite element model was developed using QTS4 and BTS3 elements available in Lusas. The beam flanges, web and stiffener plates were all modeled using the QTS4 element which is a 3D, 4-node quadrilateral thick shell element. This element is suitable for analyzing thick shell geometries that are susceptible to material and geometric non-linearity such as large displacements, rotations, and strains. The lateral and torsional bracing members between beams were modeled using BTS3 elements which are 3D, 2-node thick beam elements. These elements are also capable of accounting for geometric and material non-linearities. A summary of the degrees of freedom for each element used in the finite element model is presented in Table 5.1.

Table 5.1 Element summary.

Element Name	Number of Nodes	Degrees of Freedom
QTS4	4	$u_x, u_y, u_z, \theta_x, \theta_y, \theta_z$
BTS3	2	$u_x, u_y, u_z, \theta_x, \theta_y, \theta_z$

5.2.2 Material Non-Linearity and Stress-Strain Relationship

Two types of material models were used to represent the behaviour of steel. The first material model used to define the material behaviour in the parametric study was an elastic perfectly plastic model shown in Figure 5.1. The standard material properties were used for steel where an elastic modulus E , of 200,000 MPa and a yield stress F_y , of 350 MPa were assumed. The second material model shown in Figure 5.2 was implemented to validate the results of the experimental program by implementing a multi-linear material model developed from coupon testing. A detailed description of the material model can be found in Appendix D.

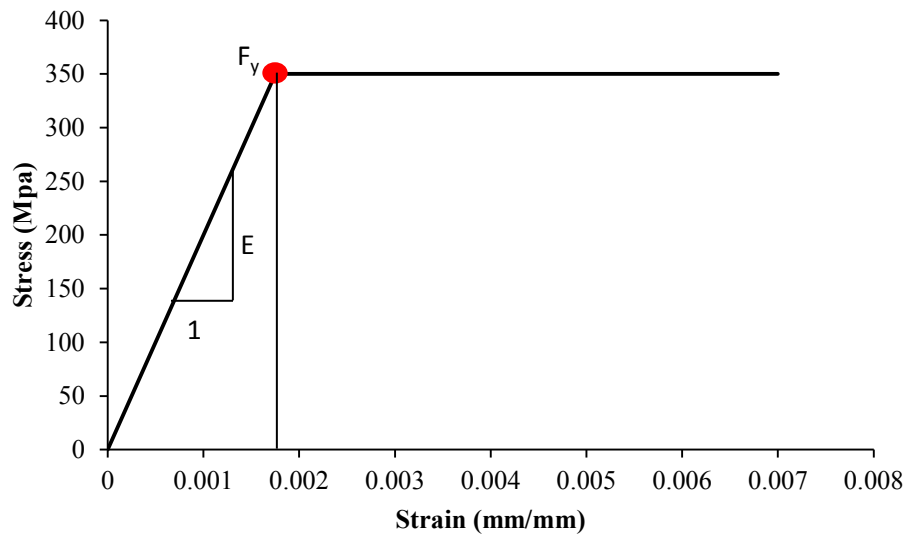


Figure 5.1 Elasto-plastic material model.

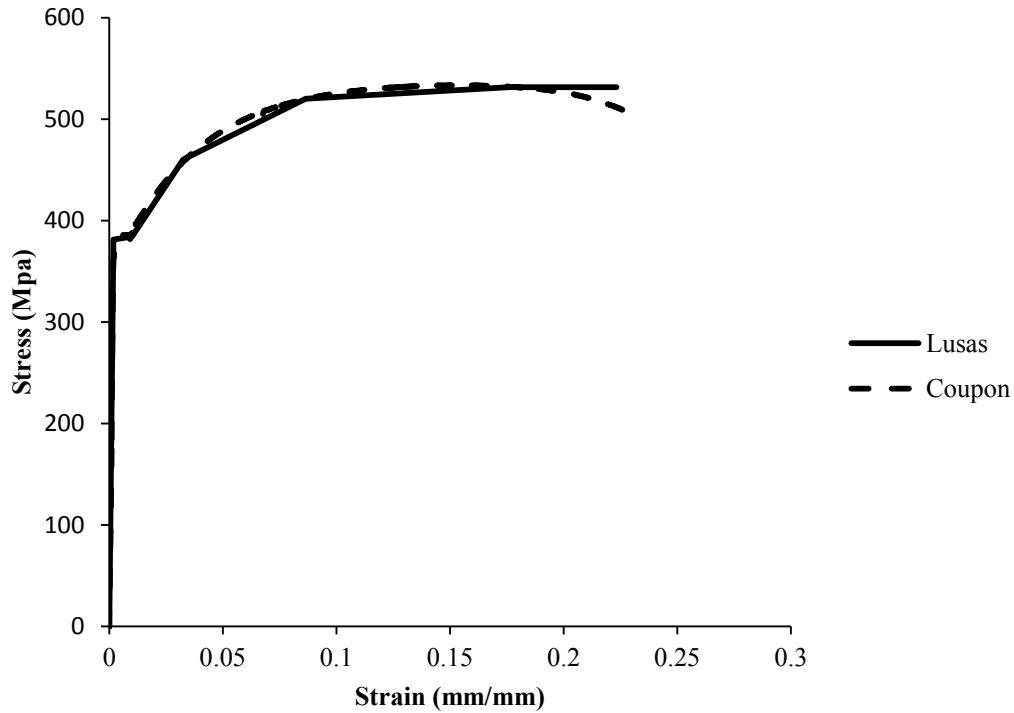


Figure 5.2 Test specimen material model applied to finite element.

5.2.3 Finite Element Mesh

The specimen was meshed using thick shell elements for the girder flanges, webs, and stiffeners whereas all bracing members between girders were meshed using thick non-linear beam elements. All shell elements were meshed in the middle plane of each component. The nodes at the flange to web junctions and stiffener to web/flange junctions were made coincidental to allow the nodes to be easily merged. To simplify the model, the fillet developed from the hot rolling process at the web to flange junction was ignored while the distance between the bottom and top flange centroids of the girder was maintained. This resulted in a small area of overlap from the web element being extended half the thickness of flange at the web to flange junction as shown in Figure 5.3. The overlap at the web to flange junction is negligible in comparison to the remaining area of the girder and was thus ignored in the analysis.

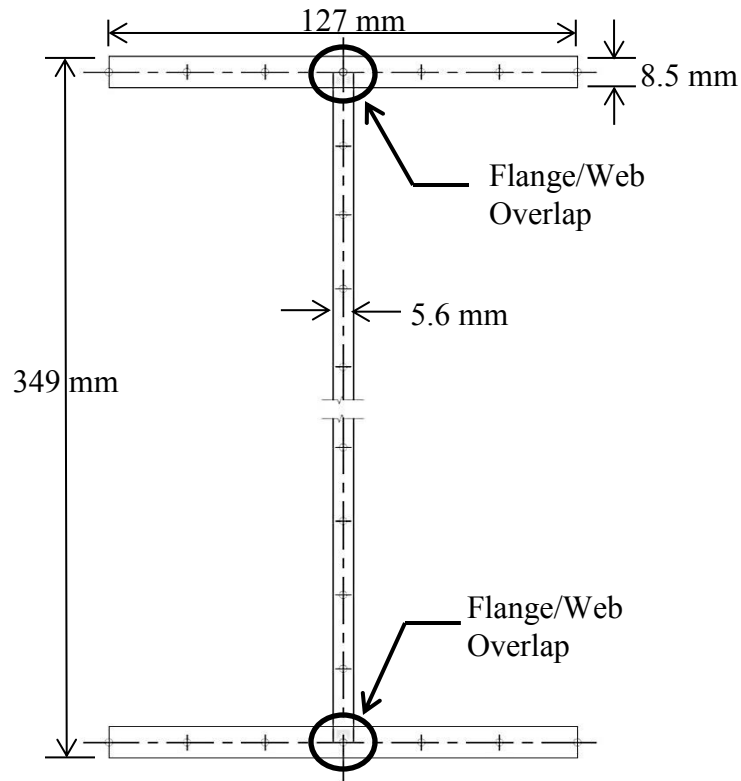


Figure 5.3 Cross-section of finite element mesh.

A convergence study was conducted to determine an efficient mesh density for the finite element model. Four different element sizes with edge lengths of 60 mm, 30 mm, 20 mm and 15 mm were analyzed using a non-linear buckling analysis. The results of the convergence study shown in Table 5.2 indicated that a mesh with a 20 mm edge length provides sufficient accuracy and computational efficiency.

Table 5.2 Mesh convergence study results.

Maximum Edge Length (mm)	P_{cr} (kN)	Difference (%)	Computational Time (hrs)
60	76.24	-	0.15
30	74.16	1.028	0.37
20	71.92	1.060	1.10
15	71.92	1.060	8.00

The flanges of the W360x33 section were meshed using six elements across the flange width. Each element was 21 mm x 20 mm with a corresponding thickness of 8.5 mm.

The webs had a similar element size that had dimensions of 20 mm x 20 mm with a corresponding thickness of 5.6 mm. The lateral bracing members that compose the cross-frame system shown in Figure 5.4 were meshed with member lengths of roughly 115 mm resulting in the member being subdivided into 6 divisions between flange tips. As shown in Figure 5.4, the cross-frame members were connected to both girders at the web to flange junctions.

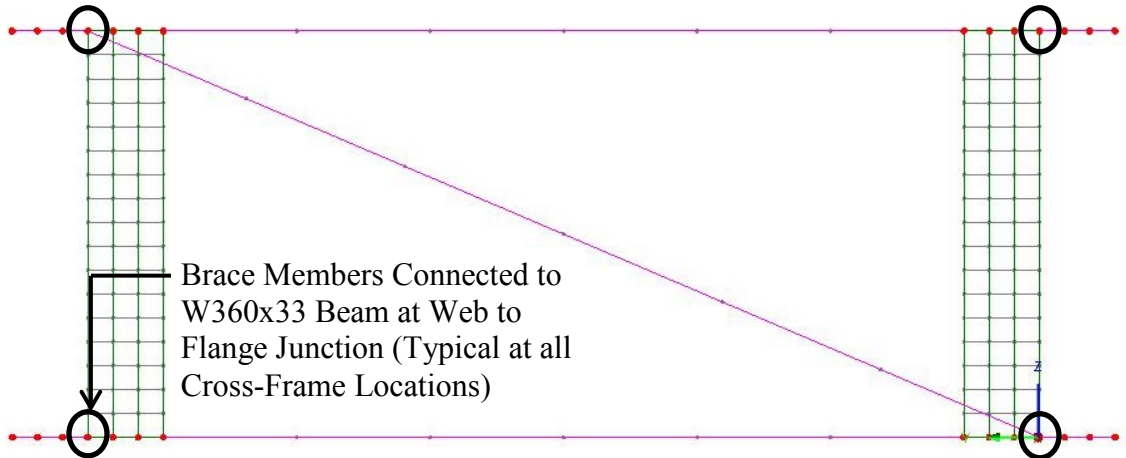


Figure 5.4 Typical cross-frame mesh.

5.2.4 Initial Imperfections

The initial out-of-straightness of the specimen was incorporated directly into the finite element model geometry. This was achieved by plotting the nodes of the girder cross-section based on the sweep measurements recorded at one meter intervals along the girder length. The coordinates of these nodes were input in the model forming the curved geometry of the specimen. An alternative method to consider the initial out-of-straightness of the specimen is to scale the deformed shape of the eigenvalue buckling analysis. However, it was thought that modeling the out-of-straightness using laboratory measurements would achieve a more accurate solution.

5.2.5 Boundary Conditions

Boundary conditions were applied to the model to simulate a twin-girder system that was simply supported in bending and torsion. Transverse and longitudinal translations were restrained at the end supports based on the support conditions provided in Figure 3.10.

The restraints shown in Figure 5.5 were situated at the web to bottom flange junction at all end supports.

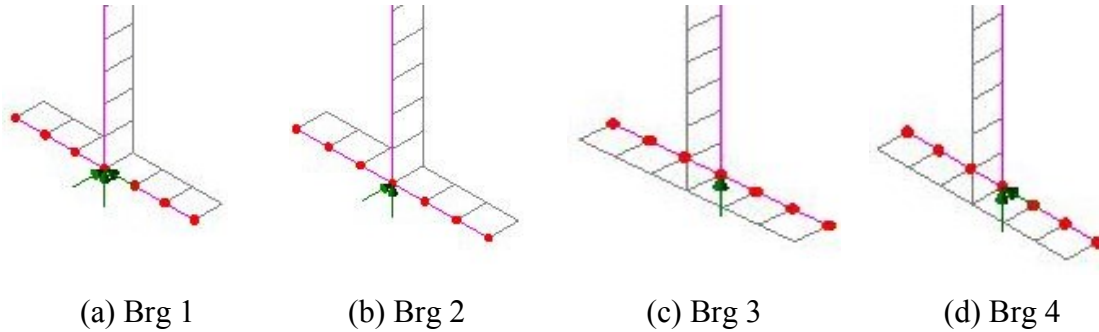


Figure 5.5 Finite element model end support conditions.

5.2.6 Residual Stresses

The residual stress profile shown in Figure 4.2 was implemented into the finite element analysis. The triangular distribution was simplified using a series of uniform stresses that were applied to each element through the cross-section as shown in Figure 5.6. The residual stresses were applied to the finite element model using the residual stress loading application provided in Lusas (2013). The residual stress distribution was applied to the model during the first load increment of the non-linear analysis.

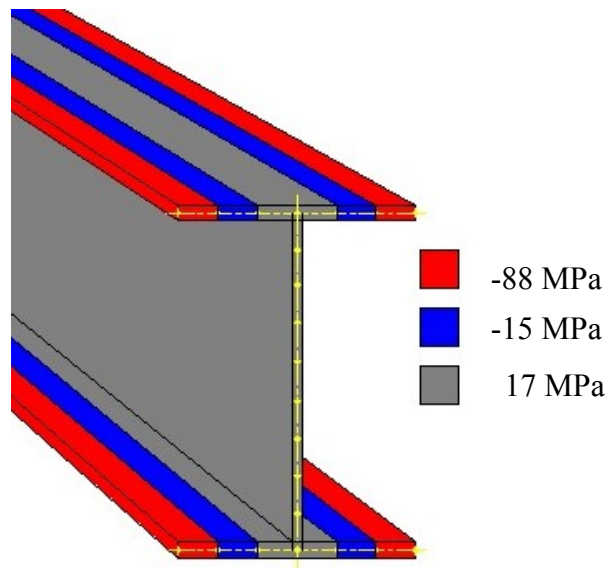


Figure 5.6 Residual stress pattern applied to finite element model.

5.2.7 Load Application

The location of the applied load in the finite element analysis was developed to simulate the loading transferred from the spreader beam to the specimen in the experimental setup. A uniformly distributed load shown in Figure 5.7 was applied at the top flange to web junction at the beam midspan. The length of the uniformly distributed load was equivalent to the length of the pivot assembly used in the experimental program. A uniformly distributed load was applied to the model to prevent potential local buckling failure which may occur if a single point load was applied at an infinitesimal point on the beam midspan.

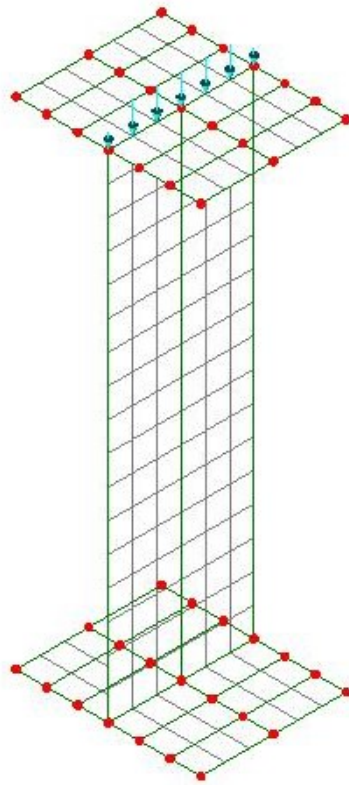


Figure 5.7 Typical midspan load application at top flange to web junction.

5.2.8 Non-Linear Buckling Analysis

The critical buckling load was determined using a non-linear analysis. The midspan load presented in Figure 5.7 was applied to the model in a number of load increments. For

each load increment, iterations are conducted in order for the structure to converge to an equilibrium state with the balanced forces. Lusas uses the Newton-Raphson procedure for this incremental-iterative method (Lusas, 2013).

In the sub step of the first load increment, the residual stresses and the specimen self-weight were applied to the finite element model using an initial input file. The following loading increments were applied up to a limit that exceeded the anticipated buckling load. To ensure that convergence of the load increments was achieved, a value of twenty iterations per increment was selected. The time history utility available in Lusas (2013) provided the ability to plot the applied load versus the structural deformation for each load increment. These time history plots formed the basis of the load versus displacement responses that were utilized to determine the critical buckling load.

5.3 FINITE ELEMENT RESULTS

For each test specimen, the load versus lateral displacement and load versus vertical displacement responses were obtained. The finite element critical buckling load was defined from the load versus lateral displacement diagram in which the specimen displayed a loss of lateral stiffness that was indicated by a sudden increase in lateral displacement while the load remained constant. The buckling modes for each test setup were also determined by plotting the deflected shape of the specimen at the critical buckling load. The numerical results are provided in Table 5.3 along with the experimental results of the three test specimens.

Table 5.3 Summary of finite element and test results for three specimens.

Test Spec.	Finite Element Study					Experimental Study				
	P _{cr} (kN)	Δ _{L,B1} (mm)	Δ _{L,B2} (mm)	Δ _{V,B1} (mm)	Δ _{V,B2} (mm)	P _{cr} (kN)	Δ _{L,B1} (mm)	Δ _{L,B2} (mm)	Δ _{V,B1} (mm)	Δ _{V,B2} (mm)
C1-1	105.0	4.1	3.4	84.0	79.7	99.5	0.3	1.2	79.1	78.2
C1-2	70.0	11.5	9.5	69.8	58.0	72.2	8.6	2.0	62.2	56.8
C2	142.6	1.5	26.1	126.4	110.0	145.3	1.6	1.8	133.0	127.9

Specimen C1-1 was modelled with the assumption that the friction developed in the roller assembly provided lateral restraint to the top flange of each girder. To verify this assumption, lateral springs situated at the roller location on the top flange of each beam were implemented in the specimen C1-1 model to simulate the effect of this friction. A small experimental procedure shown in Figure 5.8 was developed to determine the spring stiffness required in the finite element model. The experiment consisted of a small column that was loaded axially under a constant load with roller assemblies mounted at either end of the column. The constant axial load was applied at a level equivalent to the buckling load of the C1-1 specimen while a lateral load was exerted at the column mid height. The lateral movement of the roller assembly was monitored using LVDTs while the applied lateral load was recorded using a 200 kN load cell. A plot of the lateral load versus lateral displacement curve is shown in Figure 5.9. A spring constant of 128 N/mm was determined by calculating the slope of a linear segment of data around a displacement of 0.4 mm. The initial displacement readings (< 0.4 mm) from Figure 5.9 were ignored for the calculation of the spring stiffness since minimal movement was recorded over a large increase in lateral load. This indicated the column and rollers in the experiment were still stationary. The final displacement readings from Figure 5.9 were also omitted from the spring stiffness calculation due to the increase in lateral displacement over a constant load. This indicated the rollers were in motion and the lateral load had overcome the frictional resistance of the assembly. The springs were applied at the top flange to web junction for each beam.



Figure 5.8 Specimen C1-1 roller friction experiment.

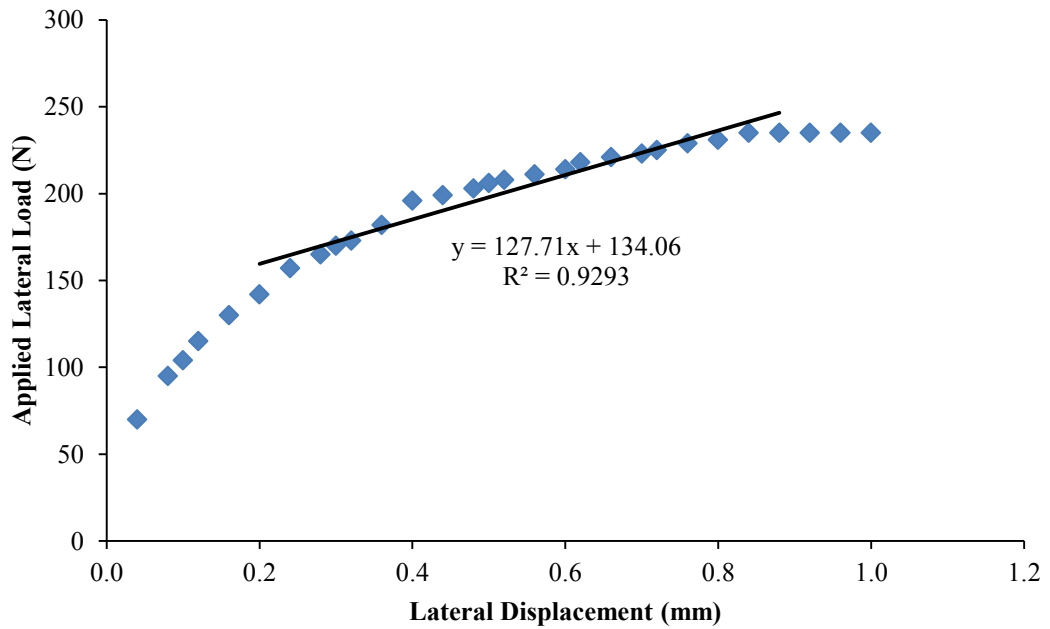


Figure 5.9 Lateral load vs. lateral displacement of specimen C1-1 roller assembly.

Figure 5.10 compares the lateral displacement profile obtained from the finite element model and the experiment for C1-1 specimen. The figure shows that FE results are in

good correlation with the test results. This also confirms that the restraint existed at the compression flanges from the roller assemblies during the experimental testing and 130 N/mm is a reasonable estimate of this restraint.

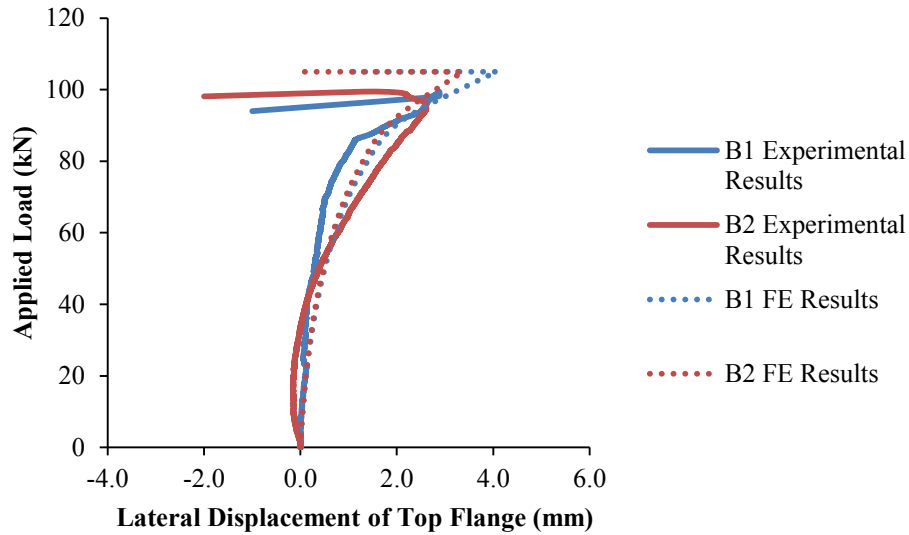


Figure 5.10 Finite element load vs. midspan lateral deflection response for specimen C1-1.

The buckling mode of the finite element model is shown in Figure 5.11 where a pronounced sinusoidal mode referred to as beam buckling occurred in the midspan region and much shallower sinusoidal shapes in the opposite direction on the two side spans. This buckled shape is in reasonably good agreement with the experimental buckling mode shape shown in Figure 4.9a.

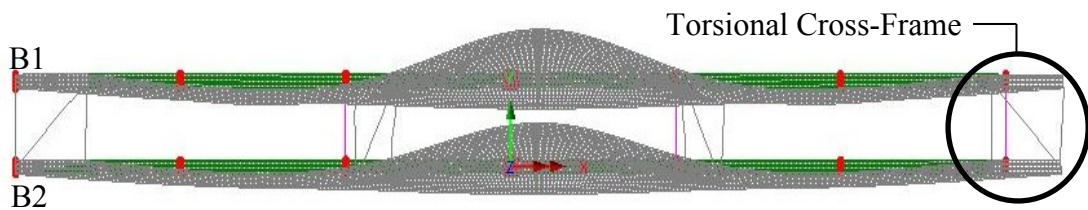


Figure 5.11 Specimen C1-1 sinusoidal buckling mode shape between cross-braces.

Specimen C1-2 was modelled with the assumption that the lateral restraint of the roller system was diminished greatly by changing the roller assembly to a set of Hilman rollers

and by providing smoother rolling surfaces. Therefore Specimen C1-2 was initially modelled with no lateral springs present at the roller locations. The lateral displacement at the buckling load shown in Figure 5.13 appeared to be quite significant in comparison to the experimental results. This indicates that some friction still exists in the Hilman roller assembly. A similar spring stiffness test procedure previously conducted for specimen C1-1 to determine the lateral spring stiffness to be applied in the finite element model was conducted for specimen C1-2. The data presented in Figure 5.12 provides a spring stiffness of 43 N/mm. This value was calculated using the same methodology previously described for the spring stiffness of specimen C1-1.

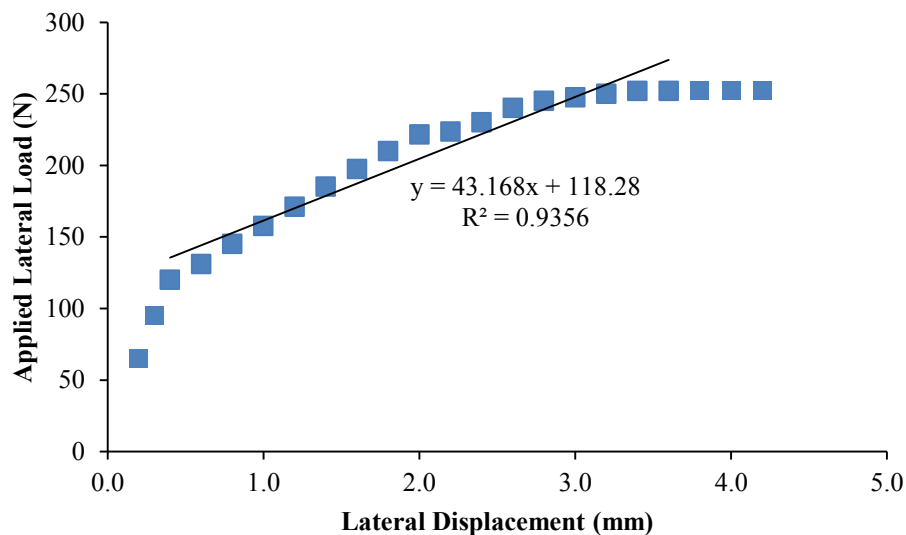


Figure 5.12 Lateral load vs. lateral displacement of specimen C1-2 roller assembly.

The application of a 43 N/mm lateral spring resulted in a lateral deflection response shown in Figure 5.13 that was similar to the Specimen C1-2 experimental response. This suggests the roller assembly continued to induce friction on the experimental behaviour of specimen C1-2, but the friction was not as excessive as the friction induced in Specimen C1-1. Global buckling of the finite element specimen was evident by observing the buckling mode shape shown in Figure 5.14, this mode shape is the same as the buckling mode observed in the experimental test.

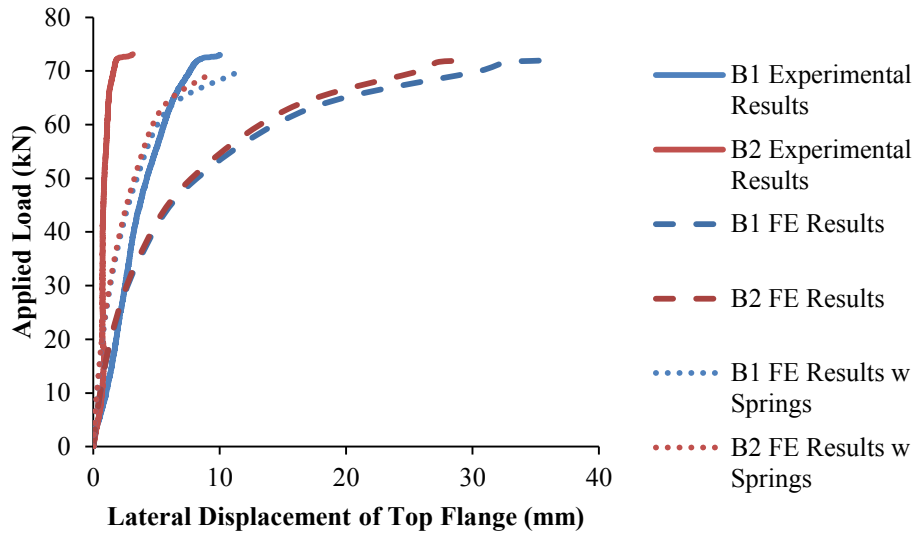


Figure 5.13 Finite element load vs. midspan lateral deflection response for specimen C1-2.

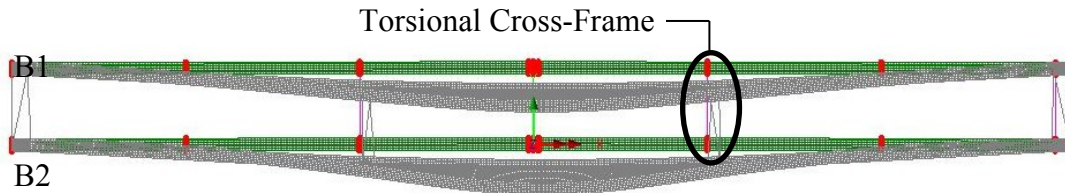


Figure 5.14 Specimen C1-2 global buckling mode shape.

In the case of specimen C2, the model was implemented using top flange lateral springs with a corresponding stiffness of 240 kN/m applied at the loading point of both beams. The spring stiffness of specimen C2 displayed in Figure 5.15 was determined using the same method as specimen C1.

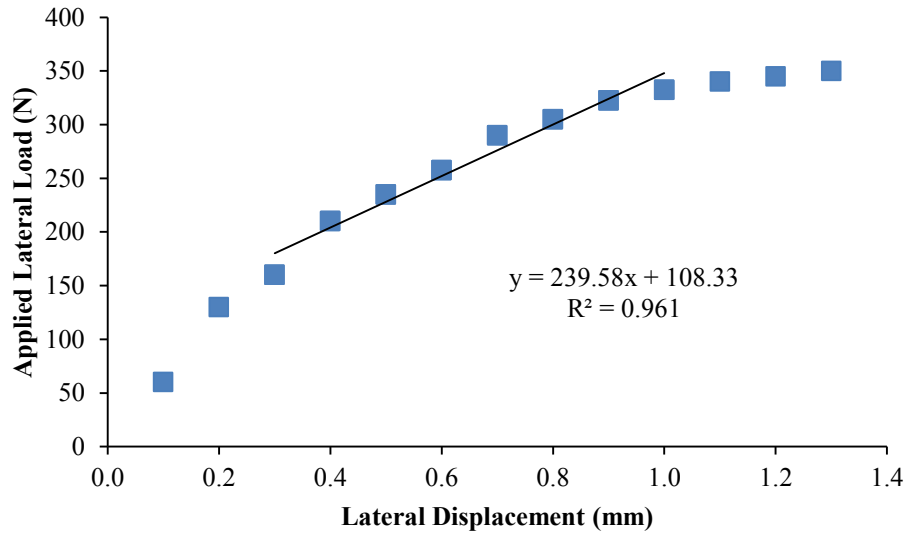


Figure 5.15 Lateral load vs. lateral displacement of specimen C2 roller assembly.

Figure 5.16 shows good agreement for the lateral displacement response of B1 with the experimental data when the lateral springs were modelled to account for the experimental roller friction. The lateral displacement response of B2 showed a difference with the experimental data when the applied load reached higher than 100 kN. The difference was thought to be a result of how the spring stiffness was applied to the compression flange of each beam in the finite element model.

The lateral springs were situated at the midspan of each girder in the finite element model and thus they behaved independently of one another in the model. The rollers in the experimental program shown in Figure 5.17 were connected to a load distribution beam which prevented differential lateral displacement between adjacent rollers. This provided the loading assembly with the ability to provide additional lateral stiffness to the weaker beam (B2) in the system by transferring frictional restraint through the load distribution beam to the roller assembly. In order to develop buckling of the specimen, the global frictional restraint of the system had to be overcome. It is believed that B2 of Specimen C2 in Figure 5.16 was dependent on B1 causing the specimen to behave as a lean-on bracing system.

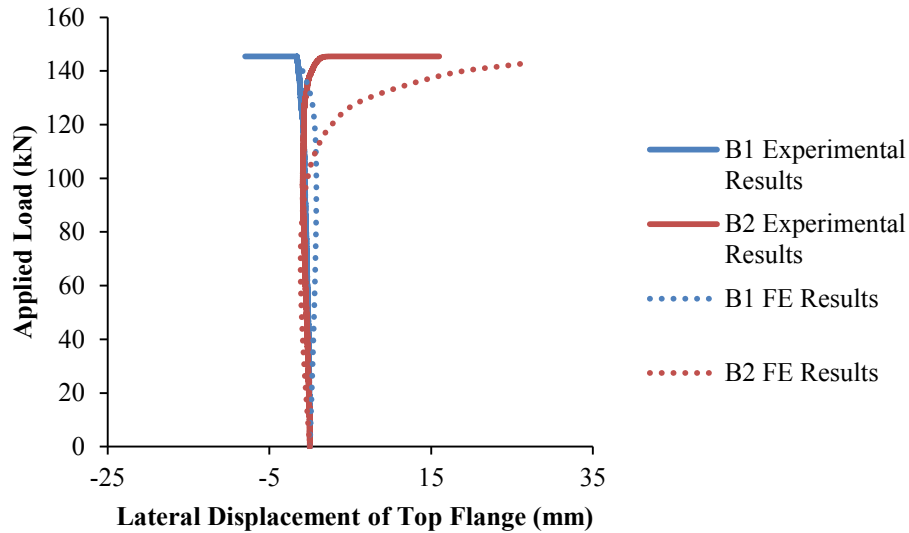


Figure 5.16 Finite element load vs. midspan lateral deflection response for specimen C2 roller assembly.

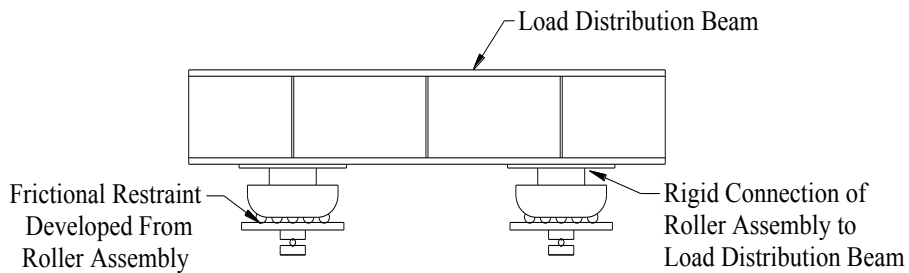


Figure 5.17 Connection of roller assembly to load distribution beam.

The buckled shape of specimen C2 in Figure 5.18 was in good agreement with the experimental results for beam buckling. Beam 1 did not display significant lateral buckling due to the in-plan bracing at the beam midspan preventing relative lateral displacement between brace points. Beam 2 exhibited lateral buckling at the beam midspan since the top flange of this span was not laterally braced.

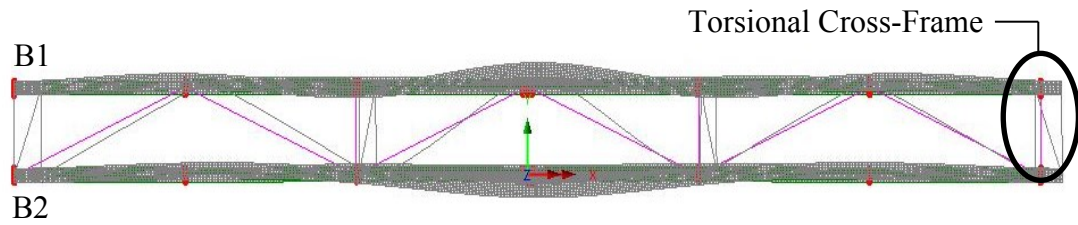


Figure 5.18 Specimen C2 buckled shape between lateral brace points.

Figure 5.19 to Figure 5.21 plot the load versus midspan vertical displacement response for each specimen. The numerical vertical displacement curves are in good agreement with the experimental results for Specimen C1-1. A small discrepancy in the vertical displacement plot was observed for specimen C1-2. As previously discussed in Chapter 4, the variation between experimental vertical displacements for beams 1 and 2 was due to each beam having a different modulus. This trend was still visible when comparing the experimental results to the FE results. Up to a vertical load of 63 kN, the numerical and experimental vertical displacement responses are in good correlation. However, the FE model exhibited a slightly larger vertical displacement for both beams at the ultimate load. Note that Figure 5.13 shows that the FE model had a larger lateral displacement than the experimental results, indicating that the spring stiffness implemented in the model is less than the restraint provided by the roller assembly in the experiment. The lateral displacement would result in bracing forces to be developed in the bracing system. The brace forces developed in the diagonal strut would distribute some magnitude of vertical load from beam 2 to beam 1. The larger the bracing force, the larger this distribution, which in turn results in larger vertical displacement. This may explain the discrepancy between the numerical and experimental vertical displacement at the ultimate. Specimen C2 shown in Figure 5.21 was also in good agreement with the experimental results for the displacement profile. It appears the experimental response showed more nonlinearity towards the ultimate load than the finite element response but the difference between the two was considered to be insignificant since the specimen had already failed by yielding of the material prior to buckling.

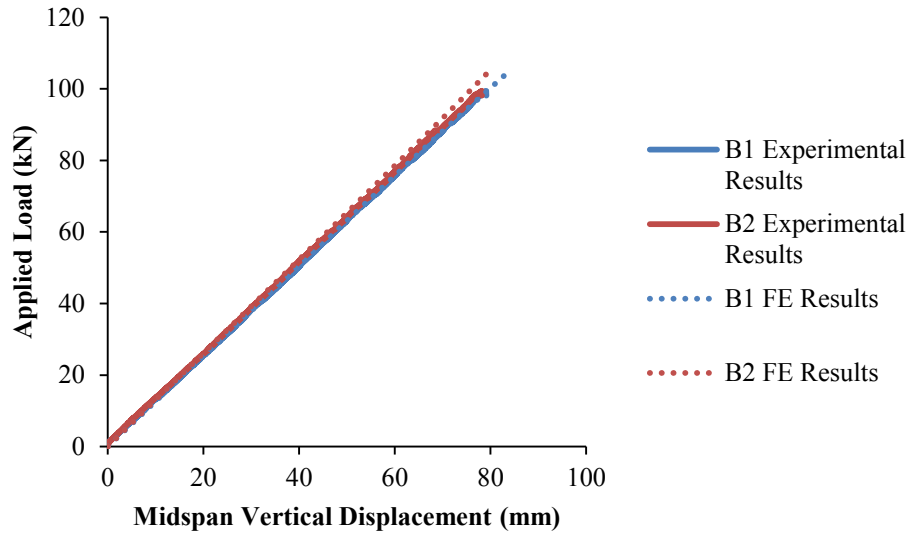


Figure 5.19 Midspan vertical displacement comparison of specimen C1-1.

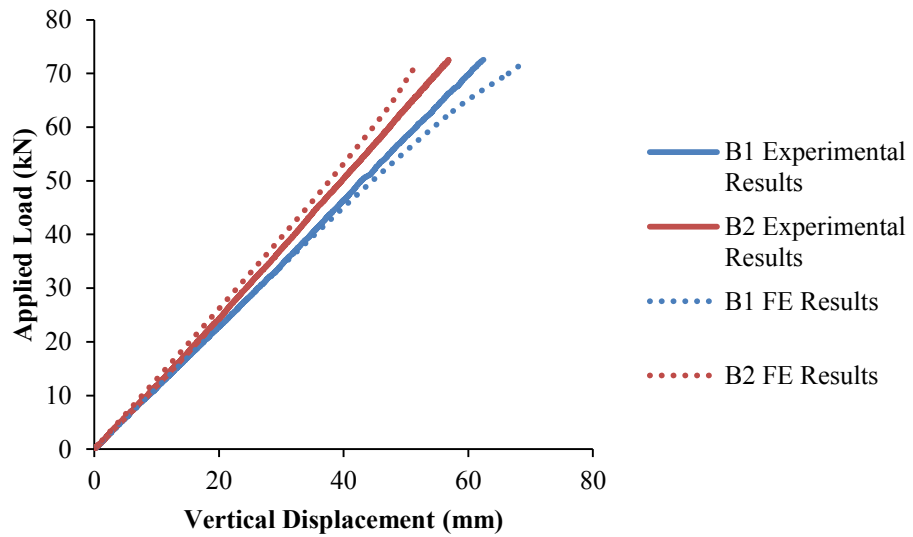


Figure 5.20 Midspan vertical displacement comparison of specimen C1-2.

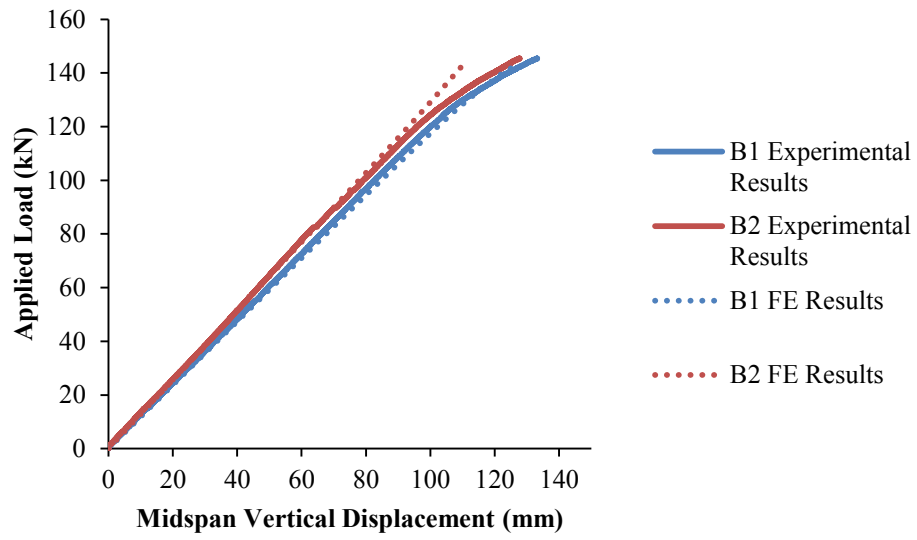


Figure 5.21 Midspan vertical displacement comparison of specimen C2.

CHAPTER 6 PARAMETRIC STUDY

6.1 GENERAL

Parametric studies were conducted to study the effect of additional parameters on the lateral stability of twin-girder systems with torsional bracing beyond the scope of the experimental program. The finite element model developed and validated in Chapter 5 was used in this study. The parameters investigated were girder spacing, cross-frame stiffness, and number of interior cross-frames installed between girders. The finite element model was simplified for the parametric study by removing the initial imperfections and residual stresses. As shown in Figure 5.1, an elastic perfectly plastic material model was used for steel with a yield strength $F_y = 350$ MPa and an elastic modulus $E = 200\,000$ MPa. The reference model is a twin-girder system consisting of two W360×33 beams simply supported with a span of 11 m. The W360x33 section is a Class 1 section. Unless otherwise specified, three interior cross-frames are incorporated and they are equally spaced along the beam span. The configuration of the cross-frame used in Chapter 4 is maintained in the parametric study. Concentrated loads were applied to the top flange of each beam at midspan.

6.2 GIRDER SPACING

In this section, the effect of girder spacing ranging from 0.5 to 1.0 m is studied. These spacing values correspond to girder spacing of 2.15 to 4.3 m for the large scale specimen as described in Chapter 3 if a constant girder spacing to girder depth ratio is maintained. This girder spacing range covers the majority of cases that would be encountered in practice. The critical elastic moment solution for a twin-girder system presented by Yura *et al.* (2008) as in Equation [2.23] is also calculated for comparison. The finite element critical moments are compared in Table 6.1 with moment values calculated using Equation [2.23]. It is noted that the critical moment resistance in the equation was developed for twin girder systems that failed in global buckling in elastic range. This resistance is dependent on the girder spacing, S , but independent of the torsional cross-frame stiffness. However, using a torsional brace stiffness equal to twice the ideal

stiffness is suggested to prevent twisting of the system as well as controlling the forces generated in the braces. The FE critical moment was obtained from the load versus top flange lateral displacement response of a girder. A typical response curve is shown in Figure 6.1. The critical buckling load is deemed to have occurred where the response curve begins to display non-linearity as represented by the red dot in the figure.

Table 6.1 Critical moment comparison between finite element results and Equation [2.23] with varying girder spacing.

Girder spacing (mm)	FE P_{cr} (kN)	FE M_{cr} (kN·m) $M_{cr} = \left(\frac{P_{cr}L}{4} \div 2 \right)$	Equation [2.23] (kN·m)	% Difference Moment
500	60.0	83.0	89.0	6.7
650	78.0	107.0	114.0	6.1
800	95.0	130.6	139.0	6.0
1000	120.0	165.0	173.0	4.6

Table 6.1 shows that for a given number of interior cross-frames (3 cross-frames), as the girder spacing increases, the critical moment also increases. This increase in moment capacity is believed to be due to an increase in torsional stiffness as a result of the increase in moment arm between girders.

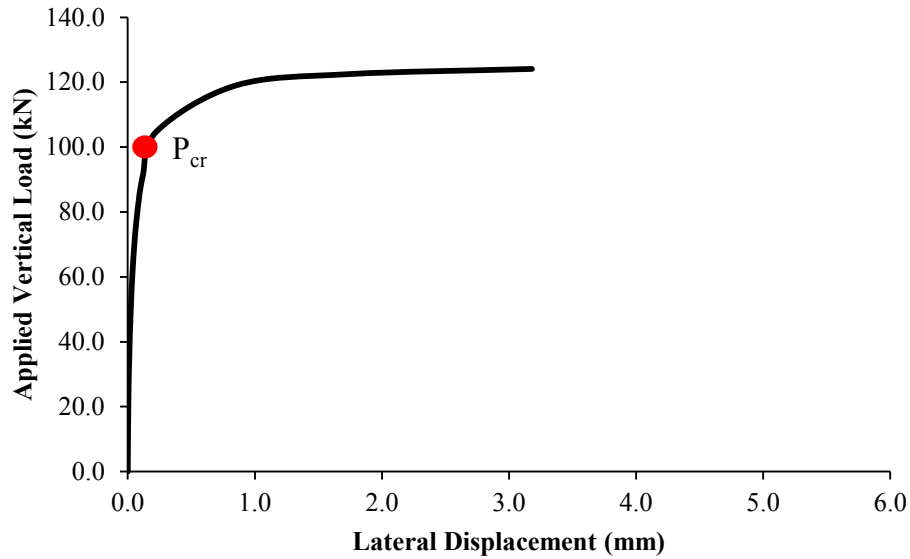


Figure 6.1 Load versus top flange lateral displacement response of a girder.

Figure 6.2 plots the finite element load versus top flange lateral displacement curves for varying girder spacing. It shows that as the girder spacing increases, the critical global buckling load increases. The initial portion of the curves is practically identical with almost zero lateral displacement prior to buckling. The comparison between the FE and the calculated critical moment values (Table 6.1) show that they are in reasonably good agreement with a maximum difference less than 7%. The FE values are in general, lower than the equation values. The listed FE critical moment values are determined as $(P_{cr}L/4)/2$ for one girder where the critical load P_{cr} was determined using the load versus lateral displacement curves in Figure 6.2. A sample calculation using Equation [2.23] is presented in Appendix E.

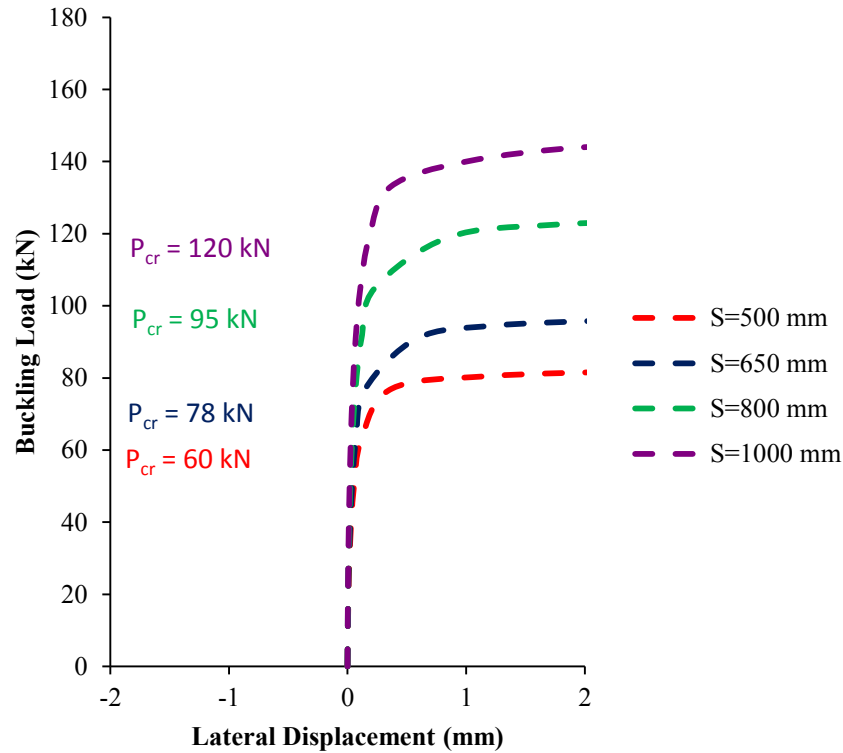


Figure 6.2 Load versus lateral displacement response of 3 interior cross-frame specimen with varying girder spacing.

The effect of varying girder spacing on the critical moment values is illustrated in Figure 6.3. The increase in the critical moment displays a linear relationship with the increase in the girder spacing. Although a limitation on girder spacing was not explicitly specified in Equation [2.23], the maximum moment cannot exceed the yield moment capacity of the cross-section, M_y , which is 165.9 kN·m for W360x33. In addition, the practical slenderness ratio of bracing members will restrict the girder spacing to a realistic range. The maximum permissible slenderness ratios according to CSA S6 (2006) and S16 (2010) for the cross-frame diagonal tension member are 200 and 300 respectively, while the horizontal cross-frame compression members cannot have a slenderness ratio in excess of 160 and 200 respectively.

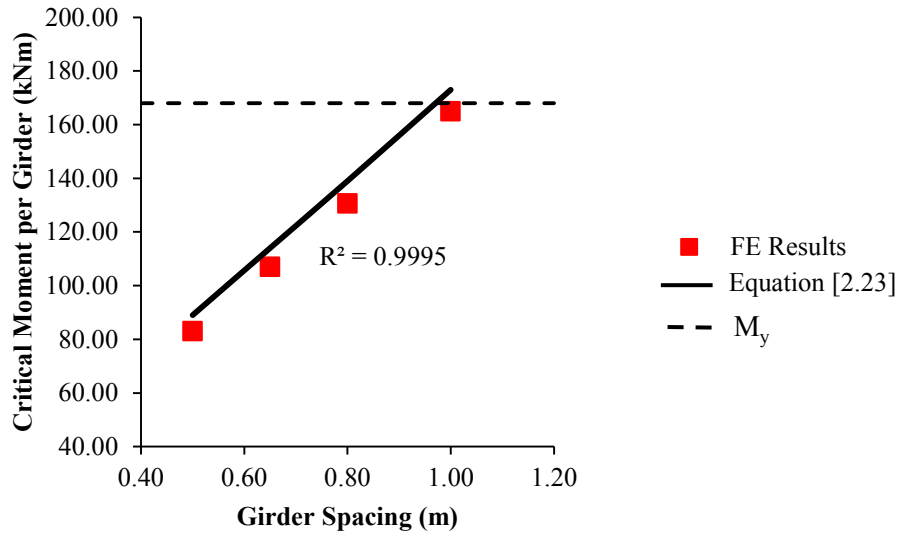


Figure 6.3 Critical moment vs girder spacing for FE and Eqn. [2.23].

6.3 CROSS-FRAME STIFFNESS

As mentioned earlier, twin-girder systems that utilize torsional bracing as the sole method for girder stability require bracing with sufficient stiffness. The numerical stiffness value of the cross-frame system considered in this study was a combination of the brace and the girder stiffness. The effect of cross-sectional distortion of the web was ignored since the stiffener was assumed to be welded to the compression flange therefore web distortion is prevented. In this study, the variation in torsional stiffness was achieved by changing the cross-sectional area of the bracing members while maintaining the girder size. Table 6.2 lists four models with varying cross-frame brace stiffness. All models had a constant girder spacing of 0.8 m with girders braced using three cross-frames. The calculation of the brace stiffness is based on Equation [2.1] and a sample calculation is presented in Appendix E.

Table 6.2 Calculated torsional stiffness for varying cross-frame member sizes.

Member	β_b (N·mm/rad)	β_g (N·mm/rad)	β_t (N·mm/rad)
L19×19×3.2	8.92E+08	9.54E+07	8.62E+07
L38×38×4.8	2.73E+09	9.54E+07	9.22E+07
L102×102×13	1.95E+10	9.54E+07	9.50E+07
C250×30	3.04E+10	9.54E+07	9.51E+07

Table 6.2 displays the brace member stiffness for a single cross-frame (β_b), girder web stiffness (β_g) and the resultant torsional stiffness of an intermediate cross-frame (β_t). A significant increase in the brace member stiffness β_b (34 times) is achieved when the braces are varied from an L19×19×3.2 to a C250×30. However, the system stiffness does not vary in the same magnitude. The much smaller variation of the latter is due to the fact that the system stiffness is governed by the girder web stiffness (Equation [2.1]) and the resultant torsional stiffness is significantly influenced by the bracing component with the smallest stiffness.

Figure 6.4 shows the load versus top flange lateral displacement of the girder for a twin-girder system with varying cross-frame member stiffness and a three cross-frame arrangement. As it can be seen, before the buckling occurred, the variation in the bracing stiffness does not result in any marked variation in the behaviour. The increase in the bracing member stiffness only results in minimal increase in the post buckling capacity. This suggests that, for a given girder size, the use of different cross-sections for bracing members does not significantly affect the critical load for global buckling since the girder stiffness is the dominant component for the cross-frame system stiffness. Also noted is that the system torsional stiffness is not explicitly reflected in Equation [2.23] and thus no comparison between results is presented.

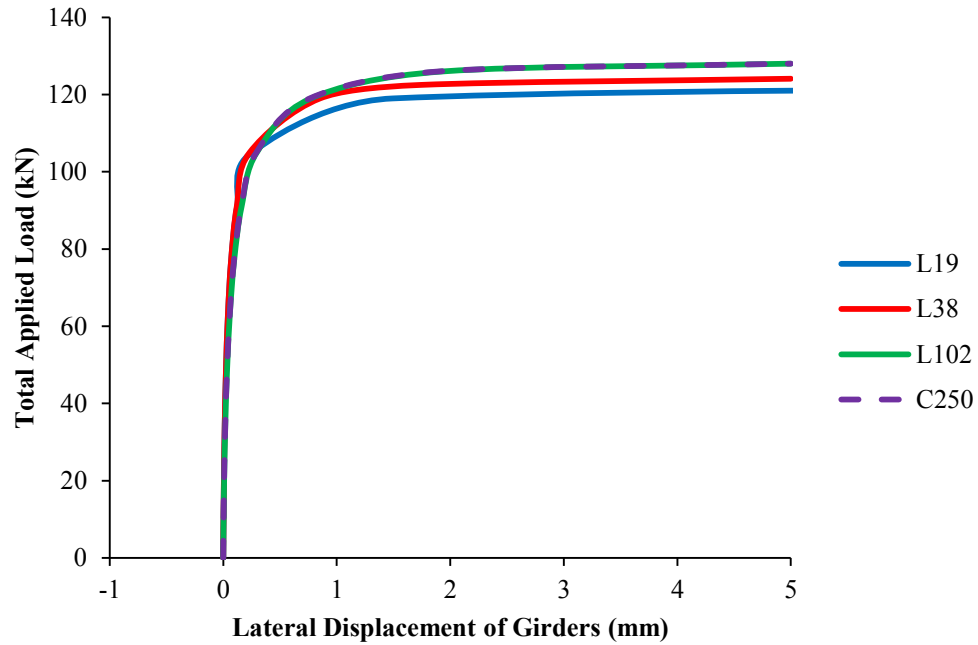


Figure 6.4 Effect of varying cross-frame stiffness on the load vs. top flange lateral displacement curves of girders.

Table 6.3 presents the FE critical moment results for cross-frames with varying member sizes. The critical moment versus cross-frame member stiffness relationship is further shown in Figure 6.5. Both the table and figure show that a variation in the brace member stiffness presents minimal change in the critical moment.

Table 6.3 FE critical moment results of three cross frames with variation in brace stiffness.

Member	β_t (N·mm/rad)	M_{cr} (kN·m)	%Difference M_{cr}
L19×19×3.2	8.62E+07	125.1	4.2
L38×38×4.8	9.22E+07	130.6	-
L102×102×13	9.50E+07	134.8	3.2
C250×30	9.51E+07	134.8	3.2

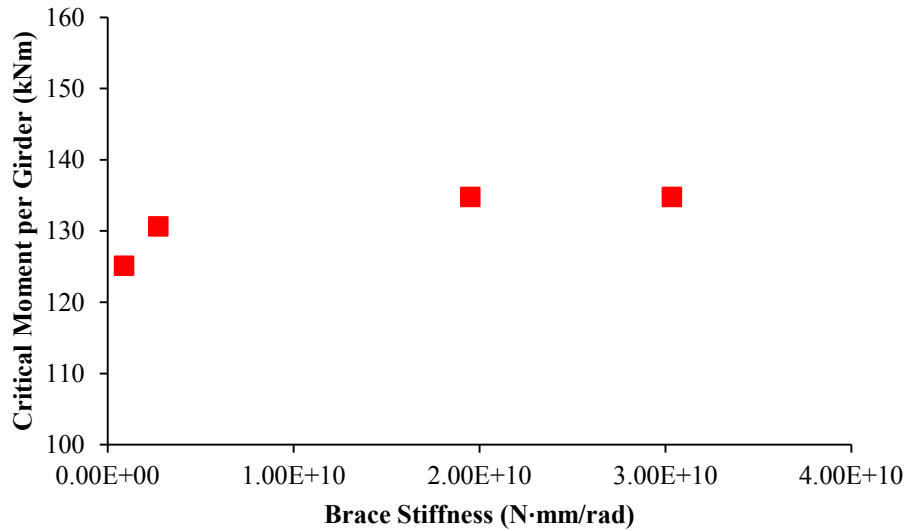


Figure 6.5 Effect of torsional cross-frame system stiffness on critical moment for varying cross-frame brace members.

6.4 NUMBER OF INTERIOR CROSS-FRAMES

The twin-girder system braced with two, three, and five interior cross-frames is studied in combination with girder spacing in this section. Table 6.4 summarizes the finite element and Equation [2.23] results. It is noted that Equation [2.23] does not account for the number of interior cross-frames in the critical moment calculation, therefore the calculated critical moment presented in Table 6.4 remains constant between varying numbers of cross-frames. The FE critical moment values are determined in the same manner as described previously. The load versus top flange lateral displacement responses for the two and five interior cross-frame arrangements are presented in Figures 6.6 and 6.7 respectively. Refer to Figure 6.2 for the critical load of the three interior cross-frame arrangements.

Table 6.4 Global elastic critical moment (kN·m) comparison with varying number of interior cross-frames.

Girder Spacing (mm)	Two Cross-Frames			Three Cross-Frames			Five Cross-Frames		
	FE	Calc. (Eqn. [2.23])	% Δ M_{cr}	FE	Calc. (Eqn. [2.23])	% Δ M_{cr}	FE	Calc. (Eqn. [2.23])	% Δ M_{cr}
500	66.0	89.0	25.8	83.0	89.0	6.7	90.8	89.0	2.0
650	88.0	114.0	22.8	107.0	114.0	6.1	115.5	114.0	1.3
800	102.0	139.0	26.6	130.6	139.0	6.0	141.6	139.0	1.9
1000	124.0	173.0	28.3	165.0	173.0	4.6	176.0	173.0	1.7

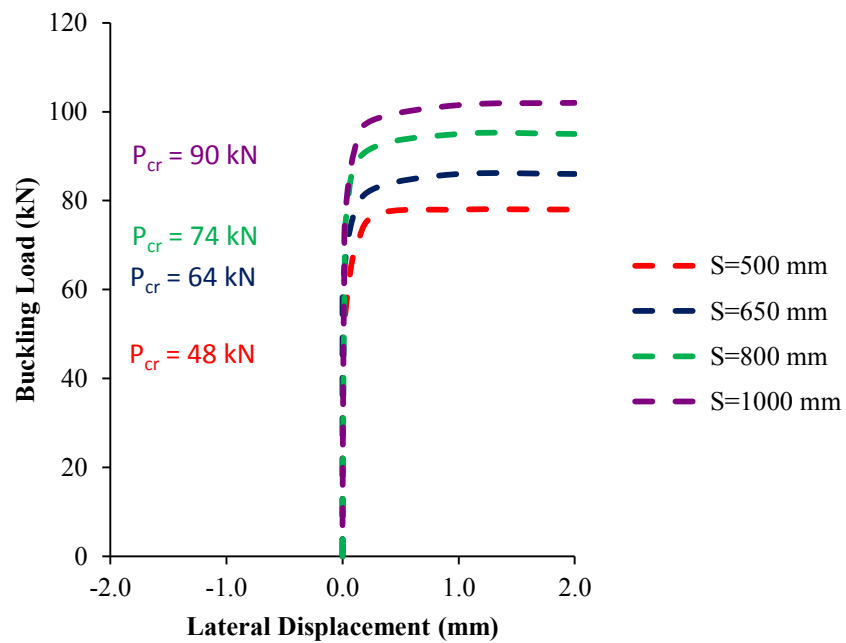


Figure 6.6 Load versus lateral displacement response of 2 interior cross-frame specimen with variable girder spacing.

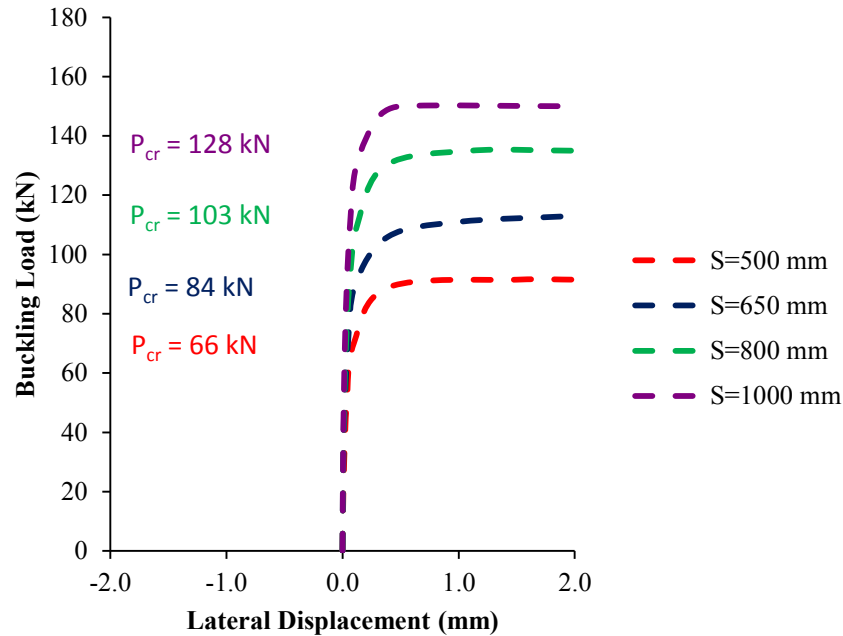


Figure 6.7 Load versus lateral displacement response of 5 interior cross-frame specimen with variable girder spacing.

Table 6.4 is graphically illustrated in Figure 6.8. As seen in both the figure and table, the effect of girder spacing as discussed previously for the three interior cross-frame arrangement is also true for two and five interior cross-frame arrangements. An increase in the girder spacing results in an increase in the critical load for all three interior cross-frame arrangements and this increase seems to be in a linear relationship with the increase in spacing. For twin girder systems with three and five interior cross-frames, the FE critical moment values are in good agreement with Equation [2.23] values with a maximum difference of 6.7% and 2.0% respectively. However, for twin-girder system with two interior cross-frames, both the table and the figure show that a significantly higher critical load in the order of 30% is provided by the equation. Equation [2.23] seems to converge with the finite element results when at least three interior cross-frames are implemented within the span but overestimate the girder capacity when only two cross-frames are present. This observation is in line with work conducted by Zhao *et al.* (2010). A modified curve reflecting a 30% reduction is seen to be in good agreement with the finite element results (Figure 6.8). This indicates that Equation [2.23] can be used to

calculate the global elastic critical buckling moment of a twin-girder system provided that it is modified for the two interior cross-frame system.

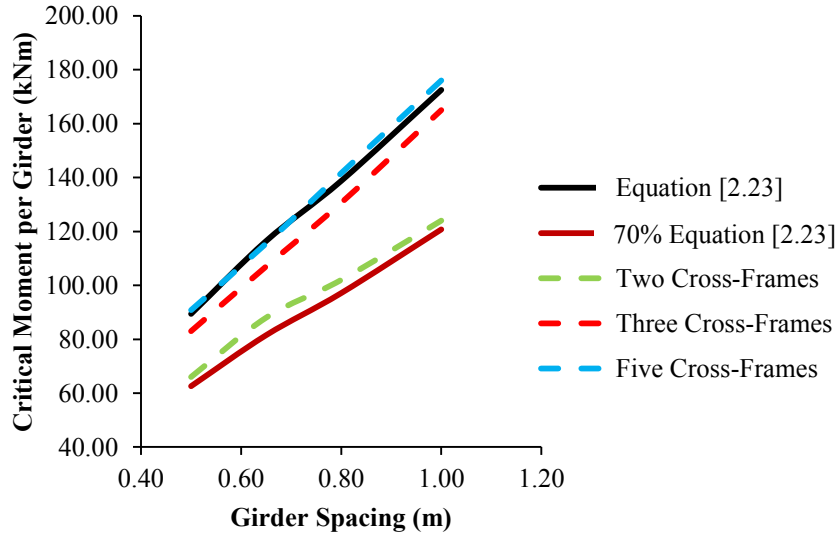


Figure 6.8 Comparison of FE and Equation [2.23] results for the number of cross-frames.

6.5 CONTINUOUS TORSIONAL BRACING STIFFNESS

As presented in Chapter 2, the critical moment of a single beam braced with only torsional braces can be determined using Equation [2.17]. In this equation, the torsional brace stiffness is explicitly accounted for providing the additional lateral stiffness to the weak axis of the girder. The effects of moment gradient and loading height are also included. The torsional brace stiffness used in the equation is in the form of continuous torsional brace stiffness as defined in Equation [2.15]. To assess the validity of Equation [2.17], the continuous torsional brace stiffness for two, three, and five interior cross-frame arrangements was calculated for a cross-frame system composed of L38×38×4.8 members and the results are listed in Table 6.5. The continuous torsional brace stiffness shows a significant increase in stiffness between two, three, and five interior cross-frames in Table 6.5. Comparing with the discrete torsional stiffness used in the previous section, the equivalent continuous torsional stiffness is a more direct indicator of the twin-girder torsional stiffness.

Table 6.5 Continuous torsional brace stiffness.

β_T (N·mm/rad/mm)			
Member	Two Cross-Frames	Three Cross-Frames	Five Cross-Frames
L38×38×4.8	1.68E+04	2.52E+04	4.20E+04

The analytical and FE critical moment values are compared in Table 6.6. The analytical values for an individual girder braced with continuous torsional bracing were based on Equation [2.17] (Yura 2001). A sample calculation is provided in Appendix E. It is noted that the FE critical moment determined in this section was obtained using the buckling load represented by the plateau after the commencement of buckling in the load versus top flange lateral displacement response. The curves for two, three, and five interior cross-frame arrangements are shown in Figure 6.9. The moment presented in Table 6.6 for one girder is determined using $(P_{cr}L/4)/2$. The rationale for using the load at buckling for this comparison is due to the fact that the torsional braces are only engaged after buckling has occurred. The table shows that Equation [2.17] yields values in good agreement with FE results with the maximum percentage difference between these two methods being around 11% for the two interior cross-frame arrangement. It also seems that the Equation [2.17] converge to FE results with more cross-frames implemented. Note that the analytical value in parenthesis for five cross-frame case is the yield moment capacity M_y of the cross-section. This value will govern the moment in design rather than 186.0 kN·m calculated using the equation. This indicates that the cross-section will yield prior to buckling. The finite element results also showed evident yielding at buckling as seen in Figure 6.10.

Table 6.6 Comparison of FE critical moment and Equation [2.17] values (kN·m).

Member	Two Cross-Frames			Three Cross-Frames			Five Cross-Frames		
	Ana.	FE	% Δ	Ana.	FE	% Δ	Ana.	FE	% Δ
L38×38×4.8	109.8	125.0	10.8	158.2	167.0	3.0	186.0 (165.9)	185.6	2.6

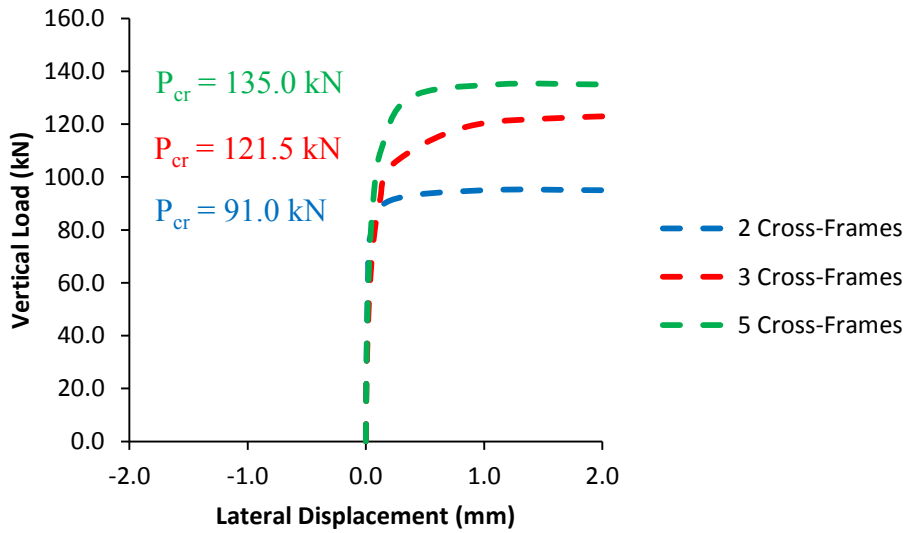


Figure 6.9 Determination of critical load from load versus top flange lateral displacement response of a girder.

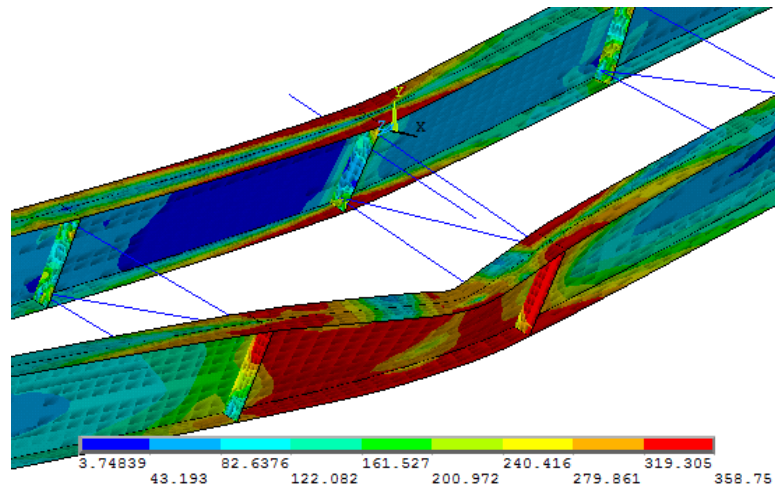


Figure 6.10 Von Mises stress at buckling for five cross-frame arrangement.

6.6 CSA S6 (2006) CRITICAL MOMENT

In this section, the validity of lateral torsional buckling design provisions specified in the current CHBDC CSA S6 (2006) standard is assessed using FE results. CSA S16 (2010) prescribes the same design equation (see Chapter 2). The elastic critical moment M_u values are calculated for a single girder with the unsupported length of beam taken as the distance between cross-frames. CSA S6 (2006) adopts the moment magnifier developed by Wong and Driver (2010) to account for effects of moment gradient in the critical moment calculation. Loading height is considered by implementing an ω_2 value of 1.0 with an effective length of $1.2L_u$, where L_u is the distance between intermediate cross-frames. Sample critical moment calculations based on CSA S6 (2006) are included in Appendix E.

The calculated critical moment values using CSA S6 (2006) including loading height effect are compared to FE values in Table 6.7. Also included in the table are FE provided torsional brace stiffness for the given cross-frame member sizes and the ideal torsional brace stiffness based on the CSA S6 (2006) critical moment using Equation [2.24]. Again, the CSA S6 (2006) value reported in parenthesis for five cross-frame case is the yield moment capacity M_y of the cross-section. The finite element moments were the same as previously presented in Table 6.6 for two, three, and five cross-frame systems.

Table 6.7 shows that the calculated critical moment from CSA S6 (2006) underestimates the two and three cross-frame cases but overestimates the five cross-frame case. This discrepancy in critical moment values is attributed to the variation between the FE provided and CSA required torsional stiffness. As shown in Table 6.7, the FE provided torsional stiffness is higher than the CSA S6 (2006) required stiffness in the case of two and three cross-frame arrangement and lower than the CSA S6 (2006) required stiffness in the case of the five cross-frame arrangement. The associated FE critical moments are then higher and lower than the corresponding CSA S6 (2006) values. This suggests the provided brace stiffness in relation to the ideal stiffness affects the magnitude of the critical moment. It should be pointed out that this stiffness requirement is not explicitly

specified in the current CSA S6 (2006) or S16 (2010) standard. Results herein indicate that if only torsional braces are present, using the unsupported length as the distance between the brace points may be unconservative as in the case of five cross-frame arrangement. If the provided stiffness of the cross-frame is less than the ideal stiffness, increasing the number of cross-frames does not increase the critical moment in proportion to the CSA S6 (2006) calculated design moment. CSA S6 (2006) gives an unrealistically high critical moment value thus resulting in an unsafe design. On the other hand, if the provided torsional bracing stiffness is equal to or greater than the required ideal stiffness, the critical moment determined using the CSA S6 (2006) procedure may be realized.

Table 6.7 Critical moment comparison between FE and CSA S6 (2006) results.

	$\beta_{T,FE-prov'd}$ (N·mm/rad)	FE (kN·m)	CSA S6 (2006) M_{cr} (kN·m) (Eqn. [2.24])	$\beta_{Ti,CSA-ideal}$ (N·mm/rad)	$\beta_{prov'd}/\beta_{ideal}$
2 Cross-Frames	9.22E + 07	125.0	67.2	4.26E + 07	2.16
3 Cross-Frames	9.22E + 07	167.0	107.5	7.28E + 07	1.27
5 Cross-Frames	9.22E + 07	185.6	220.6 (165.9)	1.84E + 08	0.50

Assuming FE values as the critical moments, an effective unbraced beam length can be calculated based on the CSA S6 (2006) procedure and the results are presented in Table 6.8. An effective length multiplier, k , is calculated using the ratio of the provided and required unbraced length of beam. As the cross-frame number increases from 2 to 3 and to 5, the k values increase from below unity to above unity. It might be reasonable to assume that when the provided torsional brace stiffness equals to the ideal torsional brace stiffness, the k value is 1.0. If the torsional brace stiffness is either less or more than the ideal brace stiffness, the k value is either less than or greater than 1.0. The relationship between the unbraced length modifier k and the ratio of provided torsional stiffness to

required torsional stiffness is shown in Figure 6.11 with the available results. The trend is not linear. It seems to suggest that the variation in k is more pronounced when $\beta_{\text{prov'd}}/\beta_{\text{ideal}}$ ratio is less than 1.2 and as the ratio increases above 1.2, the variation in k is not significant. More data points are needed to define the exact relationship between the torsional stiffness and the unbraced length that can be used in combination with CSA S6 (2006) procedure. Before this relationship is scientifically verified, it is recommended that design requirements for torsional stiffness be implemented to prevent an overestimation of the critical moment when the distance between cross-frames is used as the unbraced length of beam.

Table 6.8 Effective length factor to achieve FE results using CSA S6 (2006).

	$\beta_{\text{prov'd}}/\beta_{\text{ideal}}$	$L_{b, \text{prov'd}}$ (mm)	$L_{b, \text{ideal}}$ (mm)	$k = \frac{L_{b, \text{ideal}}}{L_{b, \text{prov'd}}}$
2 Cross-Frames	2.17	3667	2517	0.68
3 Cross-Frames	1.27	2750	2137	0.78
5 Cross-Frames	0.50	1833	2015	1.10

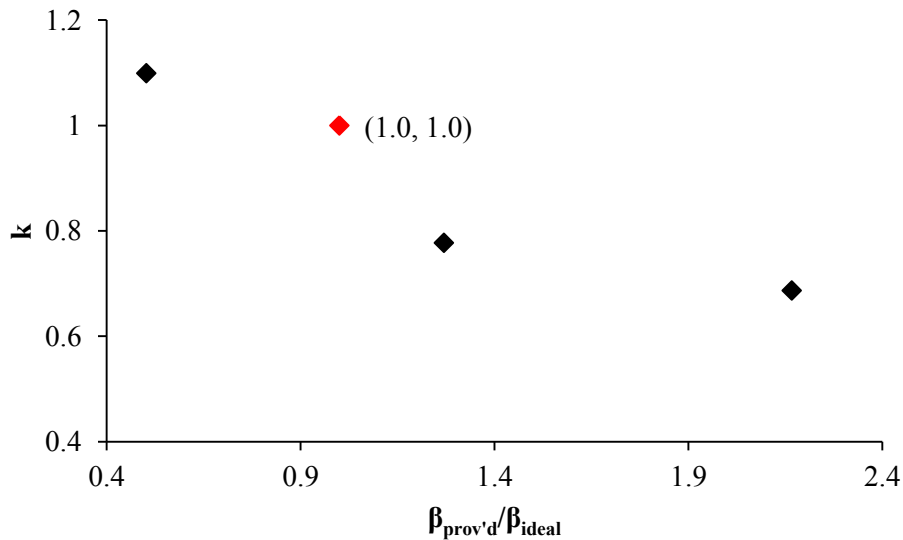


Figure 6.11 Relationship between unbraced length modifier k and ratio of provided torsional stiffness to ideal torsional stiffness.

In light of previous discussion which indicates that the loading height effect is not significant for twin girder systems with torsional braces only, the CSA S6 (2006) critical moment values are also calculated without considering the loading height effect and compared with the FE results in Table 6.9. It can be seen that the critical moment calculated without considering loading height effect for two cross-frame case is a lot closer to the FE result. For 3 and 5 cross-frames, the critical moment is over estimated resulting in the yielding strength of the cross-section governing the critical moment. It confirms that in the case of twin girder systems with torsional braces, the loading height effect may be ignored when using CSA S6 (2006) critical moment equations.

Table 6.9 Comparison with CSA S6 (2006) without loading height effect.

	FE (kN·m)	CSA S6 (2006) (kN·m) Top Flange Loading	CSA S6 (2006) (kN·m) No Top Flange Loading
2 Cross-Frames	125.0	67.2	96.3
3 Cross-Frames	167.0	107.5	190.7 (165.9)
5 Cross-Frames	185.6	220.6 (165.9)	365.7 (165.9)

6.7 BRACE FORCE

This section studies the forces developed in the torsional braces at buckling. As mentioned in Chapter 2, CSA S16 (2010) and S6 (2006) provide different requirements for design brace forces. CSA S16 (2010) suggests that a lateral or torsional brace which supports a member against buckling should be designed to resist 2% of the compressive force in the braced member at the location of the brace point. However, CSA S6 (2006) indicates that a 1% compressive force is required to provide an adequate brace point. This discrepancy between codes is believed to be attributed to the different tolerances for the maximum initial out-of-straightness that was considered in the derivation of the brace force requirement. Both standards refer to Winter (1960) where a percentage of the member's compressive force was used as a reasonable estimate for the design of a lateral brace to resist buckling of a member.

The brace forces developed at the critical moment from the FE analysis for all three cross-frame arrangements are compared to the theoretical brace force of CSA S6 (2006). The geometry of the cross-frame system from the FE analysis used in the brace force calculation is provided in Figure 6.12a. The calculation of the CSA S6 (2006) diagonal brace force was calculated in accordance with Figure 6.12b where L_c is the length of the diagonal member. In this case, F is 1% of the flange compressive force at the buckling load and the h_b and S are 340 and 800 mm respectively.

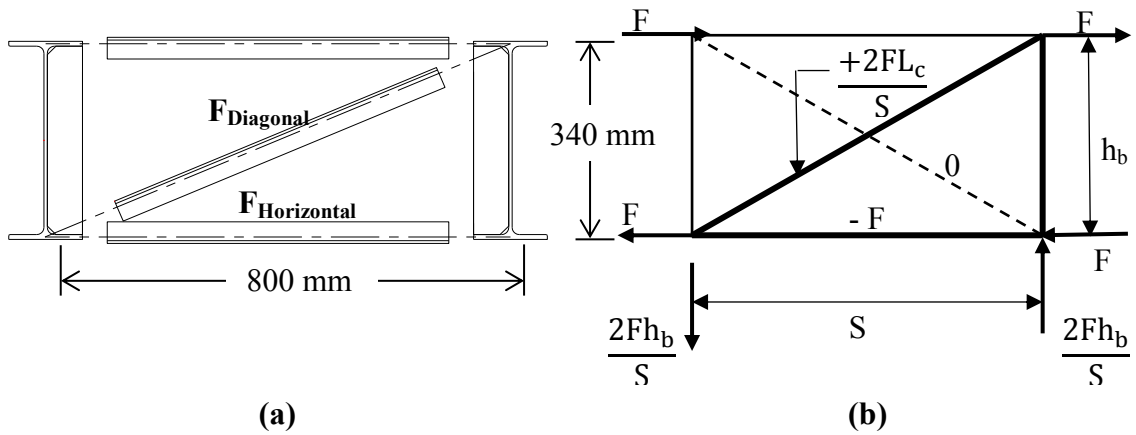


Figure 6.12 Schematic for: (a) cross-frame geometry; and (b) brace force diagram.

The brace force comparison between the finite element results and CSA S6 (2006) code values is presented in Table 6.10. The horizontal and diagonal brace forces are presented in the brace force versus vertical load curves for the two, three, and five interior cross-frame arrangements in Figure 6.13. For example, the brace forces for the three cross-frame arrangement presented in the table are identified in the figure with respect to the critical load. It is observed that up to the commencement of buckling, the brace force is practically zero. The brace forces increase significantly after buckling occurs. The table shows that brace forces developed in cross-frame members are dependent on the ratio of provided to ideal torsional stiffness. In the case of two cross-frame arrangement where the ratio of the provided-to-ideal torsional stiffness is greater than 2, the finite element brace forces are lower but close to the CSA S6 (2006) specified values. In the case of three cross-frame arrangement where the ratio of the provided-to-ideal torsional stiffness

is greater than 1 but less than 2, the finite element brace forces are more than 2 times the CSA S6 (2006) specified values. In the case of five cross-frame arrangement where the ratio of the provided-to-ideal torsional stiffness is 0.5, the finite element brace forces are about 6 times the CSA S6 (2006) specified values. This indicates that the 1% compressive force as brace force rule is only valid if the provided torsional stiffness is at least twice the ideal stiffness.

Table 6.10 Cross-frame bracing forces.

	FE (kN)		CSA S6 (2006) (kN)		$\beta_{\text{prov'd}}/\beta_{\text{ideal}}$
	$F_{\text{Hor.}}$	$F_{\text{Dia.}}$	$F_{\text{Hor.}}$	$F_{\text{Dia.}}$	
2 Cross-Frames	3.5	6.0	4.9	10.7	2.17
3 Cross-Frames	24.3	40.1	9.8	21.4	1.27
5 Cross-Frames	63.5	91.3	10.9	23.8	0.50

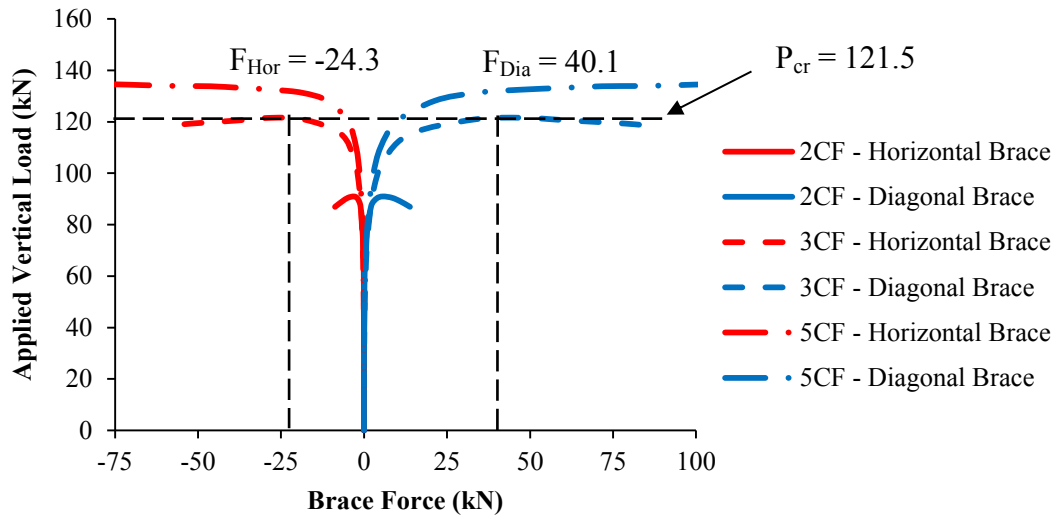
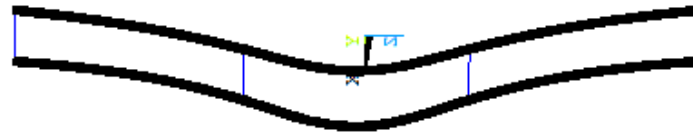


Figure 6.13 Applied load vs. brace force response of cross-frame member.

6.8 FAILURE MODES

All the FE specimens investigated in the parametric study failed by global buckling. The buckled shape presented in Figure 6.14 for all cross-frame configurations is in the form of a half sine wave. Regardless of the number of the cross-frame implemented and the

stiffness of the cross-frame, the buckled shape for beams that are braced with only torsional braces seems to remain in a half sine wave.



(a) Two intermediate cross-frame specimen



(b) Three intermediate cross-frame specimen



(c) Five intermediate cross-frame specimen

Figure 6.14 FE buckled shape.

CHAPTER 7 CONCLUSIONS AND RECOMMENDATIONS

7.1 SUMMARY

This study was conducted to investigate the efficiency of torsional braces provided by cross-frames for lateral torsional stability of twin plate girders. The applicability of lateral torsional stability design procedures contained in the current Canadian Highway Bridge Design Code CSA S6 (2006) is also examined. Both experimentation and numerical analyses were undertaken.

In the experimental portion, three twin-girder specimens were tested subjected to a midspan loading where two specimens were implemented with only torsional braces in the form of cross-frames and one specimen with a combination of torsional and lateral braces. The buckling loads and the load versus deflections responses were presented and discussed in graph and tabular formats. The experimental results were compared with values obtained from several analytical methods and CSA S6 (2006) code. The observations and implications were noted and discussed.

The numerical portion of the research included the development of a finite element model and a subsequent study to investigate the effects of several parameters on the lateral torsional stability of the twin-girder systems. The finite element model was verified using the test results. The parameters considered in the numerical study included girder spacing, brace stiffness, and number of braces. The numerical results were used to assess the accuracy of the current design equations and to provide information on the stiffness and force requirement for torsional braces in twin-girder lateral torsional buckling check.

7.2 CONCLUSIONS

The following conclusions are derived from both the experimental and numerical study of this research:

- The experimental results demonstrated that a combination of lateral and torsional bracing (specimen C2) increased the critical moment of the specimen by a factor of 1.75 in comparison to a specimen braced with only torsional braces. Incorporating lateral and torsional bracing also allows for beams to be designed to fail by yielding of the section rather than buckling.
- The finite element results compared well with experimental results, suggesting that the finite element modeling is a good alternative for further studies to predict the behavior of twin girder specimens.
- It is found that increasing the girder spacing linearly increases the global elastic critical moment of the twin girder system. An increase in the number of torsional braces results in an increase in critical moment of a twin-girder specimen. However, this increase is much more significant when the number of interior torsional braces increases from 2 to 3. The critical moment value seems to converge when the interior torsional braces are greater than 3. Changing the brace member size, even to a large degree, does not show any significant effect on the critical moment of the girder system. However, the torsional stiffness is dependent on the girder cross-section.
- The comparison between the numerical results and those obtained from existing analytical methods provided by Yura (2001) and Yura *et al.* (2008) showed that the analytical methods are reasonably accurate in providing the elastic critical moment values. One exception is when there are only two interior cross-frames present, which results in an 11% (Yura, 2001) or 30% (Yura *et al.*, 2008) difference in critical moment values..
- The comparison from the parametric study between the numerical and code values obtained from CSA S6 (2006) showed that the critical moment value is related to the ratio of provided-to-ideal torsional stiffness. When the ratio is greater than unity, the current lateral torsional buckling equation in the code provides conservative values; when the ratio is less than unity, the code provides

overestimation of the critical moment. The application of an effective length modifier further showed that an effective unbraced length can be implemented in the code equation for evaluation of critical moment for girder systems with torsional braces only. A relationship between this effective length modifier and the ratio of provided-to-ideal torsional stiffness is proposed.

- The brace force study confirmed that for twin-girder systems with only torsional braces, a stiffness equal to twice the ideal stiffness needs to be provided in order for the “1% compressive force rule” for brace force design to be valid.
- The failure mode of all finite element model specimens is by global buckling regardless of the magnitude of the torsional stiffness. Although further study is needed, it seems that the global buckling is the governing failure and buckling between brace points is only theoretical but cannot be achieved physically.

7.3 RECOMMENDATIONS

The following recommendations are developed from observations during the experimental and numerical study:

- Implement two point loading system to achieve constant moment region at girder midspan. This would enable the moment magnifier (C_b or ω_2) to be considered as 1.0 eliminating some uncertainties in the calculation of the critical moment.
- Install lateral restraints on either side of the test specimen to prevent excessive lateral displacements during buckling. Implementing a system that will prevent the specimen from leaving its bearings will maintain a safe environment during testing.
- Install web stiffeners beneath the loading points to minimize the possibility of web distortion which can contribute to increased normal stresses in the compression flange.

- Modify the loading system to be essentially frictionless. This could be achieved in a variety of ways: implementation of high molecular Teflon on the roller surface of the pivot assembly; or construction of a pinned sway frame attached to a jack secured beneath the specimen with the capability to load by pulling the frame towards the floor.
- Install rosette strain gauges at girder midspan to determine the magnitude of the strong axis warping stresses and the weak axis normal stresses that occur during buckling.
- Residual stresses should be considered in finite element modelling.
- Torsional braces should be modelled with twice the ideal stiffness to verify that providing twice the ideal stiffness does minimize the out-of plane deformations along with the brace force as studied in the parametric study.
- Finite element modelling of full scale bridge girders should be conducted to determine the effects of loading height, torsional brace stiffness, material or geometric imperfections, and unbraced length of girder between torsional braces. It is suggested that loading conditions similar to those of construction loading be applied to the finite element model based on non-composite behaviour.

REFERENCES

- American Institute of Steel Construction. (2005). *Specification for Structural Steel Buildings (AISC 360)*. Chicago.
- American Institute of Steel Construction. (2010). *Specification for Structural Steel Buildings (AISC 360)*. Chicago.
- American Society for Testing and Materials. (2012). *Standard Test Methods and Definitions for Mechanical Testing of Steel Products*. West Conshohocken.
- Canadian Standards Association. (2006). *Canadian Highway Bridge Design Code (CSA S6)*. Toronto: CSA International.
- Canadian Standards Association. (2010). *Design of Steel Structures (CSA S16)* (Tenth ed.). Toronto: Canadian Institute of Steel Construction.
- Coffelt, S. J. (2010). *Stability Analysis of Single and Double Steel Girders During Construction*. Knoxville: University of Tennessee.
- Elsayed, S. T. (2000). *Lateral Torsional Buckling of HPS Bridge I-Girders With Cost-Effective Cross-Frame Spacing*. Lehigh University.
- Galambos, T. V. (1998). *Guide to Stability Design Criteria for Metal Structures* (Fifth ed.). John Wiley & Sons.
- Geng-Shu, T., & Shao-Fan, C. (1988). Buckling of Laterally and Torsionally Braced Beams. *Journal of Constructional Steel Research*, 11, 41-55.
- Geng-Shu, T., & Shao-Fan, C. (1989). The Elastic Buckling of Interbraced Girders. *Journal of Constructional Steel Research*, 14, 87-105.
- Gil, H., & Yura, J. A. (1999). Bracing Requirements of Inelastic Columns. *Journal of Constructional Steel Research*, 1-19.
- Helwig, T. A., & Wang, L. (2003). *Cross-Frame and Diaphragm Behaviour for Steel Bridges with Skewed Support*. Texas Department of Transportation.
- Helwig, T., Yura, J. A., & Frank, K. H. (1993). Bracing Forces in Diaphragms and Cross Frames. Proceedings, *SSRC Conference* (pp. 129-137). Milwaukee, WI: Structural Stability Research Council.
- Kirby, P. A., & Nethercot, D. A. (1979). *Design for Structural Stability*. New York: John Wiley & Sons.
- Kitipornchai, S., & Richter, N. R. (1978). Lateral Buckling of Beams with Discrete Braces. *Metal Structures*.
- Kitipornchai, S., Aust, M., & Richter, N. J. (1978). Elastic Lateral Buckling of I-Beams with Discrete Intermediate Restraints. *Civil Engineering Transactions*, 105-111.
- Kozy, B., & Tunstall, S. (2007). Stability Analysis and Bracing for System Buckling in Twin I-Girder Bridges. *Bridge Structures*, 3(4), 149-163.
- Lusas. (2013). Lusas Bridge Plus, Version 14.7. *Finite Element Analysis Ltd.*, United Kingdom.

- Milner, H. R. (1977). Design of Simply Supported Beams Braced Against Twisting on the Tension Flange. *Civil Engineering Transactions* (pp. 84-91). Australia: Institute of Engineers.
- Nethercot, D. A. (1989, April). The Design of Bracing Systems for Plate Girder Bridges. *Structural Engineering/Earthquake Engineering*, 6(1), 23-34.
- Nethercot, D. A., & Rockey, K. C. (1972). A Unified Approach to the Elastic Lateral Buckling of Beams. *AISC Engineering Journal*, 9, 96-107.
- Nguyen, C. T., Moon, J., Le, V. N., & Lee, H.-E. (2010). Lateral-torsional Buckling of I-Girders with Discrete Torsional Bracings. *Journal of Constructional Steel Research*, 170-177.
- Phillips, B. A. (1990). *Bracing Requirements for Elastic Steel Beams*. Master of Science in Engineering thesis, University of Texas at Austin.
- Roddis, W. K., Winters, E. L., & Baghernejad, S. (2008). *Cross-Frame Diaphragm Bracing of Steel Bridge Girders*. Kansas: Kansas Department of Transportation.
- Salvadori, M. G. (1955). Lateral Buckling of I-Beams. *ASCE Transactions*, 120, 1165.
- Taylor, A. C., & Ojalvo, M. (1966). Torsional Restraint of Lateral Buckling. *Journal of Structural Division*, 92(ST2), 115-129.
- Timoshenko, S. P., & Gere, J. M. (1961). *Theory of Elastic Stability*. New York: McGraw-Hill.
- Trahair, N. S. (1993). *Flexural-Torsional Buckling of Structures*. London: E & FN Spon.
- Trahair, N. S., & Kitipornchai, S. (1972). Buckling of Inelastic I-Beams Under Uniform Moment. *Journal of the Structural Division*, 2551-2566.
- Vishay Precision Group. (2011). *Errors Due to Transverse Sensitivity in Strain Gages*.
- Wang, L., & Helwig, T. A. (2005). Critical Imperfections for Beam Bracing Systems. *Journal of Structural Engineering*, 131(6), 933-940.
- Winter, G. (1960). Lateral Bracing of Columns and Beams. *ASCE Transactions*, 125(1), 809-825.
- Wong, E., & Driver, R. G. (2010). Critical Evaluation of Equivalent Moment Factor Procedures for Laterally Unsupported Beams. *Engineering Journal*, 20.
- Yura, J. A. (2001). Fundamentals of Beam Bracing. *Engineering Journal*, 11-26.
- Yura, J. A., & Chen, B. (2005). Structural Bracing. In W. F. Chen, & E. M. Liu, *Handbook of Structural Engineering* (Second ed., pp. 1-23). CRC Press.
- Yura, J. A., & Helwig, T. (1996). *Bracing for Stability - Beam Buckling*.
- Yura, J. A., Helwig, T., Herman, R., & Zhou, C. (2008). Global Lateral Buckling of I-Shaped Girder Systems. *Journal of Structural Engineering*, 134(9), 1487-1494.
- Yura, J. A., Phillips, B., Raju, S., & Webb, S. (1992). *Bracing of Steel Beams in Bridges*. Austin: US Department of Transportation, Federal Highway Administration.

- Zhao, Q., Yu, B., & Burdette, E. G. (2010). Effects of Cross-Frame on Stability of Double I-Girder System Under Erection. *Journal of the Transportation Research Board*, 57-62.
- Zhao, Q., Yu, B., & Burdette, E. G. (2011). Simplified Erection Guidelines for Double I-Girder Systems during Bridge Construction. *Structures Congress*, 190-202.
- Ziemian, R. D. (2010). *Guide to Stability Design Criteria for Metal Structures* (Sixth ed.). John Wiley & Sons.

APPENDIX A

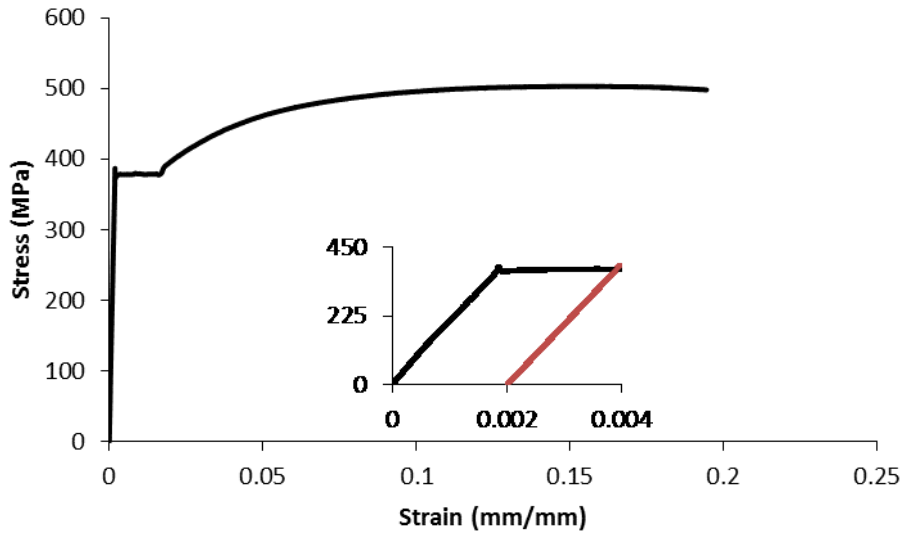


Figure A.1 Coupon OF 1 stress-strain curve.

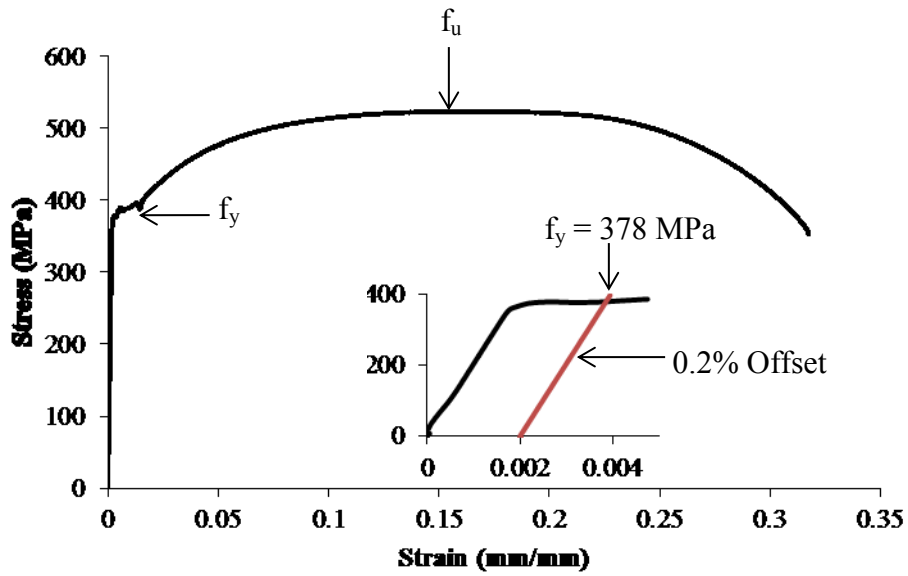


Figure A.2 Coupon OF 2 stress-strain curve.

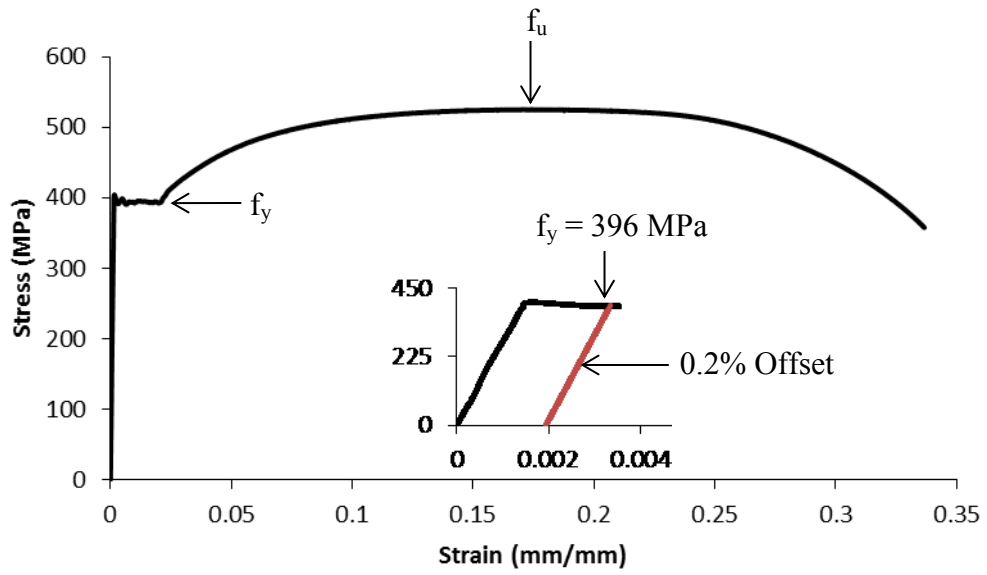


Figure A.3 Coupon OF 3 stress-strain curve.

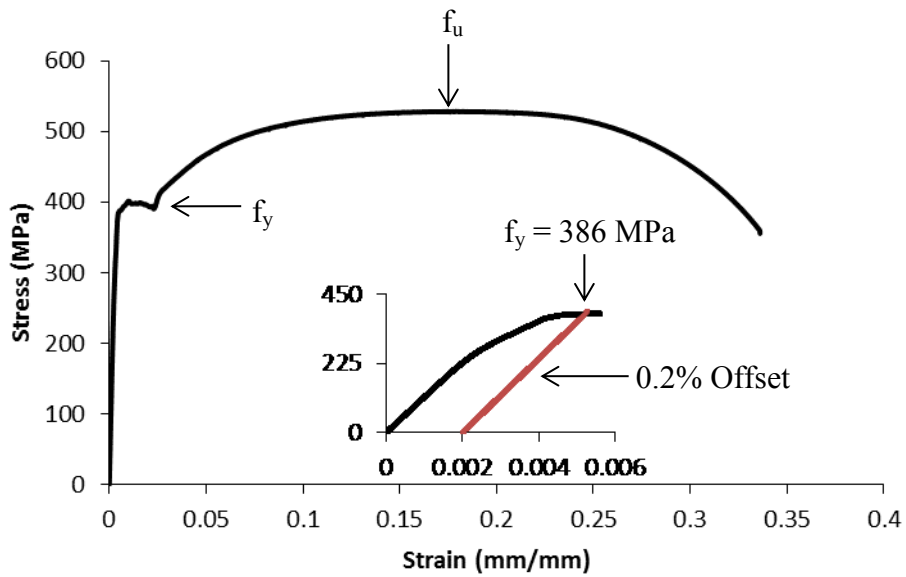


Figure A.4 Coupon OF 4 stress-strain curve.

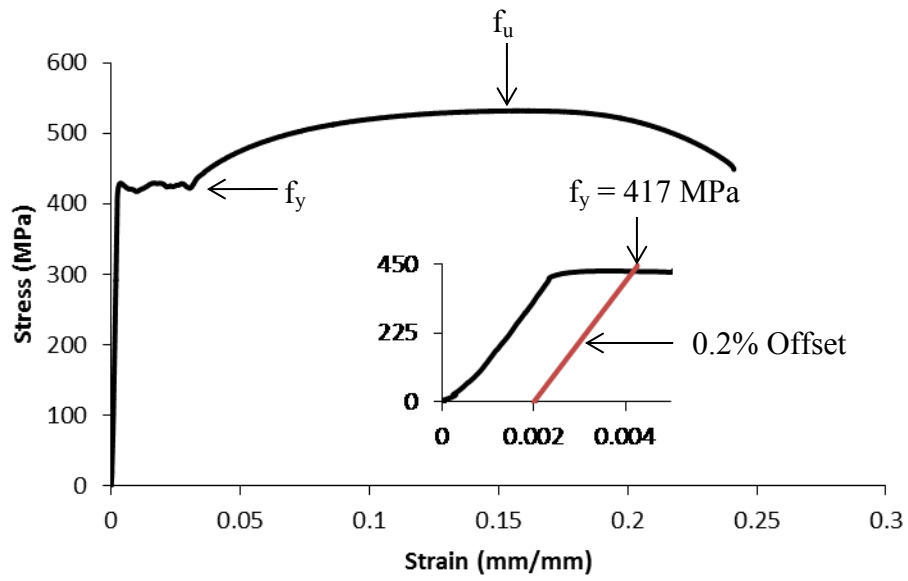


Figure A.5 Coupon OW 1 stress-strain curve.

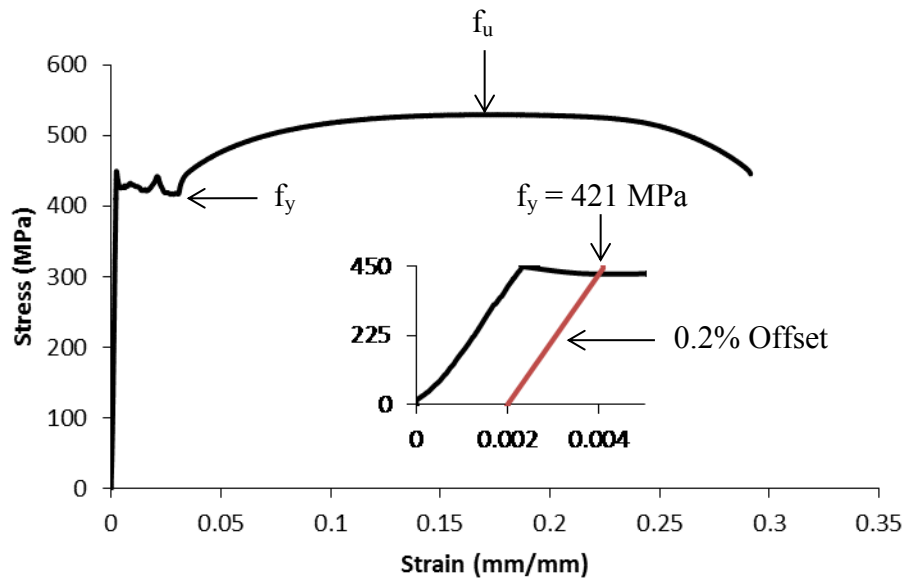


Figure A.6 Coupon OW 2 stress-strain curve.

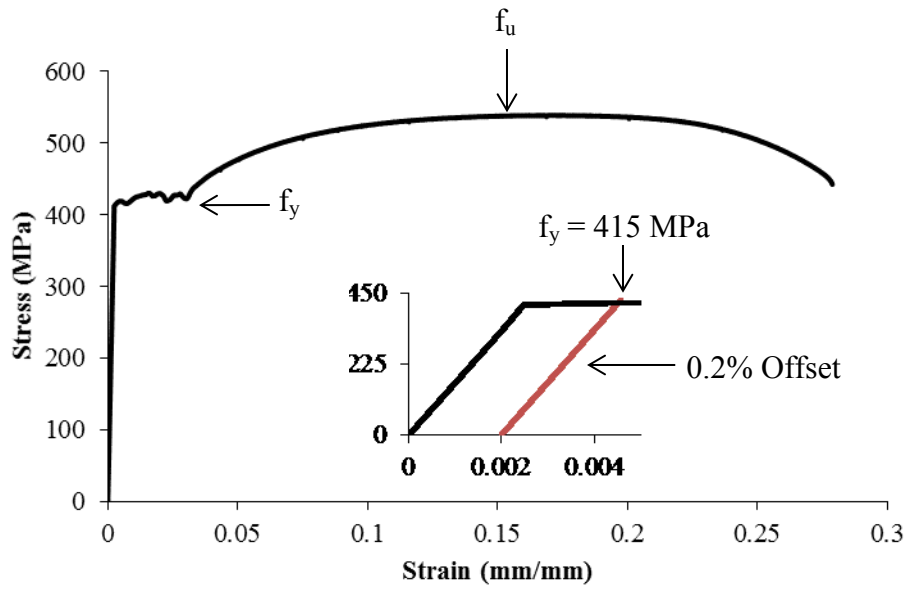


Figure A.7 Coupon OW 3 stress-strain curve.

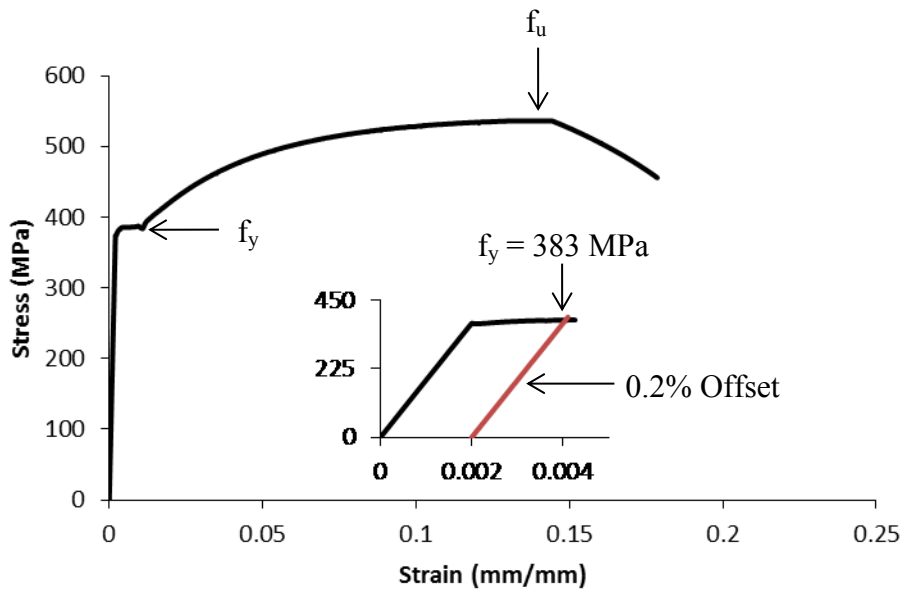


Figure A.8 Coupon NF 1 stress-strain curve.

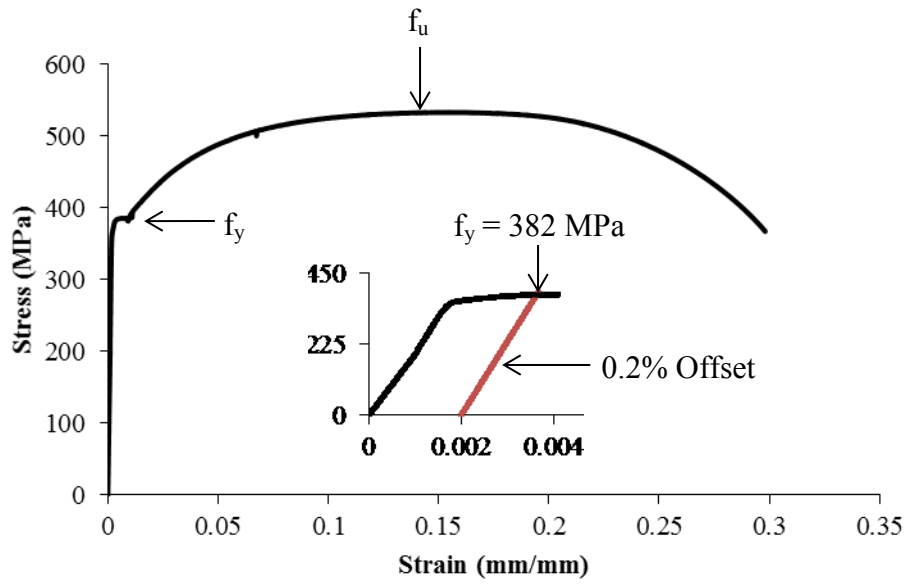


Figure A.9 Coupon NF 2 stress-strain curve.

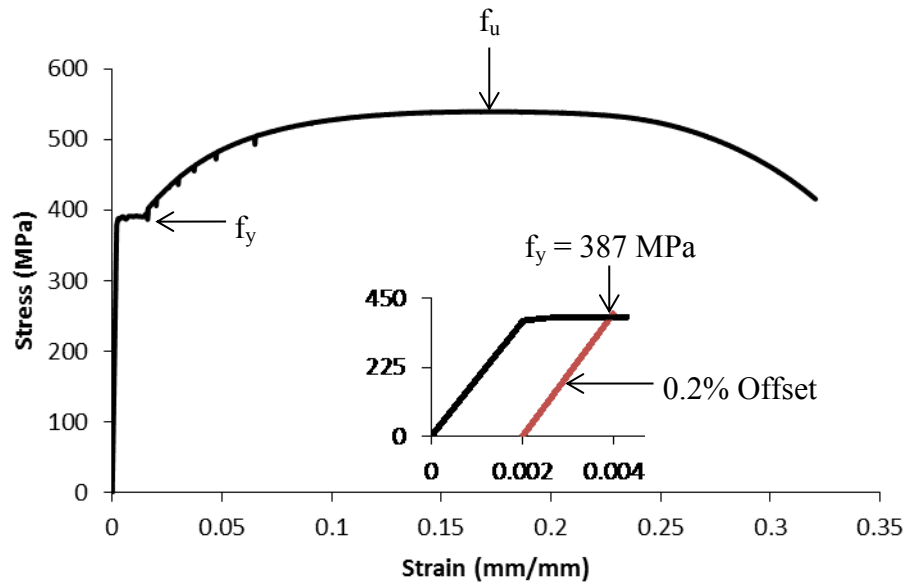


Figure A.10 Coupon NF 3 stress-strain curve.

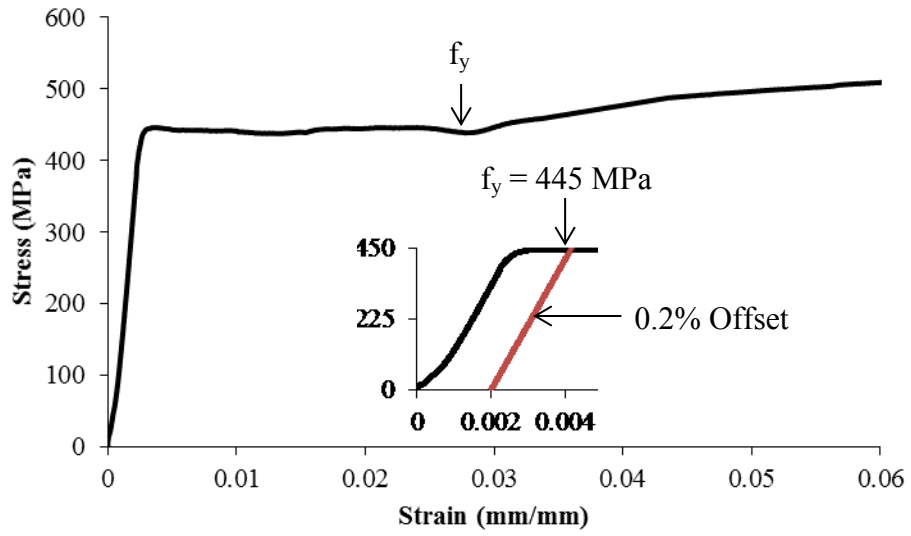


Figure A.11 Coupon NW 1 stress-strain curve.

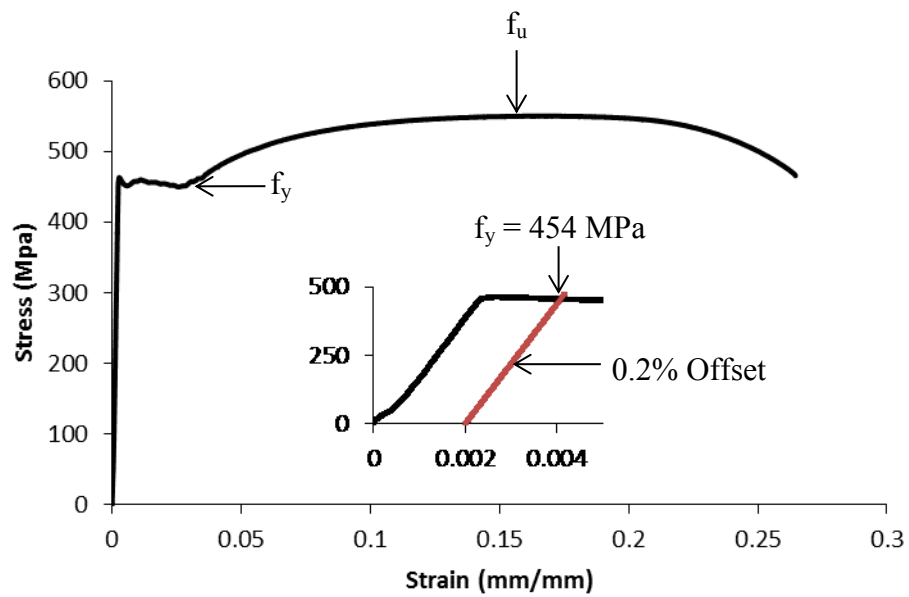


Figure A.12 Coupon NW 2 stress-strain curve.

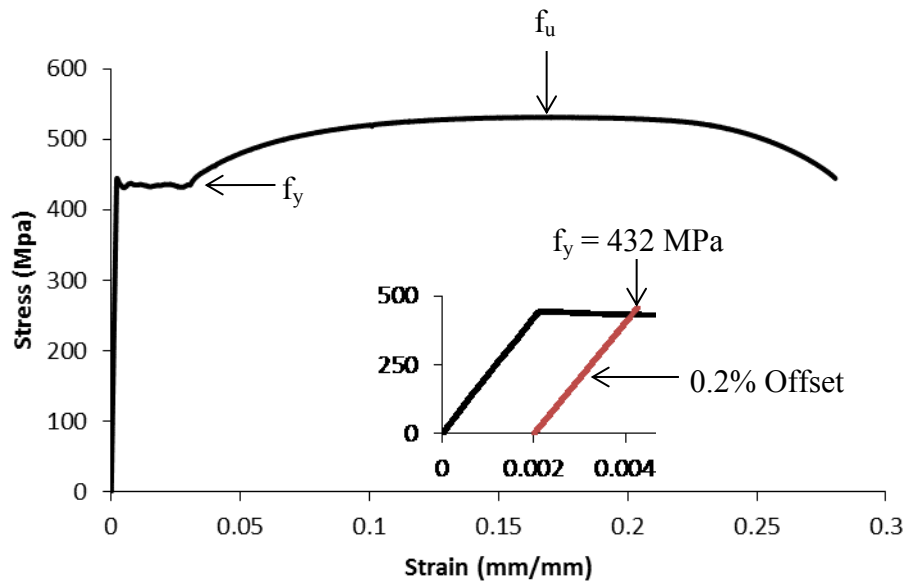


Figure A.13 Coupon NW 3 stress-strain curve.

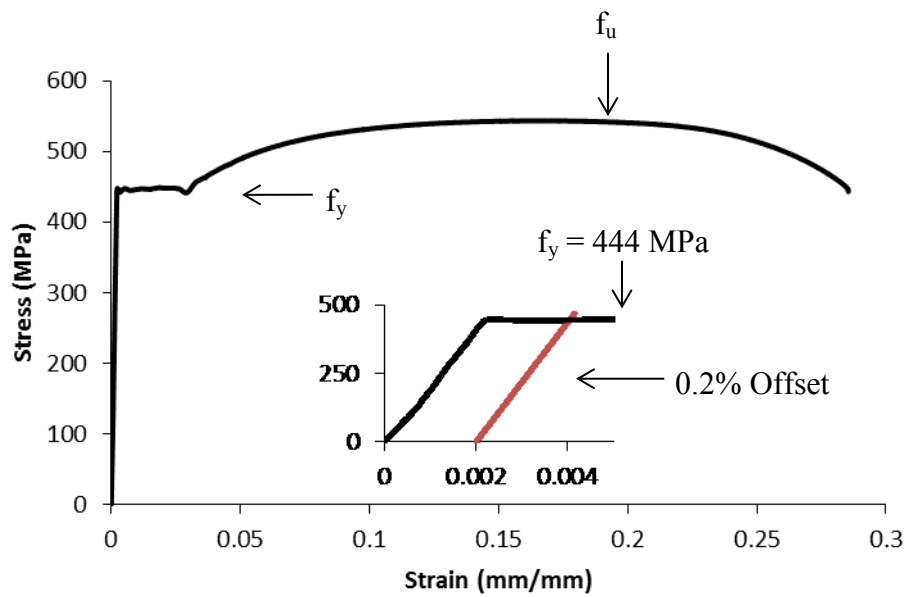


Figure A.14 Coupon NW 4 stress-strain curve.

APPENDIX B

Table B.1 Critical moment calculation of specimen C1-2 calculated using continuous torsional brace stiffness (for Table 4.5; Taylor and Ojalvo, 1966).

Section Properties			Critical Moment Capacity:
L =	11000	mm	$M_{cr} = \frac{\pi}{L} \sqrt{EI_y GJ + \frac{\pi^2 E^2 I_y^2 h^2}{4L^2} + \frac{\bar{\beta}_T L^2 EI_y}{\pi^2}} \leq M_y$
E =	209819	MPa	
$I_y =$	2.91E+06	mm ⁴	
G =	77000	MPa	
J =	8.59E+04	mm ⁴	
h =	349	mm	
$\beta_t =$	9.70E+07	N mm	
$\beta_T =$	1.76E+04	(N mm/rad)/mm	
n =	2		

Torsional stiffness of single cross-frame:

$$\frac{1}{\beta_t} = \frac{1}{\beta_b} + \frac{1}{\beta_{sec}} + \frac{1}{\beta_g}$$

$$1/\beta_t = 1.03E-08 \text{ rad / N mm}$$

Torsional stiffness of single brace:

$$\beta_b = \frac{ES^2 h_b^2}{\frac{2L_c^3}{A_c} + \frac{S^3}{A_h}}$$

$$\beta_b = 3.07E+09 \text{ N mm / rad}$$

$$S = 760 \text{ mm}$$

$$h_b = 330 \text{ mm}$$

$$L_c = 800 \text{ mm}$$

$$A_{c/h} = 340 \text{ mm}^2$$

Torsional Stiffness of girder:

$$\beta_g = \frac{12S^2 EI_x}{L^3}$$

$$\beta_g = 1.00E+08 \text{ N mm / rad}$$

$$S = 800 \text{ mm}$$

$$I_x = 8.27E+07 \text{ mm}^4$$

$$L = 11000 \text{ mm}$$

Torsional Stiffness of web stiffener:

$$\beta_{sec} = 3.3 \frac{E}{h} \left(\frac{(N+1.5h)t_w^3}{12} + \frac{t_s b_s^3}{12} \right)$$

$$\beta_{sec} = \text{N/A} \text{ N mm / rad}$$

Web distortion at cross-frame is prevented since web stiffener is welded to top and bottom flanges. Therefore web distortion is prevented.

$$M_{cr} = 106 \text{ kN m} \quad \text{Single Beam} < M_y = 182 \text{ kN m} \quad \text{Adequate}$$

$$M_{cr} = 212 \text{ kN m} \quad \text{Two Beams}$$

versus

$$M_{cr-EXP} = 209 \text{ kN m} \quad \text{Specimen C1-2}$$

$$\% \Delta = -1.44 \%$$

Table B.2 Simplified critical moment calculation of specimen C1-2 calculated using continuous torsional brace stiffness (for Table 4.5; Phillips, 1990).

Section Properties	
L = 11000	mm
E = 209819	MPa
I _y = 2.91E+06	mm ⁴
G = 77000	MPa
J = 8.59E+04	mm ⁴
C _w = 8.43E+10	mm ⁶

$$M_{cr} = \sqrt{M_o^2 + EI_y \beta_T}$$

M_o = 18.15 kN m without warping

$$\beta_T = \frac{\beta_t n}{L}$$

β _t = 89976515.5	N mm / rad
β _T = 16359.4	(N mm / rad)/mm

See below for calculations of cross-frame torsional stiffness

Torsional stiffness of single cross-frame:

$$1/\beta_t = 1.11E-08 \text{ rad / N mm}$$

$$\frac{1}{\beta_t} = \frac{1}{C_t \beta_b} + \frac{1}{\beta_{sec}}$$

Torsional stiffness of brace member:

$$\beta_b = 3.07E+09 \text{ N mm / rad}$$

$$\beta_b = \frac{ES^2 h_b^2}{\frac{2L_c^3}{A_c} + \frac{S^3}{A_h}}$$

$$S = 760 \text{ mm}$$

$$h_b = 330 \text{ mm}$$

$$L_c = 800 \text{ mm}$$

$$A_{c/h} = 340 \text{ mm}^2$$

Calculation of C_t:

$$C_t = \frac{1}{1 + 3000 \frac{\Delta_o}{L}}$$

$$\Delta = 9 \text{ mm}$$

$$C_t = 0.289474$$

Torsional Stiffness of girder:

$$\beta_g = \frac{12S^2 EI_x}{L^3}$$

$$\beta_g = 1.00E+08 \text{ N mm / rad}$$

$$S = 800 \text{ mm}$$

$$I_x = 8.27E+07 \text{ mm}^4$$

$$L = 11000 \text{ mm}$$

Torsional Stiffness of web stiffener:

$$\beta_{sec} = \text{N/A} \text{ N mm / rad}$$

$$\beta_{sec} = 3.3 \frac{E}{h} \left(\frac{(N+1.5h)t_w^3}{12} + \frac{t_s b_s^3}{12} \right)$$

Web distortion at cross-frame is prevented since web stiffener is welded to top and bottom flanges. Therefore web distortion is prevented.

M _{cr} = 99.9	kN m	Single Beam < M _y = 182	kN m	Adequate
M _{cr} = 200	kN m	Two Beams		
versus				
M _{cr-EXP} = 209	kN m	Specimen C1-2		
%Δ = 4.36	%			

Table B.3 Simplified critical moment calculation of specimen C1-2 calculated using continuous torsional brace stiffness (for Table 4.5; Yura, 2001).

Section Properties

L =	11000	mm
E =	209819	MPa
I _y =	2.91E+06	mm ⁴
G =	77000	MPa
J =	8.59E+04	mm ⁴
C _w =	8.43E+10	mm ⁶

$$M_{cr} = \sqrt{C_{bu}^2 M_o^2 + \frac{C_{bb}^2 \beta_T E I_y}{C_T}} \leq M_y$$

M_o = 18.15 kN m

n =	2	
β _t =	96807664	N mm
β _T =	17601	N mm
C _{bu} =	1.26	
C _{bb} =	1.08	
C _T =	1	

$$\beta_T = \frac{\beta_t n}{L}$$

See below for calculations of cross-frame torsional stiffness

Torsional stiffness of single cross-frame system:

$$\frac{1}{\beta_t} = \frac{1}{\beta_b} + \frac{1}{\beta_g}$$

1/β_t = 1.03E-08 rad / N mm

Torsional stiffness of brace member:

$$\beta_b = \frac{ES^2 h_b^2}{\frac{2L_c^3}{A_c} + \frac{S^3}{Ah}}$$

β_b = 2.92E+09 N mm / rad

S = 760 mm

h_b = 330 mm

L_c = 800 mm

A_{C/H} = 340 mm²

E = 200000 MPa

Torsional Stiffness of girder:

$$\beta_g = \frac{12S^2 E I_x}{L^3}$$

β_g = 1.00E+08 N mm / rad

S = 800 mm

I_x = 8.27E+07 mm⁴

L = 11000 mm

Torsional Stiffness of web stiffener:

$$\beta_{sec} = 3.3 \frac{E}{h} \left(\frac{(N+1.5h)t_w^3}{12} + \frac{t_s b_s^3}{12} \right)$$

β_{sec} = N/A N mm / rad

Web distortion at cross-frame is prevented since web stiffener is welded to top and bottom flanges. Therefore web distortion is prevented.

M_{cr} = 114 kN m Single Beam < M_y = 182 kN m Adequate

M_{cr} = 229 kN m Two Beams

versus

M_{cr-EXP} = 209 kN m Specimen C1-2

%Δ = -9.35 %

Table B.4 Global elastic buckling moment of specimen C1-2 (for Table 4.5; Yura *et al.*, 2008).

Girder Section Properties

$L_g =$	11000	mm
$E =$	209819	MPa
$I_y =$	2.91E+06	mm ⁴
$G =$	77000	MPa
$J =$	8.59E+04	mm ⁴
$I_x =$	8.27E+07	mm ⁴
$h_o =$	349	mm
$S =$	800	mm
$C_b =$	1.35	

$$M_g = 2 \frac{\pi}{L_g} \sqrt{E I_y G J + \frac{\pi^2 E^2 I_y}{4 L_g^2} (I_y h_o^2 + I_x S^2)}$$

Top Flange loading was not considered in critical moment calculation based on previous observations observed by Yura *et al.* (2008)

$M_g = 292$ kN m moment resistance of the system
 $0.7M_g = 204$ kN m 70% of Yura Global Buckling Resistance
 versus
 $M_{cr-EXP} = 209$ kN m
 $\% \Delta = 2.26$ %

Table B.5 Critical moment calculation of specimen C2 (for Table 4.6; Phillips, 1990).

Section Properties	
L =	11000 mm
E =	209819 MPa
I _y =	2.91E+06 mm ⁴
G =	77000 MPa
J =	8.59E+04 mm ⁴
C _w =	8.43E+10 mm ⁶
h =	3.30E+02 mm
S _x =	4.74E+05 mm ³
F _y =	384 MPa

$$M_{cr} = \sqrt{\left(M_0^2 + \frac{P_y^2 h^2 A}{4}\right)} (1 + A) + \beta_T E I_y \leq M_y$$

Lateral Brace Member Stiffness:

A_{br} = 582 mm²
 E = 200000 N/mm²
 L_{br} = 3667 mm
 θ = 66.4 °
 β_L = 5088 N/mm

$$\beta_L = \frac{A_{br} E \cos^2 \theta}{L_{br}}$$

n = 6
 β̄_L = 2.78 N/mm

$$\bar{\beta}_L = \frac{\beta_L n}{L}$$

Δ₀ = 9 mm
 c₁ = 0.449

$$c_L = \frac{1}{1 + 1500 \frac{\Delta_0}{L}}$$

A = 45.04

$$A = \frac{L^2}{\pi} \sqrt{\frac{.67 c_L \bar{\beta}_L}{E I_y}}$$

P_y = 448224 N P_y is the compressive force in the beam expressed as (π²EI_y/L_b²)

Torsional stiffness of single cross-frame:

1/β_t = 1.12E-08 rad / N mm

$$\frac{1}{\beta_t} = \frac{1}{C_t \beta_b} + \frac{1}{\beta_{sec}}$$

Torsional stiffness of brace member:

β_b = 2.92E+09 N mm / rad
 S = 760 mm
 h_b = 330 mm
 L_c = 800 mm
 A_{c/h} = 340 mm²

$$\beta_b = \frac{E S^2 h_b^2}{\frac{2L_c^2}{A_c} + \frac{S^3}{A_h}}$$

Calculation of C_t:

Δ = 9 mm
 C_t = 0.28947368

$$C_t = \frac{1}{1 + 3000 \frac{\Delta_0}{L}}$$

Torsional Stiffness of girder:

β_g = 1.00E+08 N mm / rad
 S = 800 mm
 I_x = 8.27E+07 mm⁴
 L = 11000 mm

$$\beta_g = \frac{12 S^2 E I_x}{L^3}$$

Torsional Stiffness of web stiffener:

β_{sec} = N/A N mm / rad

Web distortion at cross-frame is prevented since web stiffener is welded to top and bottom flanges. Therefore web distortion is prevented.

$$\beta_{sec} = 3.3 \frac{E}{n} \left(\frac{(N+1.5h)t_w^3}{12} + \frac{t_s b_s^3}{12} \right)$$

Continuous Torsional Cross-Frame Stiffness:

n = 2
 β_t = 89531075 N mm / rad
 β_T = 16278 N mm / rad / mm

$$\beta_T = \frac{\beta_t n}{L}$$

M₀ = 1.81E+07 N mm
 M_{cr} = 3371 kNm (single beam)
 6743 kNm (twin beam specimen)

M_y = 182 kNm (single beam)
 364 kNm (twin beam specimen)

* Specimen fails by yielding of the material

versus
 M_{cr-EXP} = 364 kN m Specimen C1-2
 %Δ = 0.0 %

APPENDIX C

Table C.1 CSA S6 (2006) moment calculation for beam braced with torsional cross-frames (top flange loading not considered; for Table 4.7).

Section Properties of W360x33:

E =	209819	MPa
I _y =	2.91E+06	mm ⁴
G =	77000	MPa
J =	8.59E+04	mm ⁴
C _w =	8.43E+10	mm ⁶

Unsupported length of beam:

L =	11000	mm
n =	2	cross-frames
L _u =	3667	mm

$$L_u = \frac{L}{n + 1}$$

Calculation of ω_2 :

M _{max} =	104.5	kN m
M _a =	87.1	kN m
M _b =	104.5	kN m
M _c =	87.1	kN m
ω_2 =	1.086	

$$\omega_2 = \frac{4M_{\max}}{\sqrt{M_{\max}^2 + 4M_a^2 + 7M_b^2 + 4M_c^2}} \leq 2.5$$

$$M_u = 101.8 \quad \text{kN m}$$

$$M_u = \frac{\omega_2 \pi}{L_u} \sqrt{EI_y GJ + \left(\frac{\pi E}{L_u}\right)^2 I_y C_w}$$

Determine Elastic or Inelastic Range:

Z _x =	5.42E+05	mm ³
F _y =	384	MPa
M _p =	208	kN m
0.67M _p =	139	kN m

$$M_u \leq 0.67M_p$$

Calculated Moment Resistance:

ϕ =	1.0	
M _r =	101.8	

$$M_r = \phi M_u$$

versus

$$M_{\text{cr-EXP}} = 104.5 \quad \text{kN m}$$

(Specimen C1-2)

$$\% \Delta = 2.57 \quad \%$$

Table C.2 CSA S6 (2006) moment calculation for beam braced with torsional cross-frames (top flange loading considered; for Table 4.7).

Section Properties of W360x33:

E =	209819	MPa
I _y =	2.91E+06	mm ⁴
G =	77000	MPa
J =	8.59E+04	mm ⁴
C _w =	8.43E+10	mm ⁶

Unsupported length of beam:

L =	11000	mm
n =	2	cross-frames
L _u =	3667	mm

$$L_u = \frac{L}{n + 1}$$

Calculation of ω_2 :

M _{max} =	104.5	kN m
M _a =	87.1	kN m
M _b =	104.5	kN m
M _c =	87.1	kN m
ω_2 =	1.086	

$$\omega_2 = \frac{4M_{\max}}{\sqrt{M_{\max}^2 + 4M_a^2 + 7M_b^2 + 4M_c^2}} \leq 2.5$$

$\omega_2 = 1.0$ (when top flange loading is considered)

M_u = 69.8 kN m

$$M_u = \frac{\omega_2 \pi}{1.2L_u} \sqrt{EI_y GJ + \left(\frac{\pi E}{1.2L_u}\right)^2 I_y C_w}$$

Determine Elastic or Inelastic Range:

Z _x =	5.42E+05	mm ³
F _y =	384	MPa
M _p =	208	kN m
0.67M _p =	139	kN m

$$M_u \leq 0.67M_p$$

Calculated Moment Resistance:

ϕ =	1.0	
M _r =	69.8	

$$M_r = \phi M_u$$

versus

M_{cr-EXP} = 104.5 kN m (Specimen C1-2)

%Δ = 33.25 %

Table C.3 CSA S6 (2006) moment calculation for beam braced with torsional cross-frames and lateral in plan bracing (top flange loading not considered; for Table 4.8).

Section Properties of W360x33:

E =	209819	MPa
I _y =	2.91E+06	mm ⁴
G =	77000	MPa
J =	8.59E+04	mm ⁴
C _w =	8.43E+10	mm ⁶

Unsupported length of beam:

L =	11000	mm
n =	5	Brace Points on B1
L _u =	1833	mm

$$L_u = \frac{L}{n + 1}$$

Calculation of ω_2 :

M _{max} =	184.0	kN m
M _a =	138	kN m
M _b =	153.3	kN m
M _c =	168.7	kN m
ω_2 =	1.181	

$$\omega_2 = \frac{4M_{\max}}{\sqrt{M_{\max}^2 + 4M_a^2 + 7M_b^2 + 4M_c^2}} \leq 2.5$$

$$M_u = 382.7 \text{ kN m}$$

$$M_u = \frac{\omega_2 \pi}{L_u} \sqrt{EI_y GJ + \left(\frac{\pi E}{L_u}\right)^2 I_y C_w}$$

Determine Elastic or Inelastic Range:

Z _x =	5.42E+05	mm ³
F _y =	384	MPa
M _p =	208	kN m
0.67M _p =	139	kN m

$$M_u > 0.67M_p$$

Calculated Moment Resistance:

ϕ =	1.0	
M _r =	202.9	

$$M_r = 1.15 \phi M_p \left[1 - \frac{0.28 M_p}{M_u} \right] \leq \phi M_p$$

versus

$$M_{cr-EXP} = 182 \text{ kN m}$$

$$\% \Delta = -11.48 \%$$

(Specimen C2)

Table C.4 CSA S6 (2006) moment calculation for beam braced with torsional cross-frames and lateral in plan bracing (top flange loading considered; for Table 4.8).

Section Properties of W360x33:

E =	209819	MPa
I _y =	2.91E+06	mm ⁴
G =	77000	MPa
J =	8.59E+04	mm ⁴
C _w =	8.43E+10	mm ⁶

Unsupported length of beam:

L =	11000	mm
n =	5	Brace Points on B1
L _u =	1833	mm

$$L_u = \frac{L}{n + 1}$$

Calculation of ω_2 :

M _{max} =	104.5	kN m
M _a =	87.1	kN m
M _b =	104.5	kN m
M _c =	87.1	kN m
ω_2 =	1.086	

$$\omega_2 = \frac{4M_{\max}}{\sqrt{M_{\max}^2 + 4M_a^2 + 7M_b^2 + 4M_c^2}} \leq 2.5$$

$\omega_2 = 1.0$ (when top flange loading is considered)

$$M_u = 230.5 \text{ kN m}$$

$$M_u = \frac{\omega_2 \pi}{1.2L_u} \sqrt{EI_y GJ + \left(\frac{\pi E}{1.2L_u}\right)^2 I_y C_w}$$

Determine Elastic or Inelastic Range:

Z _x =	5.42E+05	mm ³
F _y =	384	MPa
M _p =	208	kN m
0.67M _p =	139	kN m

$$M_u > 0.67M_p$$

Calculated Moment Resistance:

ϕ =	1.0	
M _r =	178.8	

$$M_r = 1.15\phi M_p \left[1 - \frac{0.28M_p}{M_u}\right] \leq \phi M_p$$

versus

$$M_{cr-EXP} = 182 \text{ kN m}$$

$$\% \Delta = 1.74 \%$$

(Specimen C2)

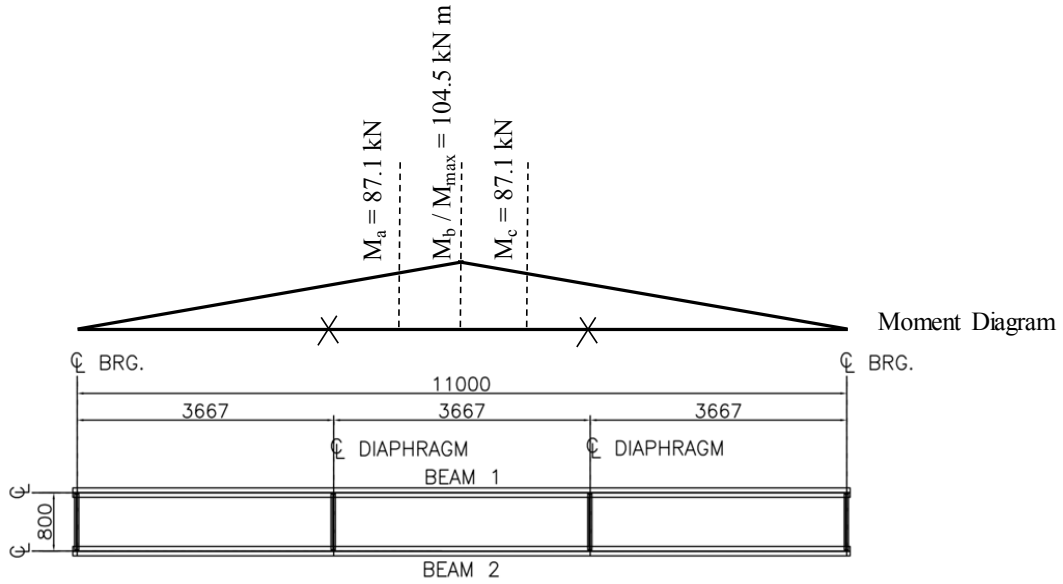


Figure C.1 Diagram for calculation of moment gradient (ω_2) for cross-frame only condition (for Table 4.7).

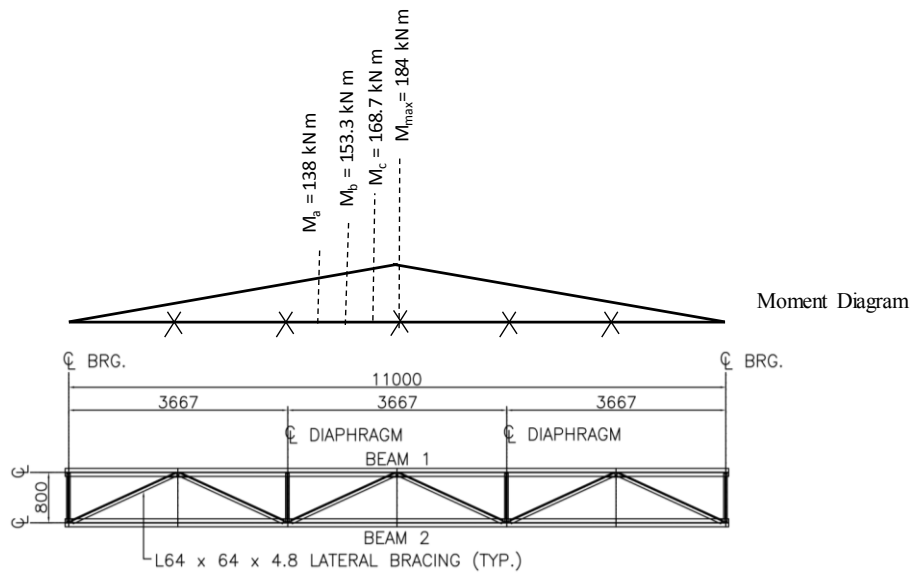


Figure C.2 Diagram for calculation of moment gradient (ω_2) for combination cross-frame and in plan bracing condition (for Table 4.8).

Table C.5 Calculated torsional brace stiffness (for Table 4.7).

L =	11000	mm
n =	2	cross-frames
E =	209819	MPa
I _y =	2.91E+06	mm ⁴

$$\beta_{ti} = \frac{1.2LM_{cr}^2}{nEI_y C_b^2}$$

Torsional Stiffness of Experimental Critical Moment:

$$C_b = 1.086$$

$$M_{cr} = 104.5 \text{ kN m}$$

$$\beta_{ti} = 1.00E+08 \text{ N mm/rad}$$

vs. $\beta_{t\text{-provided}} = 9.70E+07 \text{ N mm/rad}$

$$\% \Delta = 3.18 \%$$

Torsional Stiffness of S6 Critical Moment (top flange loading ignored):

$$C_b = 1.086$$

$$M_{cr} = 101.8 \text{ kN m}$$

$$\beta_{ti} = 9.50E+07 \text{ N mm/rad}$$

vs. $\beta_{t\text{-provided}} = 9.70E+07 \text{ N mm/rad}$

$$\% \Delta = -2.08 \%$$

Torsional Stiffness of S6 Critical Moment (top flange loading considered):

$$C_b = 1.086$$

$$M_{cr} = 69.8 \text{ kN m}$$

$$\beta_{ti} = 4.47E+07 \text{ N mm/rad}$$

vs. $\beta_{t\text{-provided}} = 9.70E+07 \text{ N mm/rad}$

$$\% \Delta = -53.97 \%$$

APPENDIX D

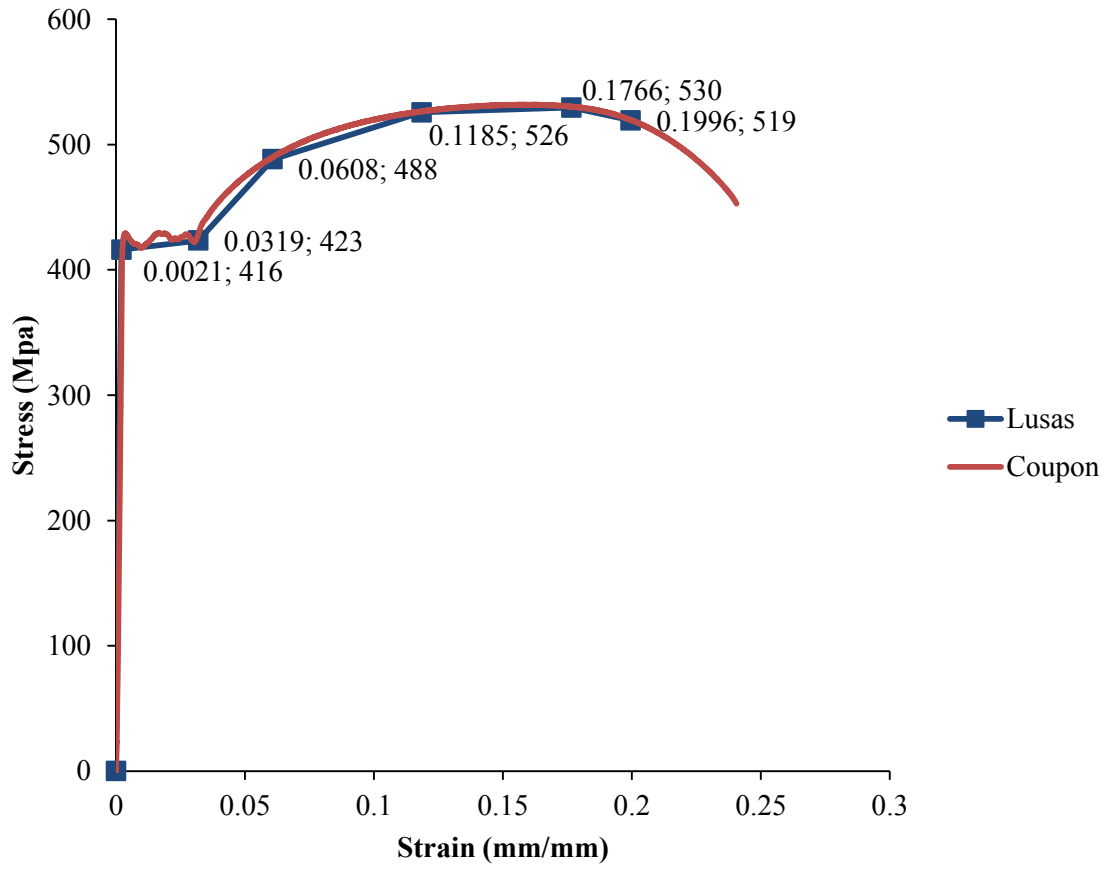


Figure D.1 Stress vs strain diagram for beam 1 web.

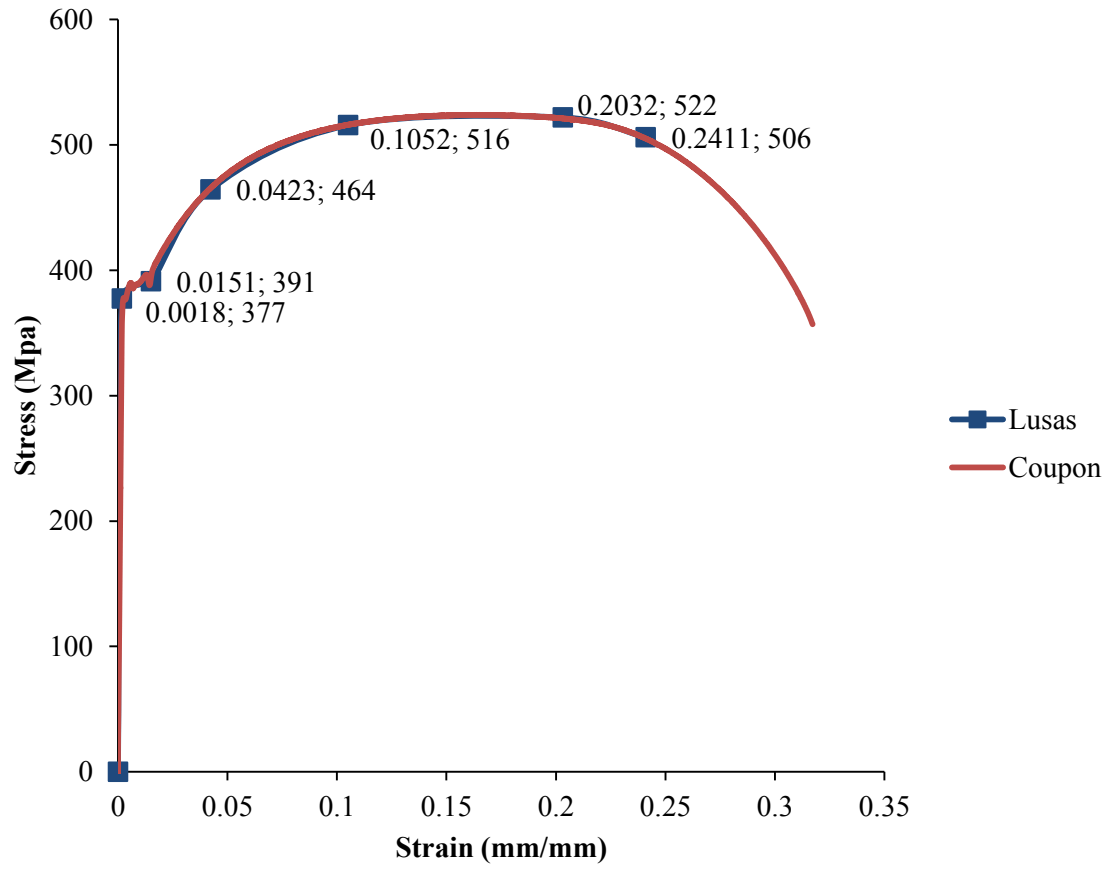


Figure D.2 Stress vs strain diagram for beam 1 flange.

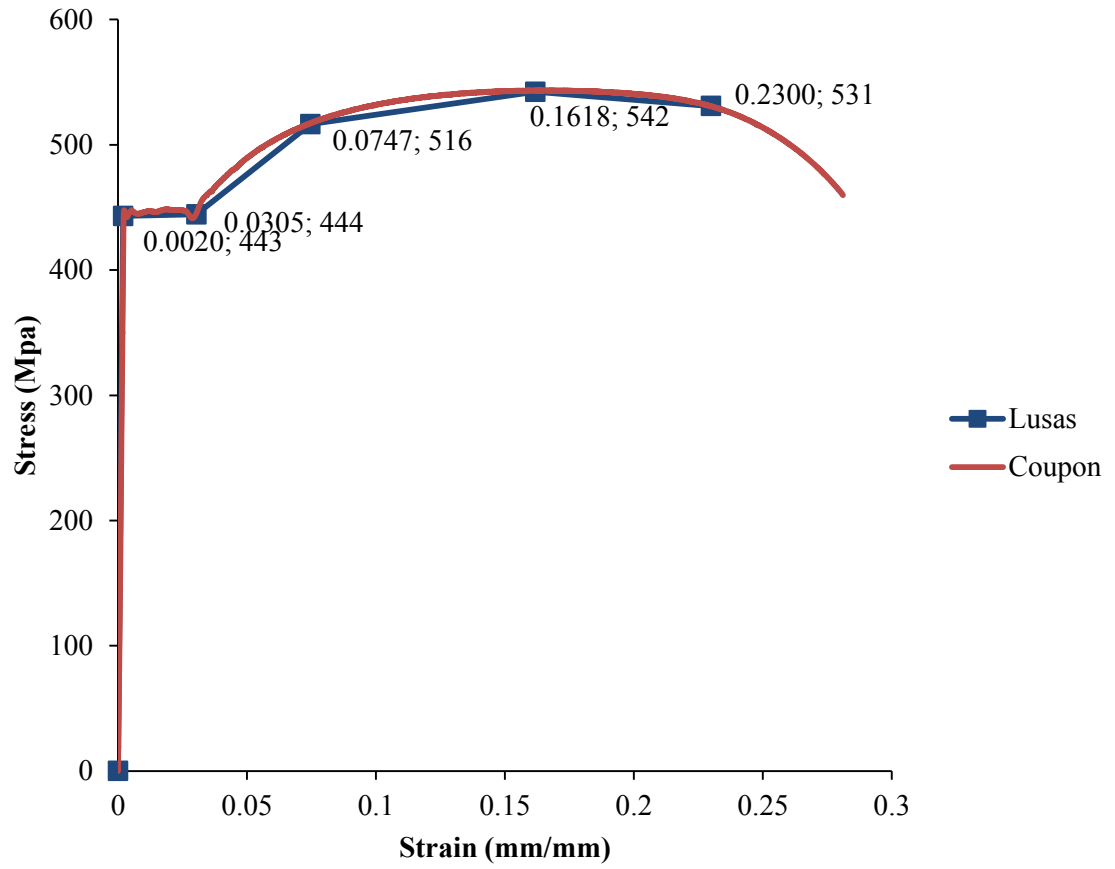


Figure D.3 Stress vs strain diagram for beam 2 web.

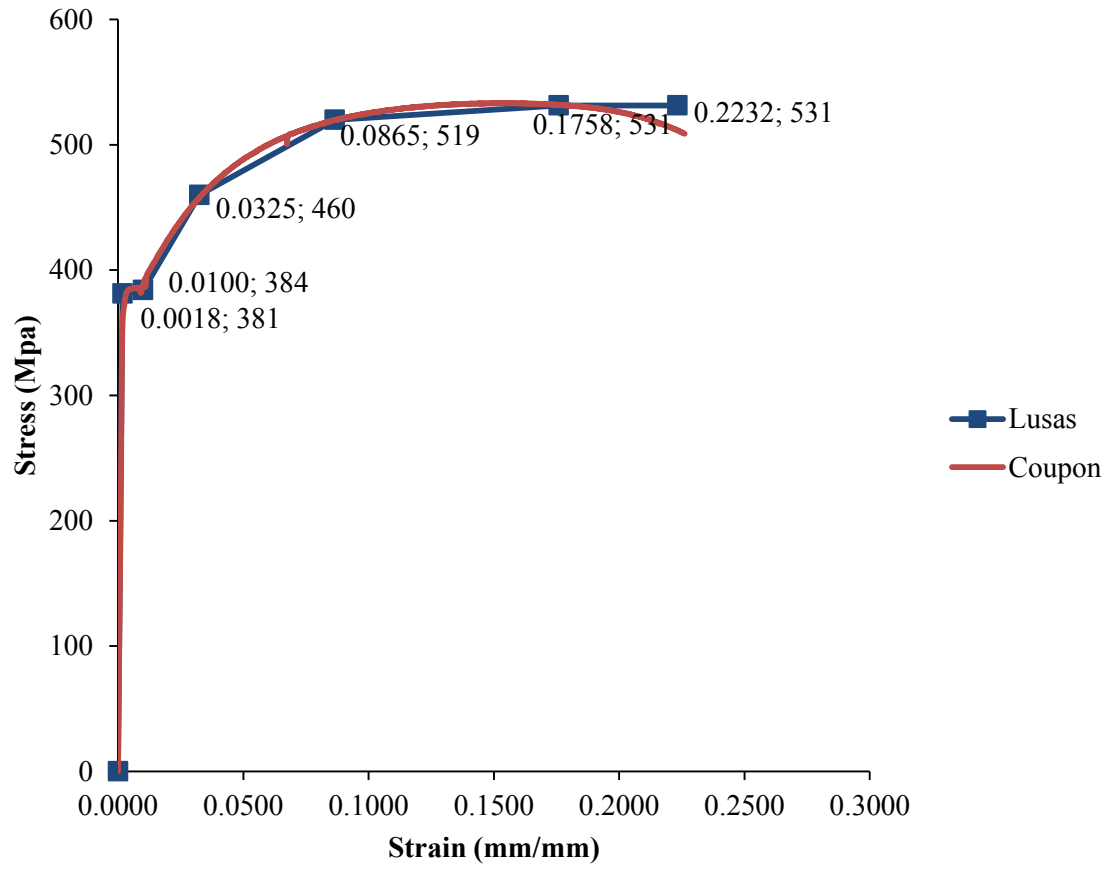


Figure D.4 Stress vs strain diagram for beam 2 flange.

APPENDIX E

Table E.1 Sample calculation of Equation [2.23] critical moment calculation presented in Table 6.1.

Section Properties of Single Beam

$I_g = 11000 \text{ mm}^4$
 $E = 200000 \text{ MPa}$
 $I_y = 2.91E+06 \text{ mm}^4$
 $G = 77000 \text{ MPa}$
 $J = 8.59E+04 \text{ mm}^4$
 $I_x = 8.27E+07 \text{ mm}^4$
 $h_o = 349 \text{ mm}$
 $C_b = 1.35$

$$M_g = 2 \frac{\pi}{L_g} \sqrt{E I_y G J + \frac{\pi^2 E^2 I_y}{4 L_g^2} (I_y h_o^2 + I_x S^2)}$$

For S = 500 mm	$M_g = 179 \text{ kN m}$	moment resistance of the system
	$M_g = 89 \text{ kN m}$	moment resistance of single beam
For S = 650 mm	$M_g = 228 \text{ kN m}$	moment resistance of the system
	$M_g = 114 \text{ kN m}$	moment resistance of single beam
For S = 800 mm	$M_g = 278 \text{ kN m}$	moment resistance of the system
	$M_g = 139 \text{ kN m}$	moment resistance of single beam
For S = 1000 mm	$M_g = 346 \text{ kN m}$	moment resistance of the system
	$M_g = 173 \text{ kN m}$	moment resistance of single beam

Table E.2 Cross-frame torsional stiffness calculation presented in Table 6.2.

Girder Stiffness Component (N·mm/rad)

W360x33 Section Properties

L =	11000	mm
E =	200000	Mpa
$I_x =$	8.27E+07	mm ⁴
S =	800	mm

$$\beta_g = 9.54E+07 \text{ N}\cdot\text{mm}$$

$$\beta_g = \frac{12S^2 E I_x}{L^3}$$

Torsional Brace Member Stiffness Component β_b (N·mm/rad)

	E	S	h_b	L_c	A_b	β_b
L19x19x3.2	200000	800	340	869	111	9.00E+08
L38x38x4.8	200000	800	340	869	340	2.76E+09
L102x102x1	200000	800	340	869	2430	1.97E+10
C250x30	200000	800	340	869	3780	3.06E+10

$$\beta_b = \frac{ES^2 h_b^2}{\frac{2L_c^3}{A_c} + \frac{S^3}{A_h}}$$

Torsional System Stiffness of the Cross-frame β_t (N·mm/rad)

	$1/\beta_t$	β_t
L19x19x3.2	1.16E-08	8.63E+07
L38x38x4.8	1.08E-08	9.22E+07
L102x102x1	1.05E-08	9.50E+07
C250x30	1.05E-08	9.51E+07

$$\frac{1}{\beta_t} = \frac{1}{\beta_b} + \frac{1}{\beta_g}$$

Table E.3 Equation [2.23] critical moment calculations presented in Table 6.4.

Section Properties of Single Beam

$L_g =$	11000	mm
$E =$	200000	MPa
$I_y =$	2.91E+06	mm ⁴
$G =$	77000	MPa
$J =$	8.59E+04	mm ⁴
$I_x =$	8.27E+07	mm ⁴
$h_o =$	349	mm
$C_b =$	1.35	

$$M_g = 2 \frac{\pi}{L_g} \sqrt{E I_y G J + \frac{\pi^2 E^2 I_y}{4 L_g^2} (I_y h_o^2 + I_x S^2)}$$

For $S = 500$ mm

$M_g = 179$ kN m moment resistance of the system
 $M_g = 89$ kN m moment resistance of single beam
 $0.7M_g = 63$ kN m moment resistance of single beam

For $S = 650$ mm

$M_g = 228$ kN m moment resistance of the system
 $M_g = 114$ kN m moment resistance of single beam
 $0.7M_g = 80$ kN m moment resistance of single beam

For $S = 800$ mm

$M_g = 278$ kN m moment resistance of the system
 $M_g = 139$ kN m moment resistance of single beam
 $0.7M_g = 97$ kN m moment resistance of single beam

For $S = 1000$ mm

$M_g = 346$ kN m moment resistance of the system
 $M_g = 173$ kN m moment resistance of single beam
 $0.7M_g = 121$ kN m moment resistance of single beam

Table E.4 Calculation of critical moment presented in Table 6.6 using Equation [2.17].

Section Properties of Single Beam

L =	11000	mm
E =	200000	MPa
I _y =	2.91E+06	mm ⁴
G =	77000	MPa
J =	8.59E+04	mm ⁴
C _T =	1	

$$M_{cr} = \sqrt{C_{bu}^2 M_o^2 + \frac{C_{bb}^2 \beta_T E I_y}{C_T}} \leq M_y$$

$$M_y = \frac{\pi}{L} \sqrt{E I_y G}$$

* C_T considered as 1.0 since top loading results are considered to be negligible for twin girder specimen.

Moment Gradient Factor For Each Cross-Frame Using Equation [2.16] Based on Max Moment Equivalent to Critical Moment of FEA

	Unsupported				
	M _{max}	M _b	M ₀	M _c	C _{bu}
Two Cross-Frames	125.1	62.55	125.1	62.55	1.26491106
Three Cross-Frames	165.0	82.5	165	82.5	1.26491106
Five Cross-Frames	185.6	92.8	185.6	92.8	1.26491106

$$C_b = \frac{4M_{max}}{\sqrt{M_{max}^2 + 4M_o^2 + 7M_b^2 + 4M_c^2}} \leq 2.5$$

Moment Gradient Factor For Each Cross-Frame Using Equation [2.16] Based on Max Moment Equivalent to Critical Moment of FEA

	Supported				
	M _{max}	M _b	M ₀	M _c	C _{sb}
Two Cross-Frames	125.1	104.15	125.1	104.15	1.08685611
Three Cross-Frames	165	103.13	123.75	144.38	1.29352333
Five Cross-Frames	185.6	139.20	154.7	170.10	1.18092272

* Moment Gradient Factor was calculated using the moment diagram from the FE Analysis.

Two Cross-Frames		Three Cross-Frames		Five Cross-Frames	
β _T =	2.55E+04 N·mm/mm	β _T =	3.82E+04 N·mm/mm	β _T =	6.37E+04 N·mm/mm
M ₀ =	17719874 N·mm	M ₀ =	17719874 N·mm	M ₀ =	17719874 N·mm
C _{bu} =	1.265	C _{bu} =	1.265	C _{bu} =	1.265
C _{bb} =	1.087	C _{bb} =	1.294	C _{bb} =	1.181
M _{cr} =	134.3 kN·m	M _{cr} =	194.2 kN·m	M _{cr} =	228.5 kN·m
M _y =	165.9 kN·m	M _y =	165.9 kN·m	M _y =	165.9 kN·m
M _{cr} Governs Failure Mode		M _y Governs Failure Mode		M _y Governs Failure Mode	

Table E.5 Calculation of critical moment using CSA S6 (2006) for two intermediate cross-frames presented in Table 6.7.

Section Properties of W360x33:

E =	200000	MPa
I _y =	2.91E+06	mm ⁴
G =	77000	MPa
J =	8.59E+04	mm ⁴
C _w =	8.43E+10	mm ⁶

Unsupported length of beam:

L =	11000	mm
n =	2	cross-frames
L _u =	3667	mm

$$L_u = \frac{L}{n + 1}$$

Calculation of ω_2 :

M _{max} =	104.5	kN m
M _a =	87.1	kN m
M _b =	104.5	kN m
M _c =	87.1	kN m
ω_2 =	1.086	

$$\omega_2 = \frac{4M_{\max}}{\sqrt{M_{\max}^2 + 4M_a^2 + 7M_b^2 + 4M_c^2}} \leq 2.5$$

$\omega_2 = 1.0$ (when top flange loading is considered)

M_u = 67.2 kN m

$$M_u = \frac{\omega_2 \pi}{1.2L_u} \sqrt{EI_y GJ + \left(\frac{\pi E}{1.2L_u}\right)^2 I_y C_w}$$

Determine Elastic or Inelastic Range:

Z _x =	5.42E+05	mm ³
F _y =	350	MPa
M _p =	190	kN m
0.67M _p =	127	kN m

$$M_u \leq 0.67M_p$$

Calculated Moment Resistance:

ϕ =	1.0	
M _r =	67.2	

$$M_r = \phi M_u$$

versus

M_{cr-FE} = 125.1 kN m (FE Results)
 %Δ = 46.30 %

Table E.6 Calculation of critical moment using CSA S6 (2006) for three intermediate cross-frames presented in Table 6.7.

Section Properties of W360x33:

E =	200000	MPa
I _y =	2.91E+06	mm ⁴
G =	77000	MPa
J =	8.59E+04	mm ⁴
C _w =	8.43E+10	mm ⁶

Unsupported length of beam:

L =	11000	mm
n =	3	cross-frames
L _u =	2750	mm

$$L_u = \frac{L}{n + 1}$$

Calculation of ω_2 :

M _{max} =	167.0	kN m
M _a =	104.4	kN m
M _b =	125.3	kN m
M _c =	146.1	kN m
ω_2 =	1.293	

$$\omega_2 = \frac{4M_{\max}}{\sqrt{M_{\max}^2 + 4M_a^2 + 7M_b^2 + 4M_c^2}} \leq 2.5$$

$\omega_2 = 1.0$ (when top flange loading is considered)

$$M_u = 107.5 \text{ kN m}$$

$$M_u = \frac{\omega_2 \pi}{1.2L_u} \sqrt{EI_y GJ + \left(\frac{\pi E}{1.2L_u}\right)^2 I_y C_w}$$

Determine Elastic or Inelastic Range:

Z _x =	5.42E+05	mm ³
F _y =	350	MPa
M _p =	190	kN m
0.67M _p =	127	kN m

$$M_u \leq 0.67M_p$$

Calculated Moment Resistance:

ϕ =	1.0	
M _r =	107.5	

$$M_r = \phi M_u$$

versus

$$M_{cr-FE} = 167 \text{ kN m} \quad (\text{FE Results})$$

$$\% \Delta = 35.65 \%$$

Table E.7 Calculation of critical moment using CSA S6 (2006) for five intermediate cross-frames presented in Table 6.7.

Section Properties of W360x33:

E =	200000	MPa
I _y =	2.91E+06	mm ⁴
G =	77000	MPa
J =	8.59E+04	mm ⁴
C _w =	8.43E+10	mm ⁶

Unsupported length of beam:

L =	11000	mm
n =	5	cross-frames
L _u =	1833	mm

$$L_u = \frac{L}{n + 1}$$

Calculation of ω_2 :

M _{max} =	185.6	kN m
M _a =	139.2	kN m
M _b =	154.7	kN m
M _c =	170.1	kN m
ω_2 =	1.181	

$$\omega_2 = \frac{4M_{\max}}{\sqrt{M_{\max}^2 + 4M_a^2 + 7M_b^2 + 4M_c^2}} \leq 2.5$$

$\omega_2 = 1.0$ (when top flange loading is considered)

M_u = 220.6 kN m

$$M_u = \frac{\omega_2 \pi}{1.2L_u} \sqrt{EI_y GJ + \left(\frac{\pi E}{1.2L_u}\right)^2 I_y C_w}$$

Determine Elastic or Inelastic Range:

Z _x =	5.42E+05	mm ³
F _y =	350	MPa
M _p =	190	kN m
0.67M _p =	127	kN m

$$M_u > 0.67M_p$$

Calculated Moment Resistance:

ϕ =	1.0	
M _r =	165.9	

$$M_r = 1.15\phi M_p \left[1 - \frac{0.28M_p}{M_u} \right] \leq \phi M_p$$

versus

M_{cr-FE} = 185.6 kN m (FE Results)
 %Δ = 10.61 %

Table E.9 Calculation of effective length using CSA S6 (2006) critical moment calculation for two intermediate cross-frames presented in Table 6.7.

Section Properties of W360x33:

E =	200000	MPa
I _y =	2.91E+06	mm ⁴
G =	77000	MPa
J =	8.59E+04	mm ⁴
C _w =	8.43E+10	mm ⁶

Unsupported length of beam:

L =	7551	mm
n =	2	cross-frames
L _u =	2517	mm

$$L_u = \frac{L}{n + 1}$$

Calculation of ω_2 :

M _{max} =	104.5	kN m
M _a =	87.1	kN m
M _b =	104.5	kN m
M _c =	87.1	kN m
ω_2 =	1.086	

$$\omega_2 = \frac{4M_{\max}}{\sqrt{M_{\max}^2 + 4M_a^2 + 7M_b^2 + 4M_c^2}} \leq 2.5$$

$\omega_2 = 1.0$ (when top flange loading is considered)

M_u = 125.1 kN m

$$M_u = \frac{\omega_2 \pi}{1.2L_u} \sqrt{EI_y GJ + \left(\frac{\pi E}{1.2L_u}\right)^2 I_y C_w}$$

Determine Elastic or Inelastic Range:

Z _x =	5.42E+05	mm ³
F _y =	350	MPa
M _p =	190	kN m
0.67M _p =	127	kN m

$$M_u \leq 0.67M_p$$

Calculated Moment Resistance:

ϕ =	1.0	
M _r =	125.1	

$$M_r = \phi M_u$$

versus

M_{cr-FE} = 125.1 kN m (FE Results)

% Δ = 0.00 %

Table E.10 Calculation of effective length using CSA S6 (2006) critical moment calculation for three intermediate cross-frames presented in Table 6.7.

Section Properties of W360x33:

E =	200000	MPa
I _y =	2.91E+06	mm ⁴
G =	77000	MPa
J =	8.59E+04	mm ⁴
C _w =	8.43E+10	mm ⁶

Unsupported length of beam:

L =	8547	mm
n =	3	cross-frames
L _u =	2137	mm

$$L_u = \frac{L}{n + 1}$$

Calculation of ω_2 :

M _{max} =	167.0	kN m
M _a =	104.4	kN m
M _b =	125.3	kN m
M _c =	146.1	kN m
ω_2 =	1.293	

$$\omega_2 = \frac{4M_{\max}}{\sqrt{M_{\max}^2 + 4M_a^2 + 7M_b^2 + 4M_c^2}} \leq 2.5$$

$\omega_2 = 1.0$ (when top flange loading is considered)

M_u = 167.0 kN m

$$M_u = \frac{\omega_2 \pi}{1.2L_u} \sqrt{EI_y GJ + \left(\frac{\pi E}{1.2L_u}\right)^2 I_y C_w}$$

Determine Elastic or Inelastic Range:

Z _x =	5.42E+05	mm ³
F _y =	350	MPa
M _p =	190	kN m
0.67M _p =	127	kN m

$$M_u \leq 0.67M_p$$

Calculated Moment Resistance:

ϕ =	1.0	
M _r =	167.0	

$$M_r = \phi M_u$$

versus

M_{cr-FE} = 167 kN m (FE Results)

% Δ = 0.00 %

Table E.11 Calculation of effective length using CSA S6 (2006) critical moment calculation for five intermediate cross-frames presented in Table 6.7.

Section Properties of W360x33:

E =	200000	MPa
I _y =	2.91E+06	mm ⁴
G =	77000	MPa
J =	8.59E+04	mm ⁴
C _w =	8.43E+10	mm ⁶

Unsupported length of beam:

L =	12091	mm
n =	5	cross-frames
L _u =	2015	mm

$$L_u = \frac{L}{n + 1}$$

Calculation of ω_2 :

M _{max} =	185.6	kN m
M _a =	139.2	kN m
M _b =	154.7	kN m
M _c =	170.1	kN m
ω_2 =	1.181	

$$\omega_2 = \frac{4M_{\max}}{\sqrt{M_{\max}^2 + 4M_a^2 + 7M_b^2 + 4M_c^2}} \leq 2.5$$

$\omega_2 = 1.0$ (when top flange loading is considered)

M_u = 185.6 kN m

$$M_u = \frac{\omega_2 \pi}{1.2L_u} \sqrt{EI_y GJ + \left(\frac{\pi E}{1.2L_u}\right)^2 I_y C_w}$$

Determine Elastic or Inelastic Range:

Z _x =	5.42E+05	mm ³
F _y =	350	MPa
M _p =	190	kN m
0.67M _p =	127	kN m

$$M_u > 0.67M_p$$

Calculated Moment Resistance:

ϕ =	1.0	
M _r =	155.7	

$$M_r = 1.15\phi M_p \left[1 - \frac{0.28M_p}{M_u} \right] \leq \phi M_p$$

versus

M_{cr-FE} = 185.6 kN m (FE Results)

% Δ = 16.10 %

Table E.12 CSA S6 (2006) critical moment calculation with two cross-frames loaded through shear center (for Table 6.9).

Section Properties of W360x33:

E =	200000	MPa
I _y =	2.91E+06	mm ⁴
G =	77000	MPa
J =	8.59E+04	mm ⁴
C _w =	8.43E+10	mm ⁶

Unsupported length of beam:

L =	11000	mm
n =	2	cross-frames
L _u =	3667	mm

$$L_u = \frac{L}{n + 1}$$

Calculation of ω₂:

M _{max} =	125.1	kN m
M _a =	108.4	kN m
M _b =	125.1	kN m
M _c =	108.4	kN m
ω ₂ =	1.069	

$$\omega_2 = \frac{4M_{\max}}{\sqrt{M_{\max}^2 + 4M_a^2 + 7M_b^2 + 4M_c^2}} \leq 2.5$$

$$M_u = 96.3 \quad \text{kN m}$$

$$M_u = \frac{\omega_2 \pi}{L_u} \sqrt{EI_y GJ + \left(\frac{\pi E}{L_u}\right)^2 I_y C_w}$$

Determine Elastic or Inelastic Range:

Z _x =	5.42E+05	mm ³
F _y =	350	MPa
M _p =	190	kN m
0.67M _p =	127	kN m

$$M_u \leq 0.67M_p$$

Calculated Moment Resistance:

φ =	1.0	
M _r =	96.3	

$$M_r = \phi M_u$$

versus

$$M_{\text{cr-FE}} = 125.1 \quad \text{kN m} \quad (\text{FE Results})$$

$$\% \Delta = 23.04 \quad \%$$

Table E.13 CSA S6 (2006) critical moment calculation with three cross-frames loaded through shear center (for Table 6.9).

Section Properties of W360x33:

E =	200000	MPa
I _y =	2.91E+06	mm ⁴
G =	77000	MPa
J =	8.59E+04	mm ⁴
C _w =	8.43E+10	mm ⁶

Unsupported length of beam:

L =	11000	mm
n =	3	cross-frames
L _u =	2750	mm

$$L_u = \frac{L}{n + 1}$$

Calculation of ω_2 :

M _{max} =	167.0	kN m
M _a =	104.4	kN m
M _b =	125.3	kN m
M _c =	146.1	kN m
ω_2 =	1.293	

$$\omega_2 = \frac{4M_{\max}}{\sqrt{M_{\max}^2 + 4M_a^2 + 7M_b^2 + 4M_c^2}} \leq 2.5$$

$$M_u = 190.7 \text{ kN m}$$

$$M_u = \frac{\omega_2 \pi}{L_u} \sqrt{EI_y GJ + \left(\frac{\pi E}{L_u}\right)^2 I_y C_w}$$

Determine Elastic or Inelastic Range:

Z _x =	5.42E+05	mm ³
F _y =	350	MPa
M _p =	190	kN m
0.67M _p =	127	kN m

$$M_u > 0.67M_p$$

Calculated Moment Resistance:

ϕ =	1.0	
M _r =	157.4	

$$M_r = 1.15\phi M_p \left[1 - \frac{0.28M_p}{M_u} \right] \leq \phi M_p$$

versus

$$M_{cr-FE} = 167 \text{ kN m} \quad (\text{FE Results})$$

$$\% \Delta = 5.76 \%$$

Table E.14 CSA S6 (2006) critical moment calculation with five cross-frames loaded through shear center (for Table 6.9).

Section Properties of W360x33:

E =	200000	MPa
I _y =	2.91E+06	mm ⁴
G =	77000	MPa
J =	8.59E+04	mm ⁴
C _w =	8.43E+10	mm ⁶

Unsupported length of beam:

L =	11000	mm
n =	5	cross-frames
L _u =	1833	mm

$$L_u = \frac{L}{n + 1}$$

Calculation of ω₂:

M _{max} =	185.6	kN m
M _a =	139.2	kN m
M _b =	154.7	kN m
M _c =	170.1	kN m
ω ₂ =	1.181	

$$\omega_2 = \frac{4M_{\max}}{\sqrt{M_{\max}^2 + 4M_a^2 + 7M_b^2 + 4M_c^2}} \leq 2.5$$

$$M_u = 365.7 \text{ kN m}$$

$$M_u = \frac{\omega_2 \pi}{L_u} \sqrt{EI_y GJ + \left(\frac{\pi E}{L_u}\right)^2 I_y C_w}$$

Determine Elastic or Inelastic Range

Z _x =	5.42E+05	mm ³
F _y =	350	MPa
M _p =	190	kN m
0.67M _p =	127	kN m

$$M_u > 0.67M_p$$

Calculated Moment Resistance:

φ =	1.0	
M _r =	186.5	

$$M_r = 1.15 \phi M_p \left[1 - \frac{0.28 M_p}{M_u} \right] \leq \phi M_p$$

versus

$$M_{\text{cr-FE}} = 185.6 \text{ kN m} \quad (\text{FE Results})$$

$$\% \Delta = -0.47 \%$$

Table E.15 AISC 360 (2010) critical moment calculation with two cross-frames loaded through shear center (for Table 6.9).

W360x33 Section Properties

E =	200000	Mpa
I _y =	2.91E+06	mm ⁴
S _x =	4.74E+05	Mpa
J =	8.59E+04	mm ⁴
C _w =	8.43E+10	mm ⁶
c =	1	
h _o =	340.5	mm

$$F_{cr} = \frac{C_b \pi^2 E}{\left(\frac{L_b}{r_{ts}}\right)^2} \sqrt{1 + 0.078 \frac{Jc}{S_x h_o} \left(\frac{L_b}{r_{ts}}\right)^2}$$

$$r_{ts}^2 = 1044.92$$

$$r_{ts} = 32.33$$

$$r_{ts}^2 = \frac{\sqrt{I_y C_w}}{S_x}$$

Unsupported length of beam:

L =	11000	mm
n =	2	cross-frames
L _b =	3667	mm

$$L_b = \frac{L}{n + 1}$$

Calculation of C_b:

M _{max} =	125.1	kN m
M _a =	108.4	kN m
M _b =	125.1	kN m
M _c =	108.4	kN m
C _b =	1.068	

$$C_b = \frac{12.5M_{max}}{2.5M_{max} + 3M_a + 4M_b + 3M_c}$$

F _{cr} =	203	MPa	(critical buckling stress in accordance with AISC)
M _{cr} =	96.2	kN m	(critical moment in accordance with AISC)
			versus
M _{cr-S6} =	96.2	kN m	(CSA-S6-06 Critical Elastic Moment; top flange load height neglected)
%Δ =	-0.04	%	

Table E.16 AISC 360 (2010) critical moment calculation with three cross-frames loaded through shear center.

W360x33 Section Properties

E =	200000	Mpa
I _y =	2.91E+06	mm ⁴
S _x =	4.74E+05	Mpa
J =	8.59E+04	mm ⁴
C _w =	8.43E+10	mm ⁶
c =	1	
ho =	340.5	mm

$$F_{cr} = \frac{C_b \pi^2 E}{\left(\frac{L_b}{r_{ts}}\right)^2} \sqrt{1 + 0.078 \frac{Jc}{S_x h_o} \left(\frac{L_b}{r_{ts}}\right)^2}$$

$$r_{ts}^2 = 1044.92$$

$$r_{ts} = 32.33$$

$$r_{ts}^2 = \frac{\sqrt{I_y C_w}}{S_x}$$

Unsupported length of beam:

L =	11000	mm
n =	3	cross-frames
L _b =	2750	mm

$$L_b = \frac{L}{n + 1}$$

Calculation of C_b:

M _{max} =	167.0	kN m
M _a =	104.4	kN m
M _b =	125.3	kN m
M _c =	146.1	kN m
C _b =	1.250	

$$C_b = \frac{12.5M_{max}}{2.5M_{max} + 3M_a + 4M_b + 3M_c}$$

F _{cr} =	389	MPa	(critical buckling stress in accordance with AISC)
M _{cr} =	184.3	kN m	(critical moment in accordance with AISC)
		versus	
M _{cr-S6} =	190.7	kN m	(CSA-S6-06 Critical Elastic Moment; top flange load height neglected)
%Δ =	3.38	%	
M _y =	165.9	kN m	Material will yield prior to buckling; Therefore yielding governs design

Table E.17 AISC 360 (2010) critical moment calculation with five cross-frames loaded through shear center (for Table 6.9).

W360x33 Section Properties

E =	200000	Mpa
I _y =	2.91E+06	mm ⁴
S _x =	4.74E+05	Mpa
J =	8.59E+04	mm ⁴
C _w =	8.43E+10	mm ⁶
c =	1	
ho =	340.5	mm

$$F_{cr} = \frac{C_b \pi^2 E}{\left(\frac{L_b}{r_{ts}}\right)^2} \sqrt{1 + 0.078 \frac{Jc}{S_x h_o} \left(\frac{L_b}{r_{ts}}\right)^2}$$

$$r_{ts}^2 = 1044.92$$

$$r_{ts} = 32.33$$

$$r_{ts}^2 = \frac{\sqrt{I_y C_w}}{S_x}$$

Unsupported length of beam:

L =	11000	mm
n =	5	cross-frames
L _b =	1833	mm

$$L_b = \frac{L}{n + 1}$$

Calculation of C_b:

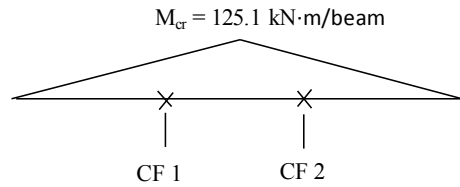
M _{max} =	185.6	kN m
M _a =	139.2	kN m
M _b =	154.7	kN m
M _c =	170.1	kN m
C _b =	1.154	

$$C_b = \frac{12.5M_{max}}{2.5M_{max} + 3M_a + 4M_b + 3M_c}$$

F _{cr} =	754	MPa	(critical buckling stress in accordance with AISC)
M _{cr} =	357.3	kN m	(critical moment in accordance with AISC)
			versus
M _{cr-S6} =	365.7	kN m	(CSA-S6-06 Critical Elastic Moment; top flange load height neglected)
%Δ =	2.29	%	
M _y =	165.9	kN m	Material will yield prior to buckling; Therefore yielding governs design

Table E.18 CSA S6 (2006) brace force calculation for two intermediate cross-frames (for Table 6.10).

Two Cross-Frames:



$$M_{cr} \text{ @ Cross-Frame Locations: } 125.1 \text{ kN}\cdot\text{m} \times 3.667 \text{ m} / 5.5 \text{ m} = 83.4 \text{ kN}\cdot\text{m}/\text{beam}$$

$$F_{\text{horizontal}}: \quad F_{\text{horizontal}} = \frac{M_{cr,CF}}{h_b} \times 0.01 \times \#beams$$

$$h_b = 340 \text{ mm}$$

$$\# \text{ beams} = 2$$

$$F_{\text{horizontal}} = 4.9 \text{ kN}$$

$$F_{\text{Diagonal}}: \quad F_{\text{Diagonal}} = \frac{2 \times F_{\text{horizontal}} \times L_c}{S}$$

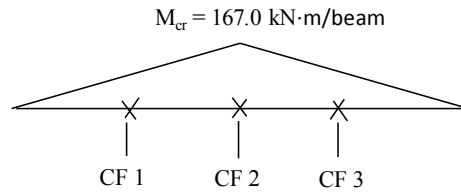
$$L_c = 872.8 \text{ mm}$$

$$S = 800 \text{ mm}$$

$$F_{\text{horizontal}} = 10.7 \text{ kN}$$

Table E.19 CSA S6 (2006) brace force calculation for three intermediate cross-frames (for Table 6.10).

Three Cross-Frames:



M_{cr} @ Cross-Frame Location CF2: 167.0 kN·m/beam

$$F_{\text{horizontal}}: \quad F_{\text{horizontal}} = \frac{M_{cr,CF}}{h_b} \times 0.01 \times \#beams$$

$$h_b = 340 \quad \text{mm}$$

$$\# \text{ beams} = 2$$

$$F_{\text{horizontal}}: \quad \mathbf{9.8} \quad \text{kN}$$

$$F_{\text{Diagonal}}: \quad F_{\text{Diagonal}} = \frac{2 \times F_{\text{horizontal}} \times L_c}{S}$$

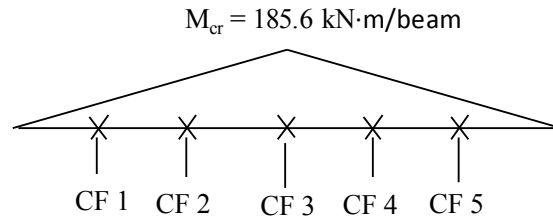
$$L_c = 872.8 \quad \text{mm}$$

$$S = 800 \quad \text{mm}$$

$$F_{\text{horizontal}}: \quad \mathbf{21.4} \quad \text{kN}$$

Table E.20 CSA S6 (2006) brace force calculation for five intermediate cross-frames (for Table 6.10).

Five Cross-Frames:



M_{cr} @ Cross-Frame Location CF3: 185.6 $\text{kN}\cdot\text{m}/\text{beam}$

$$F_{\text{horizontal}}: \quad F_{\text{horizontal}} = \frac{M_{cr,CF}}{h_b} \times 0.01 \times \#beams$$

$$h_b = 340 \quad \text{mm}$$

$$\# \text{ beams} = 2$$

$$F_{\text{horizontal}}: \quad \mathbf{10.9 \quad \text{kN}}$$

$$F_{\text{Diagonal}}: \quad F_{\text{Diagonal}} = \frac{2 \times F_{\text{horizontal}} \times L_c}{S}$$

$$L_c = 872.8 \quad \text{mm}$$

$$S = 800 \quad \text{mm}$$

$$F_{\text{horizontal}}: \quad \mathbf{23.8 \quad \text{kN}}$$